ALL-DIELECTRIC NEAR-FIELD TRANSFORMING STRUCTURES TO DIELECTRIC-LESS METASURFACES FOR HIGH-GAIN ANTENNA SYSTEMS

by

Ali Lalbakhsh

Dissertation submitted in fulfilment of the requirements

for the degree of

DOCTOR OF PHILOSOPHY

Department of Engineering
Faculty of Science and Engineering
Macquarie University
Sydney, Australia

March 2020

STATEMENT OF CANDIDATE

I certify that the work in this thesis entitled **Near-Field Transforming Structures for High-Gain Antenna Systems** has not previously been submitted for a degree nor has it been submitted as part of the requirements for a degree to any other university or institution other than Macquarie University.

I also certify that the thesis is an original piece of research and it has been written by me. Any help and assistance that I have received in my reserach work and the preparation of the thesis itself have been appropiately acknowledged.

In addition, I certify that all information sources and literature used are indicated in the thesis.

.....

Ali Lalbakhsh

To my amazing parents, and my dearest wife.

Abstract

This dissertation presents several novel Electromagnetic (EM) metsurfaces that are engineered to manipulate the electric near-field of any EM sources for various purposes. The approach combines the use of aperture antennas, such as Resonant Cavity Antennas (RCAs), or horn antennas as the EM radiators and the introduced metasurfaces to improve or alter the radiation patterns of the antennas. Initially, a conventional RCA is diagnosed with sub-optimal radiation patterns as a result of poor EM near-field characteristics. So, a novel all-dielectric structure is designed to completely remove this deficiency over a large frequency band, which has never been performed, opening new doors into other cutting-edge applications of this class of antenna, such as passive beamsteering. So, an all-dielectric structure named Near-Field Correcting Structure (NFCS) is designed, which is composed of circular correcting regions, determined by a numerical method in which time-average Poynting vector in conjunction with a phase gradient analysis is utilized to suggest the initial configuration of the NFCS. It is then completed using a customized particle swarm optimization algorithm implemented in MATLAB. The NFCS was fabricated and placed in a subwavelength distance from the RCA and measured. According to the predicted and measured results, the phase and magnitude distributions of the electric near-field of the antenna have been greatly improved over a large bandwidth of 40%, resulting in a high aperture efficiency of 70%. The antenna under NFCS loading has

a peak measured directivity of 21.6 dB, a 3 dB directivity bandwidth of 41% and a 10 dB return loss bandwidth of 46%. Using the same concept of the near-field transformation, all-dielectric metasurfaces composed of near-field rotatable graded-dielectric plates are designed to realize an EM-wave beamsteering antenna. According to the numerical results, the beam can be scanned within a large conical region with an apex angle of 82.2° with a significantly less profile than the mechanically scanned reflector dishes. Unlike the all-dielectric structures mentioned above, a printed metasurface is designed to exhibit a negative transverse-reflection magnitude gradient and, at the same time, a progressive reflection phase gradient over frequency. The first phenomenon has already been realized using either multiple printed dielectric surfaces or a large single FSS, while the proposed metasurface is made of a compact single dielectric. The second phenomenon was also realized using costly fabrication techniques, which is not the case with the proposed low-cost metasurface. A prototype of the metasurface was fabricated and tested with a partially shielded cavity, creating an improved RCA, showing a very high aperture efficiency of 83% with a peak directivity 16.2 dB and a 3 dB directivity bandwidth of 22%.

In all aforementioned metasurfaces, dielectric substrates are an integral part of the metasurface configurations, where the realization of the metasurfaces is not impossible without the dielectric substrates. However, in some less-specialized applications, the high cost of dielectric substrates can be an impediment to the applications of metasurfaces. Furthermore, dielectric-based metasurafces cannot directly be used in high-power applications, as they are prone to dielectric breakdown. To address this issue, several dielectric-less metasurfaces are presented in this thesis for a variety of applications, including single-frequency phase correction of RCAs, wideband spatial filtering, and wideband phase correction of shortened horn antennas. Unlike the existing Phase Correcting Structures (PCSs) of RCA, a hybrid topology of fully-metallic spatial phase shifters are developed to form an All-Metal PCS (AMPCS), resulting in an extremely lower proto-

typing cost as that of other state-of-the-art substrate-based PCSs. The APMCS was fabricated using laser technology and tested with a RCA to verify its predicted performance. Results show that the phase uniformity of the RCA aperture has been remarkably improved, resulting in 8.4 dB improvement in the peak gain of the antenna and improved sidelobe levels (SLLs). The antenna system including APMCS has a peak gain of 19.42 dB with a 1 dB gain bandwidth of around 6%.

In order to achieve wideband performance using dielectric-less metasurfaces, a design methodology is presented in which the integrity of metasurfaces are ensured by metallic inductive grids, which have a wideband bandpass frequency response. Therefore, additional metallic resonators can be integrated into the grid, without any mechanical stability concerns. Based on this design mechanism, Orthogonal Dipole Resonator (ODRs) are integrated into the metallic grids to form a wideband bandpass metasurface filter with excellent performance. The metasurface filter is composed of multiple segregated metallic layers, where the selectivity of the filter can be improved by increasing the number of layers. The metasurface filter has the capability of harmonic suppression and has a fully adjustable wide passband of 31%. Extension of this method can be used to develop wideband phase correcting metasurfaces, which can be used to significantly enhance the near-field of shortened horn antennas, leading to a small horn antennas with plane wave. The horn antenna with the metasurface has a uniform phase distribution over a large frequency band of 25%, resulting a high aperture efficiency of 66% at 11.7 GHz. The antenna system has a measured peak directivity of 20.9 dB with a large frequency band from 9.70 GHz to 12.45 GHz.

Acknowledgements

This PhD thesis would not have been possible without the support and contribution of many amazing individuals. Foremost, I would like to thank my supervisor, Prof. Karu P. Esselle, the director of Centre for Collaboration in Electromagnetic and Antenna Engineering (C4CELANE), for giving me the opportunity to work as a PhD student under his supervision. Thank you for your unconditional dedication, support and guidance.

I would like to thank Dr. Muhammad Usman Afzal, whose enthusiasm for research, patience, and diligence have motivated me to complete this long journey regardless of all the obstacles. Thank you for being the most honest friend I have ever had, the most supportive research collaborator I have ever worked with, and thank you for letting me grow with you and your exceptional research ethics. I am indebted to you for sparing your time to discuss the direction of my project and to assist me with a lot of measurements in the anechoic chamber.

I would like to thank Dr Stephanie L. Smith, my co-supervisor from The Commonwealth Scientific and Industrial Research (CSIRO), for her genuine support and suggestions and guidance throughout my candidature. I would like to thank CSIRO for awarding me prestigious grants on Astronomy and Space exploration, which helped me with more financial support during my PhD.

I am also very grateful and would like to acknowledge the Commonwealth of Australia

and Macquarie University for honouring me with the prestigious International Macquarie Research Excellence Scholarship (iMQRES). Without this financial support, this PhD research would not have been possible. On top of that, I thank Macquarie University for granting a Postgraduate Research Funding (PGRF) and WiMed Research Centre Travel Grants which enabled me to present the outcomes of my research in several international conferences.

I express gratitude to Dr. Basit A. Zeb, Mr. Touseef Hayat and Mr. Foez Ahmed for the active research collaborations we had over the last year. Thank you for the technical supports, thoughtful suggestions, critical comments, patience, and promptness during countless revisions of research manuscripts. I am looking forward to working with you again in the future.

My acknowledgments also goes to my friend in The school of Engineering, Ms. Bahar Mohammadzade, Mr. Hossein Eslahi, Mr. Ehsan Saeedi, Mr. Arslan Kiyani, and all HDR students and staffs from the school with whom I have ever had the honour of meeting and working with. Thank you for the technical and non-technical supports, collaborations, friendship and unforgettable moments we spent over the last three years.

Special thanks are also for my amazing parents. Thank you for all your love, supports, and prayers. Also, I would like to express my huge appreciation to my wife, Fatemeh, who has been faithfully standing beside me throughout this long journey. Thank you for believing in me and my dreams, and for never letting me settle for anything less than my best. Without you, I would not have sustained thus far. I love you.

List of Publications

This thesis is based on the following original research papers, which are published or in review. These publications are referred to in the text by Roman numbers.

A. Discussed in Thesis

I. Ali Lalbakhsh, Muhammad U. Afzal, Karu P. Esselle, Stepanie L. Smith, "Wideband Near-Field Correction of a Fabry-Perot Resonator Antenna," *IEEE Transactions on Antennas and Propagation*, vol. 67, no. 3, pp. 1975–1980, Jan. 2019.

II. Muhammad U. Afzal, Ali Lalbakhsh, Karu P. Esselle, "Electromagnetic-wave beam-scanning antenna using near-field rotatable graded-dielectric plates," *Journal of Applied Physics*, vol. 124, no. 23, pp. 912–915, Jul. 2018.

III. Ali Lalbakhsh, Muhammad U. Afzal, Karu P. Esselle, Stepanie L. Smith, Basit A. Zeb, "Single-dielectric Wideband Partially Reflecting Surface with Variable Reflection Components for Realization of a Compact High-gain Resonant Cavity Antenna," *IEEE Transactions on Antennas and Propagation*, vol. 67, no. 3, pp. 1916–1921, Jan. 2019.

IV. Ali Lalbakhsh, Muhammad U. Afzal, Karu P. Esselle, Stepanie L. Smith, "Low-Cost Non-Uniform Metallic Lattice for Rectifying Aperture Near-Field of Electromagnetic

Bandgap Resonator Antennas," *IEEE Transactions on Antennas and Propagation,* Vol. 68, 2020.

V. Ali Lalbakhsh, Muhammad U. Afzal, Karu P. Esselle, Stepanie L. Smith, "Low-Cost Wideband Frequency-Selective Surface Bandpass Filter with a Polarization Insensitive All-Metal Structure," *IEEE Transactions on Antennas and Propagation (Under review).*

VI. Ali Lalbakhsh, Muhammad U. Afzal, Karu P. Esselle, Stepanie L. Smith, " Substrate-Less Polarization-Independent Structure for Wideband Near-Field Correction," *IEEE Transactions on Antennas and Propagation (Under review).*

B. Other Related Publications

1. B Mohamadzade, RBVB Simorangkir, R. Hashmi, Ali Lalbakhsh, "A Conformal Ultrawideband Antenna with Monopole-like Radiation patterns," *IEEE Trans. Antennas Propag.*, vol. 68, 2020.

2. B. Mohamadzade, Ali Lalbakhsh, R. B Simorangkir, A. Rezaee, and R. M Hashmi, "Mutual Coupling Reduction in Microstrip Array Antenna by Employing Cut Side Patches and EBG Structures," *Progress In Electromagnetics Research*, vol. 89, pp. 179-187, 2020.

3. T Hayat, MU Afzal, Ali Lalbakhsh, KP Esselle, "3D Printed Phase-Rectifying Transparent Superstrate for Resonant-Cavity Antenna," *IEEE Antennas and Wireless Propagation Letters*, vol. 18, no. 7, pp. 1400-1404, 2019.

4. T Hayat, MU Afzal, Ali Lalbakhsh, KP Esselle, "Additively Manufactured Perforated Superstrate to Improve Directive Radiation Characteristics of Electromagnetic Source," *IEEE Access*, vol. 7, pp. 153445–153452, 2019.

5. Priyanka Das, Kaushik Mandal, Ali Lalbakhsh, "Single Layer Polarization Insensitive Frequency Selective Surface for Beam Reconfigurability of Monopole Antennas," *Journal of Electromagnetic Waves and Applications*, vol.34, no. 1, pp. 86-102, 2020.

6. B Mohamadzade, RBVB Simorangkir, R. Hashmi, R Gharaei, Ali Lalbakhsh, "Monopole-like and semi-directional reconfigurable pattern antenna for wireless body area network applications," *Microwave and Optical Technology Letters*, vol. 16, no. 12, pp. 2760-2765, 2019.

7. MB Jamshidi Ali Lalbakhsh, B Mohamadzade, H Siahkamari, "A novel neural-based approach for design of microstrip filters," *AEU-International Journal of Electronics and Communication*, vol. 110, 152847, 2019.

8. Ali Lalbakhsh, KP Esselle, S L. Smith, "A Wideband Procedure for Near-Field Enhancement of Resonant Cavity Antennas," *16th Australian Symposium on Antennas, 2019.*

9. G. Karimi, H. pourasad, Ali Lalbakhsh, H Siahkamari, "Design of a compact ultra-narrow band dual band filter for WiMAX application," *AEU-International Journal of Electronics and Communication*, vol. 110, 152827, 2019.

10. M. B. Jamshidi,A Lalbakhsh, S. Lotfi, H. Siahkamari, B. Mohamadzade, and J. Jalilian, "A Neuro-based Approach to Designing a Wilkinson Power Divider," *International Journal of RF and Microwave Computer Aided Engineering*, e22091, 2019.

11. Muhammad U. Afzal, Karu P. Esselle, Ali Lalbakhsh, " A Methodology to Design A Low-Profile Composite-Dielectric Phase-Correcting Structure„" *IEEE Antennas and Wireless Propagation Letters*, vol. 17, no. 7, pp. 1223–1227, 2018.

12. Ali Lalbakhsh, Muhammad U. Afzal, Karu P. Esselle, "Multiobjective particle swarm optimization to design a time-delay equalizer metasurface for an electromagnetic band-

gap resonator antenna," *IEEE Antennas and Wireless Propagation Letters*, vol. 16, pp. 912–915, 2016.

13. T Hayat, MU Afzal, Ali Lalbakhsh, F. Ahmed, Karu P. Esselle, "Comparative Analysis of Highly Transmitting Phase Correcting Structures for Electromagnetic Bandgap Resonator Antenna," *International Workshop on Antenna Technology (iWAT 2020)*, Bucharest Romania, 2020.

14. T Hayat, MU Afzal, F. Ahmed, Ali Lalbakhsh, Karu P. Esselle, "3D Printable Lightweight Porous Superstrate for Improved Radiation Performance of Antenna," *3rd Australian Microwave Symposium* Sydney, Australia, Feb. 2020.

15. A. Lalbakhsh, MU Afzal, KP Esselle, S L. Smith, "An array of electromagnetic bandgap resonator antennas for v-band backhaul applications," *The IIER International Conference*, Tokyo, Japan, 7th-8th August, 2019, 69-71.

16. MU Afzal, A. Lalbakhsh, N. Y. Koli, KP Esselle, "Antenna Beam Steering by Near-Field Phase Transformation: Comparison between Phase Transforming Printed Metasurfaces and Graded-Dielectric Plates," *International Conference on Electromagnetics in Advanced Applications (ICEAA 2019)*, Granada, Spain, 0593-0595.

17. MB Jamshidi, N Alibeigi, A. Lalbakhsh, S Roshani, "An ANFIS Approach to Modeling a Small Satellite Power Source of NASA," *International Conference on Networking, Sensing and Control (ICNSC)*, Banff, Canada, 2019, pp. 459-464.

18. Ali Lalbakhsh, Muhammad U. Afzal, Karu P. Esselle, ""Simulation-driven particle swarm optimization of spatial phase shifters," in *Proc. 18th IEEE international Conference on Electromagnetics in Advanced Applications (ICEAA)*, Cairns, Australia, Sep., 2016, pp 428–430

19. Ali Lalbakhsh, Muhammad U. Afzal, Karu P. Esselle, ""Directivity improvement of a Fabry-Perot cavity antenna by enhancing near field characteristtics," in *Proc. 17th IEEE International Symposium on Antenna Technology and Applied Electromagnetics (ANTEM)*, Montreal, Canada, Jul., 2016, pp 1–3

20. Ali Lalbakhsh, Karu P. Esselle, "Design of an improved resonant cavity antenna," in *Proc. 19th IEEE international Conference on Electromagnetics in Advanced Applications (ICEAA)*, Verona, Italy, Sep., 2017.

21. Ali Lalbakhsh, Muhammad U. Afzal, Karu P. Esselle, Stepanie L. Smith, "Design of an artificial magnetic conductor surface using an evolutionary algorithm," in *Proc. 19th IEEE international Conference on Electromagnetics in Advanced Applications (ICEAA)*, Verona, Italy, Sep., 2017.

22. Ali Lalbakhsh, Muhammad U. Afzal, Karu P. Esselle, Stepanie L. Smith, "A fast design procedure for quadrature reflection phase," in *Proc. 39th Progress in Electromagnetics Research Symposium (PIERS)*, Singapore, Nov., 2017.

23. Ali Lalbakhsh, Muhammad U. Afzal, Karu P. Esselle, Stepanie L. Smith, ""Design of a single-slab low-profile frequency selective surface," in *Proc. 39th Progress in Electromagnetics Research Symposium (PIERS)*, Singapore, Nov., 2017.

24. Muhammad U. Afzal, Ali Lalbakhsh, Karu P. Esselle, Stepanie L. Smith, ""Integration of sparse array feed and phase correction to design high gain resonant cavity antennas," in *Proc. 39th Progress in Electromagnetics Research Symposium (PIERS)*, Singapore, Nov., 2017.

25. Ali Lalbakhsh, Muhammad U. Afzal, Karu P. Esselle, Stepanie L. Smith, "A High-gain wideband ebg resonator antenna for 60 GHz unlicenced frequency band," in *Proc.*

12th European Conference on Antennas and Propagation (EuCAP), London, UK, Apr. 2018, pp. 1–3.

26. Muhammad U. Afzal, Karu P. Esselle, Ali Lalbakhsh, "A Metasurface to Focus Antenna Beam at Offset Angle," in *Proc. 2nd URSI Atlantic Radio Science Meeting (AT-RASC)*, Meloneras , Spain, Jun. 2018, pp. 1–4.

27. Ali Lalbakhsh, Muhammad U. Afzal, Karu P. Esselle, Stepanie L. Smith, "A Fabry-Perot Cavity Antenna with a Non-Uniform Permittivity Superstrate for V-band Applications," in *Proc. 7th IEEE Asia-Pacific Conference on Antennas and Propagation (APCAP)*, Auckland, New Zealand, Aug. 2018, pp. 223–224.

28. Muhammad U. Afzal, Ali Lalbakhsh, Karu P. Esselle, "A Low-Profile Beam-Tilted Antenna Array for Receiving Direct-Broadcast Satellite Services," in *Proc. 7th IEEE Asia-Pacific Conference on Antennas and Propagation (APCAP)*, Auckland, New Zealand, Aug. 2018, pp. 147–148.

Contents

List of Figures

List of Tables

List of Abbreviations

AMPCS	All-Metal Phase Correcting Structure
AusAMF	Australian Antenna Measurement Facility
AWC	Abrasive Waterjet Cutting
C4CELANE	Centre for Collaboration in Electromagnetic and Antenna Engineering
CP	Circularly Polarized
CST	Computer Simulation Technology
DR	Diagonal Resonator
EM	Electromagnetic
ERA	Electromagnetic Band-Gap Resonator Antenna
EBG	Electromagnetic Band-Gap
FEM	Finite-Element Method
5G	Fifth Generation
FIT	Finite-Integration Technique
FPRAs	Fabry–Perot resonator antennas
FRS	Fully Reflecting Surface
FSS	Frequency Selective Surface

FWB	Fractional Bandwidth
GDP	Graded-Dielectric Plates
LGD	Linearly Graded Dielectric
GRIN	Gradient Index
LP	Linearly Polarized
LEO	Low Earth Orbit
MAM	Metal Additive Manufacturing
MEO	Medium Earth Orbit
NFCS	Near-Field Correcting Structure
ODR	Orthogonal Dipole Resonator
PCB	Printed Circuit Board
PCS	Phase Correcting Structure
PDMS	polydimethylsiloxane
PLA	Polylactic Acid
PSO	Particle Swarm Optimization
PRS	Partially Reflecting Surface
RF	Radio Frequency
RGD	Radially Graded Dielectric
RCA	Resonant Cavity Antenna
SC	Static Cross
SLL	Sidelobe Level
TC	Throughout Cross
UWB	Ultra-wideband
VICTS	Variable Inclination Continuous Transverse-Stub
VPA	Varying PermittivitY Axis
VSWR	Voltage Standing Wave Ratio

CHAPTER 1

Introduction

1.1 Background

With the growing wireless communications dominating the consumer market over the past decade, tremendous interest in the development and application of different types of metasurfaces and near-filed transforming devices has emerged. This class of Electromagnetic (EM) devices can be used either as a standalone module for applications such as EM shielding, spatial filtering, radome, or they can be integrated into other EM sources for EM-field transformations which are otherwise not possible. Such integration has recently attracted a lot of interest from the EM community, particularly for high-gain-related applications, such as beamsteering, Radar Cross-Section (RCS) reduction and phase correction of the aperture antennas. Metasurfaces can be considered as a subset of metamaterials, which are generally composed of artificial structural units engineered to develop some specific EM properties. The macroscopic structure of metamaterial can be arbitrary, and it can be named metasurafce when one of the dimensions is significantly smaller than the others. Metasurfaces can be categorized based on the materials used in their structural elements, which can be all-dielectric substances, all-metal components or a combination of metal and dielectric materials.

1.1.1 All-Dielectric Metasurface

All-dielectric metasurfaces used with high-gain antennas can broadly be categorized based on their mechanism to create the required EM characteristics. Such metasurfaces can generally be realized by either varying the thickness of the dielectric throughout the metasurface, or using composite-based materials, in which dielectric substances with various permittivities are utilized. Several configurations based on the mentioned mechanism have been proposed for a variety of applications, including horn lens antennas, transmitarrays, reflectarrays and Partially Reflecting Structures (PRS) for realization of high-performance Resonant Cavity Antennas (RCAs) [1–3]. For example, planar lenses for horn antennas have been developed using all-dielectric gradient index (GRIN) metasurfaces. Apart from phase transformation, magnitude correction has recently been achieved by adding a baffle inside the horn and placing a GRIN metasurafce on the horn aperture. In [4], a metasurface transmitarray has been designed by perforating a dielectric slab to achieve high transmission magnitude and a full phase range. The integration of this metasurface with a shortened horn antenna resulted in around 10 dB improvement in the peak directivity of the antenna. In [5], low-cost polymers have been used to form three different dielectric reflectarrays with variable dielectric thickness, operating at 100 GHz. These prototypes were fabricated based one polymer-jetting 3-D printing technology. A compact single-layer metasurface having permittivity gradient in the directions transverse to the RCA axis has been designed to achieve a high directivity-bandwidth product from a RCA [6].

1.1.2 Printed Metasurface

Printed metasurfaces are the most common type of metasurfaces, as the combination of conductive patterns on numerous commercially available dielectric substrates provides metasurface designers with an extremely large degree of freedom. Such diversity in design

results in a wide range of printed metasurfaces applications, including transmitarrays, reflectarrays, partially reflecting surfaces [7–12], spatial filters [13–16], beamsteering [17, 18] orbital angular momentum beam generator [19], and near-field phase and magnitude corrections [20–22]. From configuration point of view, printed metasurfaces can be composed of one or multiple dielectric substrates with conductive patterns, in which each layer exhibits resonance or non-resonance behaviors. For example, desired frequency response of spatial metasurface filters can be achieved by bounding multiple capacitive and inductive layers [13, 23–25]. In a different approach, resonating elements can be designed on each layer of the dielectric substrates and the desired frequency response can be achieved by tunning the resonant frequencies of the resonating elements [26–31].

1.1.3 All-Metal Metasurface

The use of microwave dielectric substrates in all-dielectric and printed metasurfaces provides a great flexibility in the design of metasurfaces. However, they are expensive and cannot directly be used in high-power applications, due to the risk of dielectric breakdown [32–36]. As a solution to this issue, all-metal configurations can be used for realization of metasurfaces. However, most of the known conductive patterns used in the printed metasurfaces cannot be implemented without a dielectric substrate, limiting the realization of all-metal metasurfaces. As a result, there are significantly fewer number of all-metal metasurfaces reported for different applications, such as reflectarrays, PRS and transmitarrays. An all-metal transmitarray has been realized using numerous cross-slot units, which are capable to give a full transmission phase range with a high transmission magnitude by rotation of the cross slot [34]. The same method has been used in conjunction with the concept of Risley prism to develop an all-metal beam steering antenna. The antenna consists of a feed antenna and two rotating metal metasurfaces, which are responsible to steer the radiation beam in both azimuth and elevation planes [35]. The

limitations associated to these all-metal metasurfaces are that they only operate at a single frequency, and secondly they can work only for circular polarization. In a different approach, a dual-band linearly polarized transmitarray has been proposed in [36]. The transmitarray is composed of four metallic layers containing rectangular slots, which are used to control the magnitude and phase range of transmission coefficients by varying the slot length [36]. Another linearly polarized metasurface has been reported in [37] to be used as a transmitarray. The metasurface was composed of three metallic layers, where each layer has a square wide slot within which there are a number of parallel stubs.

1.2 Challenges and Objectives

Near-field transformation and integration of metasurfaces with EM sources have recently been considered as a solution for various problems faced in the EM community. In terms of the near-field transformation, several near-field transforming structures have been proposed to tailor the electric near-filed of aperture antennas like RCAs for better radiation performance. Achieving a large operational frequency band and ability to tailor both magnitude and phase of aperture antennas is a challenge which is addressed in this thesis.

In relation to metasurfaces, they can be categorized based on their constituting materials, which can be all-dielectric, all-metal, and a combination of both dielectric and metal. The challenge here is to develop a cost-effective design methodology of metasurfaces, which can be used to address critical issues in relation to the high-gain antennas, such as the limited bandwidth and large footprint of high-gain RCA, the large aperture phase error of some high-gain antennas, and steering the radiations of high-gain antennas through a low-profile passive mechanism. Furthermore, the challenge of high manufacturing cost of metasurfaces can also be addressed using the all-metal configurations, where the expensive microwave dielectric substrates are made redundant. However, there are

limited geometries, which can be used in a purely metallic configuration, limiting the applications of all-metal metasurfaces.

Therefore, the objectives of this thesis are defined as follows:

1- A methodology for developing wideband near-field transformation, in which both magnitude and phase can be controlled over a large frequency band.

2- A methodology for developing low-profile passive beamsteering of high-gain antennas using metasurfaces.

3- A methodology for developing a cost-effective PRS, having all the critical characteristics, such as a single commercial dielectric layer, compactness, stable |S11| bandwidth, high gain, and wideband response.

4- A methodology for developing all-metal metasurfaces for phase correction of high-gain antennas at a singe frequency.

5- A methodology for developing wideband all-metal metsurface for phase correction of high-gain antennas.

1.3 Thesis Contribution and Outline

This thesis contributes to the area of metasurface design and fabrication, as well as near-field transformation. The first contribution is the development of a new holistic design procedure for wideband electric near-field correction of high-gain antennas, which is explained in **Chapter 2**. The realization of the proposed Near-Field Correcting Structure (NFCS) is divided into two major steps. The time-average Poynting vector is firstly calculated for the antenna under consideration based on which the minimum lateral size of the NFCS is chosen. Setting the total size of the NFCS, the minimum number of correcting regions is calculated using the aperture phase gradient over the desired frequency band. An optimization-based approach is then used to find the thickness of each correcting re-

gion in the NFCS to correct both near-filed magnitude and phase of the antenna. As an example case, one NFCS has been designed, fabricated and tested with a conventional RCA. The antenna under NFCS loading has a peak measured directivity of 21.6 dB, a 3-dB directivity bandwidth of 41% and a 10-dB return loss bandwidth of 46%, which covers the directivity bandwidth. The diameter of the proposed NFCS is $3.8\lambda_{0c}$, which is around half that of all other previously phase-correcting structures of RCAs , where λ_{0c} is the free-space wavelength at the central frequency of the NFCS (13.09 GHz). This chapter has been published in the *IEEE Transactions on Antennas and Propagation*, vol. 67, no. 3, pp. 1975–1980, Jan. 2019.

The second contribution of this thesis is the development of all-dielectric metsurfaces used for realization of a low-profile high-gain beam-scanning antenna system, which is explained in **Chapter 3**. The antenna system comprises a RCA and three graded-dielectric metasurfaces: one radially graded and two linearly graded. The radially graded dielectric (RGD) is stationary while the two linearly graded dielectric (LGD) metasurfaces are rotated around the antenna axis. The antenna system has a maximum peak directivity of 21 dB at 11 GHz, showing around 9 dB improvement over the bare RCA. Using three different beam-scanning configurations, it is estimated that the beam can be scanned within a large conical region with an apex angle of 82.2^{o}. The total height of the antenna system is $2.2\lambda_0$, which is significantly less than mechanically scanned reflector dishes. Due to the low and planar profile of the antenna system, it can be used to develop Ka and Ku band beam-scanning antennas for ground and mobile terminals to communicate with upcoming LEO and MEO satellites. This chapter has been published in the *Journal of Applied Physics*, vol. 124, no. 23, pp. 912–915, Jul. 2018.

The third contribution of this thesis is the development of a compact, low-cost Partially Reflecting Surface (PRS) for a wideband high-gain RCA, requiring only a single commercial dielectric slab, which is explained in **Chapter 4**. The PRS has one non-

uniform double-sided printed dielectric, which exhibits a negative transverse-reflection magnitude gradient and at the same time a progressive reflection phase gradient over frequency. The measured peak directivity of the antenna is 16.2 dBi at 11.4 GHz with a 3-dB bandwidth of 22%. The measured peak gain and 3-dB gain bandwidth are 15.75 dBi and 21.5%, respectively. The PRS has a radius of 29.25 mm ($1.1\lambda_0$) with a thickness of 1.52 mm ($0.12\lambda_g$), and the overall height of the antenna is $0.6\lambda_0$, where λ_0 and λ_g are the free-space and guided wavelengths at the center frequency of 11.4 GHz. This chapter has been published in the *IEEE Transactions on Antennas and Propagation*, vol. 67, no. 3, pp. 1916–1921, Jan. 2019.

The fourth contribution of this thesis is the development of an industrially-justified metasurface to rectify the near-field non-uniformity associated with the high-gain RCA, which is explained in **Chapter 5**. In this approach, a new generation of PCS, in which microwave dielectric substrates, known as the main cause of cost, are removed from the PCS configuration, introducing an All-Metallic PCS (AMPCS). The APMCS was fabricated using laser technology and tested with a RCA to verify its predicted performance. Results show that the phase uniformity of the RCA aperture has been remarkably improved, resulting in 8.4 dB improvement in the peak gain of the antenna and improved sidelobe levels. The antenna system including APMCS has a peak gain of 19.42 dB with a 1-dB gain bnamdwidth of 6%. This chapter has been submitted to *IEEE Transactions on Antennas and Propagation*.

The fifth contribution of this thesis is the development of a harmonic-free wideband all-metal metasurface filter, capable of handling both circular and linear polarization. In this approach, which is explained in **Chapter 6**, non-resonant segregated metallic grids are designed to ensure the consistency of the structure, and secondly to provide a wideband bandpass response without the unwanted second harmonic. The frequency response is then further tailored by introducing metallic resonant elements implemented

on the previously designed metallic grids. The role of each section of the proposed topology is theoretically discussed through equivalent-circuit models and modal analysis, when the modular geometry reconfigurabilities of the metasurface filter emerged and verified. This chapter has been submitted to *IEEE Transactions on Antennas and Propagation.*

The sixth contribution of this thesis is the development of a wideband all-metal meta-surface to be used with a shortened horn antenna for generation of highly-directive plane-wave radiations over a large frequency band. The presented metallic metasurface explained in **Chapter 7** is incredibly low-cost and support both circular and linear polarization over a large fractional bandwidth of 25%. The proposed passive meta-surface is composed of two freestanding layers of metallic resonating elements collectively create high transmission with controllable transmission phase. The predicted and measured results suggest that the horn with the meta-surface generates plane wave for a wide frequency band, and has considerably higher aperture efficiency of 66% compared to the horn without the metasurface. The measured peak directivity of the antenna system is around 21 dB with a large 3-dB directivity bandwidth of 25%. This chapter has been submitted to *IEEE Transactions on Antennas and Propagation.* Finally, conclusion and future work are presented in **Chapter 8**.

1.4 Thesis Organization

This dissertation follows Thesis-by-Publication format which has been approved by Macquarie University Higher Degree Research Office. It consists of an introduction including background, and the following list of my major 6 journal articles, as well as conclusion chapter. The thesis materials are original texts and figures of my publications, published or in review, which have been reformatted for readability improvement. In addition to these 6 major journal articles, which correspond to Chapter 2 to Chapter 7 of the thesis,

a complete list of publications resulted from my candidature is included in the List of Publications under "Other Related Publications" section.

I. Ali Lalbakhsh, Muhammad U. Afzal, Karu P. Esselle, Stepanie L. Smith, "Wideband Near-Field Correction of a Fabry-Perot Resonator Antenna," *IEEE Transactions on Antennas and Propagation*, vol. 67, no. 3, pp. 1975–1980, Jan. 2019.

II. Muhammad U. Afzal, Ali Lalbakhsh, Karu P. Esselle, "Electromagnetic-wave beam-scanning antenna using near-field rotatable graded-dielectric plates," *Journal of Applied Physics*, vol. 124, no. 23, pp. 912–915, Jul. 2018.

III. Ali Lalbakhsh, Muhammad U. Afzal, Karu P. Esselle, Stepanie L. Smith, Basit A. Zeb, "Single-dielectric Wideband Partially Reflecting Surface with Variable Reflection Components for Realization of a Compact High-gain Resonant Cavity Antenna," *IEEE Transactions on Antennas and Propagation*, vol. 67, no. 3, pp. 1916–1921, Jan. 2019.

IV. Ali Lalbakhsh, Muhammad U. Afzal, Karu P. Esselle, Stepanie L. Smith, "Low-Cost Non-Uniform Metallic Lattice for Rectifying Aperture Near-Field of Electromagnetic Bandgap Resonator Antennas," *IEEE Transactions on Antennas and Propagation*, Vol. 68, 2020.

V. Ali Lalbakhsh, Muhammad U. Afzal, Karu P. Esselle, Stepanie L. Smith, "Low-Cost Wideband Frequency-Selective Surface Bandpass Filter with a Polarization Insensitive All-Metal Structure," *IEEE Transactions on Antennas and Propagation (Under review).*

VI. Ali Lalbakhsh, Muhammad U. Afzal, Karu P. Esselle, Stepanie L. Smith, " Substrate-Less Polarization-Independent Structure for Wideband Near-Field Correction," *IEEE Transactions on Antennas and Propagation (Under review).*

1.5 Author's Contribution

In all the publications listed above, I have conducted the major investigations, designs, measurements, data processing, and drafting. Only in Article II, my second co-supervisor Dr. Afzal and I jointly conceiving the idea behind the design and both contributed in manuscript writing. Prof. Esselle, who is my principal supervisor, and my co-supervisor Dr. Smith provided invaluable guidance, suggestions and advice at every stage of this research. Dr Afzal provided initial support regarding the simulation environment as well as measurements of the fabricated prototypes. Prof. Esselle, Dr. Smith, and Dr. Afzal helped in reviewing, and proof-reading articles based on which this thesis is formed.

CHAPTER 2

All-Dielectric Near-Field Transforming Structure

2.1 Abstract

A systematic approach to correcting electric near-field phase and magnitude over a wide band for Fabry-Perot Resonator Antennas (FPRAs) is presented. Unlike all other unit-cell based near-field correction techniques for FPRAs, which merely focus on phase correction at a single frequency, this method delivers a compact Near-Field Correcting Structure (NFCS) with a wide operational bandwidth of 40%. In this novel approach, a time-average Poynting vector in conjunction with a phase gradient analysis is utilized to suggest the initial configuration of the NFCS for wideband performance. A simulation-driven optimization algorithm is then implemented to find the thickness of each correcting region, defined by the gradient analysis, to complete the NFCS design. According to the predicted and measured results, the phase and magnitude distributions of the electric near field have been greatly improved, resulting in a high aperture efficiency of 70%. The antenna under

Published as: Ali Lalbakhsh, Muhammad U. Afzal, Karu P. Esselle, Stepanie L. Smith, "Wideband Near-Field Correction of a Fabry-Perot Resonator Antenna," *IEEE Transactions on Antennas and Propagation*, vol. 67, no. 3, pp. 1975–1980, Jan. 2019.

NFCS loading has a peak measured directivity of 21.6 dB, a 3-dB directivity bandwidth of 41% and a 10-dB return loss bandwidth of 46%, which covers the directivity bandwidth. The diameter of the proposed NFCS is $3.8\lambda_{0c}$, which is around half that of all other unit-cell-based phase-correcting structures, where λ_{0c} is the free-space wavelength at the central frequency of the NFCS (13.09 GHz).

2.2 Introduction

Fabry-Perot Resonator Antennas (FPRAs), also known as electromagnetic band-gap resonator antennas, resonant-cavity antennas, and 2-D leaky-wave antennas, have recently attracted significant attention in the electromagnetics field for their highly directive radiation patterns and simple feed mechanism. There are countless applications in modern communication systems for this class of antenna, such as base stations, back-haul networks and satellite communications [38–44]. Antennas of this type could possibly replace array antennas and bulky parabolic antennas in applications where the fabrication cost and the volume of space taken up by the antenna are limitations [14, 45]. Conventional FPRAs are basically composed of a cavity created between a ground plane and a Partially Reflecting Surface (PRS). Constructive wave interference above the cavity, caused by numerous reflections inside the cavity, results in boresight radiation patterns [14, 38–46]. Nontransparent Fully Reflecting Surfaces (FRSs) have been recently proposed in [20,47,48] for FPRAs. This new design procedure offers more flexibility in the adjustment of the FPRAs' aperture field, such as SLLs reduction [20].

The electromagnetic field reflected by the superstrate constructively adds to the incident field from the primary feed resulting in improved broadside radiation. However, a small field radiates in the transverse direction that causes a non-uniform aperture phase distribution. It should be noted that lens theory cannot be applied to estimate the phase

errors caused by this phenomenon, due to the infinite number of rays emitting from the radiating aperture and the lack of an isolated point source, as explicitly explained in [49].

Therefore, Phase Correcting Structures (PCSs) were recently introduced for FPRAs [21,22,25,49–51]. In spite of their excellent performance in correcting phase errors, leading to a significant improvement in peak gain, their operational bandwidth is very limited (around 10%). Such a limited bandwidth adversely affects the data rate, which is a critical factor in modern communication systems [52]. In [22] a hybrid approach, which is a combination of equivalent-circuit models and full-wave simulation, was proposed for phase correction of an FPRA at a single frequency. The antenna achieved a high peak gain of 19.85 dB, as a result of its uniform phase distribution. All the PCSs proposed in [21, 25, 49, 50] were designed based on a unit-cell model, in which PCSs are composed of various arrays of spatial phase shifters designed in isolation at a single frequency. The narrowband nature of this technique along with the relatively large unit cells ($\lambda_0/3$) resulted in narrowband PCSs with a large lateral size, leading to sub-optimal aperture efficiency (around 30%). Inspired by PCSs, several phase-shifting surfaces have been incorporated in FPRAs for some other applications, such as beamsteering [17,18]. Another application of near-field modification has recently been proposed to mitigate coupling between antennas in multiple-input, multiple-output (MIMO) systems [53].

In this paper, we propose a holistic design procedure for wideband electric near-field correction of FPRAs. The proposed method does not have the limitations associated with other unit-cell based approaches, delivering significantly enhanced near-field components over a large bandwidth, never achieved by other PCSs. The realization of the proposed Near-Field Correcting Structure (NFCS) is divided into two major steps. As will be explained in Section II, the time-average Poynting vector is calculated for a conventional FPRA, based on which the minimum lateral size of the NFCS is chosen. Setting the total size of the NFCS, the minimum number of correcting regions is calculated using the

aperture phase gradient over the desired frequency band. An optimization-based approach is explained in Section III to find the thickness of each correcting region in the NFCS and re-adjust the cavity height to maintain the bandwidth in the predetermined frequency band. Optimization and electromagnetic results are presented in Section IV, where the near-field and far-field results verify the proposed technique. A brief conclusion is given in Section V.

2.3 Configuration of the Near-field Correcting Structure (NFCS)

A conventional FPRA configuration with a PRS made of TMM3 dielectric material, designed at 11 GHz, is shown in Fig. 2.1. The PRS's thickness and the cavity height are close to $\lambda_g/4$ and $\lambda_0/2$, respectively, as recommended in the literature [38,39] and [21,25,49,50]. λ_0 is the free-space wavelength and λ_g is the guided wavelength within the PRS at the design frequency (11 GHz). The feed antenna is a waveguide-fed slot antenna with dimensions of 9 $mm \times 14$ mm, placed in the center of the ground plane. The time average Poynting vector was calculated at a distance of λ_0 above the antenna using (2.1) and plotted in Fig. 2.2.

$$\mathbf{W} = \frac{1}{2} Re[\mathbf{E} \times \mathbf{H}^*] \tag{2.1}$$

As can be seen from Fig. 2.2, the average power radiated form the antenna plunges radially, which means that the marginal region of the aperture has significantly less contribution to the far-field radiation patterns. Indeed, around 73% of the average power is radiated from the central part of the aperture which comprises only one fourth of the aperture area. Based on this analysis, $3\lambda_0 \times 3\lambda_0$ is suggested as the critical area of the aperture for near-field correction, as opposed to $6\lambda_0 \times 6\lambda_0$ recommended for phase cor-

rection in [21, 25, 49, 50]. So, the effects of the outer regions are ignored here for having a compact structure. It can be hypothesized that a smaller aperture is easier for correction, and as a result near-field correction over a large bandwidth would be possible.

In order to choose an efficient configuration for the wideband NFCS, a more detailed investigation into the nature of the non-uniform electric near field of FPRAs is essential. Fig. 2.3 shows 2-D phase distributions at 6 discrete frequencies at a distance of $2\lambda_0$ from the conventional FPRA depicted in Fig. 2.1. The antenna has a peak directivity of 10.6 dB at 12 GHz and its 3-dB directivity bandwidth is 21%, (10.6 - 13.1 GHz). As can be seen from Fig. 2.3, the phase distribution deteriorates as frequency increases, while a nearly circular symmetry of phase distribution remains at all frequencies. According to this analysis, not only does the proposed NFCS need to be composed of annular regions, but the width of each region is required to be small enough to effectively manipulate the near field at higher frequencies, when the wavelength gets smaller. So, the aperture phase distribution needs to be analyzed at various frequencies throughout the band. To do

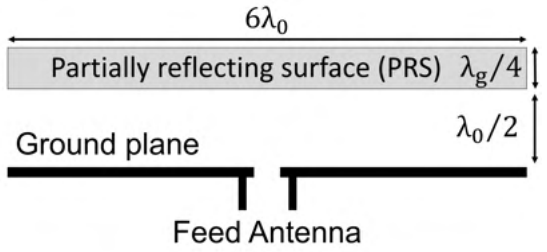

Figure 2.1: Configuration of a conventional FPRA.

this, the actual phase values are captured on a reference plane in cylindrical coordinates with $\phi = 0$ and at a height of $2\lambda_0$ above the PRS. Fig. 2.4 shows the phase distribution on the reference plane at 5 distinct frequencies (11, 12,. . . ,15 GHz). It can be observed that the phase errors increase more rapidly in the outer regions than in the central part of the aperture. Therefore, the aperture is divided into minor and major phase-error regions. In the former, phase errors are less than 45 degrees at all frequencies (11-15 GHz),

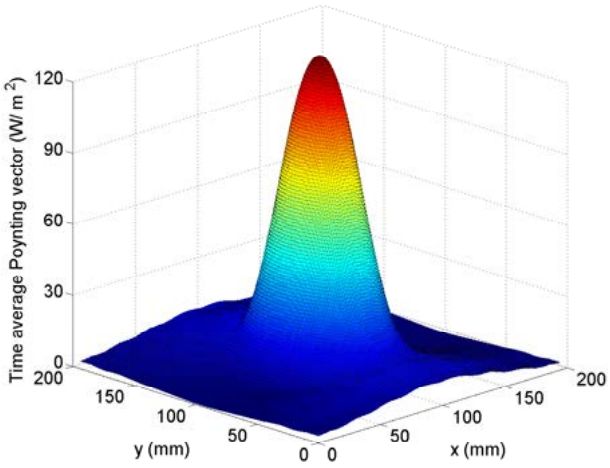

Figure 2.2: Time-average Poynting vector of the conventional FPRA at the design frequency of 11 GHz. The permittivity and the thickness of the PRS are 3.27 and 3.1 mm, respectively. The cavity height is 12.5 mm.

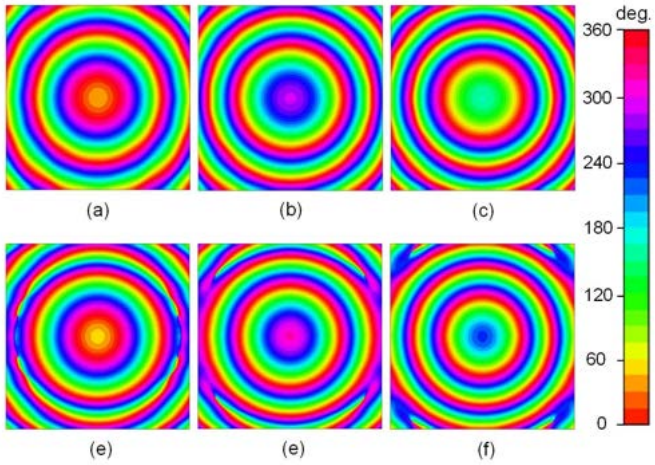

Figure 2.3: 2-D phase distribution of a conventional FPRA over a wide frequency range at a distance of z=$2\lambda_0$ from the PRS. (a) f= 10 GHz, (b) f= 11 GHz, (c) f= 12 GHz, (d) f= 13 GHz, (e) f= 14 GHz, (f) f= 15 GHz.

representing a small phase gradient of $90^o/\lambda_0$ (equal to 3.2 deg/mm), while the latter undergoes severe phase non-uniformity, showing the highest phase gradient of $214^o/\lambda_0$ (equal to 7.5 deg/mm) at 15 GHz. To ensure the accomplishment of phase correction

throughout the aperture, the major phase-error region is considered as the reference to calculate the maximum correcting width of the NFCS. Such aperture division prevents wrong perception of the near-field phase behavior, as the strong non-uniformity in the outer area of the aperture is not overlooked, due to the more uniform phase distribution in the central area. So, a new formula, (2.2), based on the phase gradient analysis is proposed for the width of the correcting regions, which ensures wideband performance of the NFCS. The maximum width of the correcting regions is 5.7 mm ($0.21\lambda_0$), which is yielded by

$$W_{NFCS} \leq \frac{\Delta\theta}{\tau_{max}} \tag{2.2}$$

where $\Delta\theta$ represents the allowed phase differences in the uniform phase region (45^o) and τ_{max} is the highest absolute value of the phase gradient on the aperture ($214^o/\lambda_0$). Therefore, the NFCS is composed of 8 circular correcting regions with a width of 5.5 mm ($\simeq 0.2\lambda_0$), as shown in Fig. 2.5(a). Such a rotationally symmetrical structure can also support circular polarization, which is desired in many applications.

2.4 NFCS Design Using Optimization-Based Approach

In the previously reported design methodologies of narrow-band PCSs [21, 25, 49, 50], each correcting region was designed in isolation from other regions at a single frequency. Additionally a further optimization was required to re-tune the cavity height to retain the bandwidth in the desired region. On the other hand, we propose a holistic numerical optimization technique, in which all mutual effects of the correcting regions are considered throughout a large frequency band. In this approach, apart from the eight correcting regions' heights ($h1, h2, ..., h8$), the air gap between the NFCS and the PRS (H_{Gap}) as

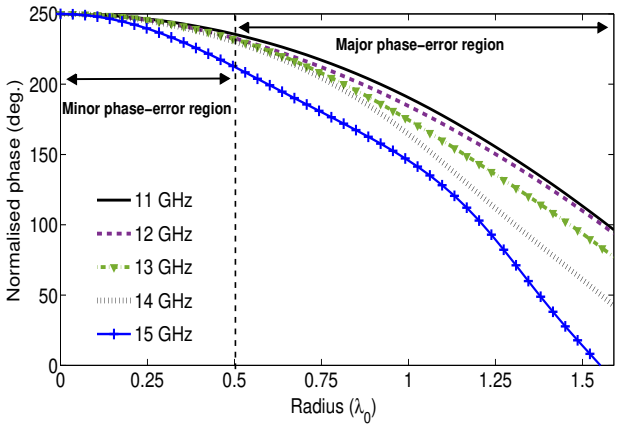

Figure 2.4: Phase distribution on a reference plane located $2\lambda_0$ above the PRS with a radius of $1.5\lambda_0$ in cylindrical coordinates with $\phi = 0^o$. The lateral size and the thickness of the PRS are $3\lambda_0$ and $\lambda_g/4$, respectively, where λ_0 is the free-space wavelength and λ_g is the guided wavelength within the PRS at 11 GHz. The cavity height and the slot antenna size are $\lambda_0/2$ and $9\ mm \times 14\ mm$, respectively.

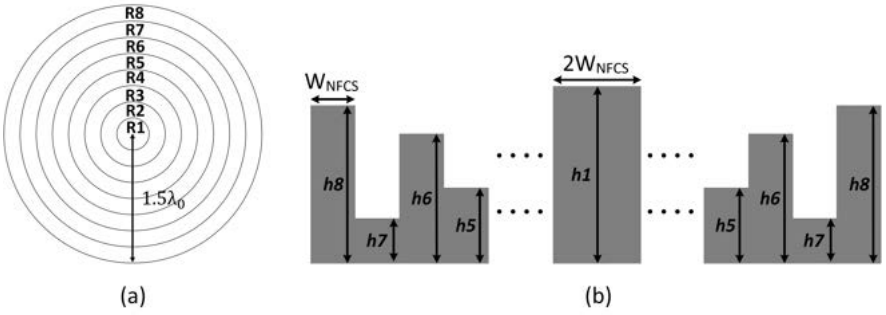

Figure 2.5: (a) Top view of the proposed near-field correcting structure. The diameter of the whole structure is $1.5\lambda_0$ and the width of each region is nearly $0.2\lambda_0$. (b) Cross-sectional view of the NFCS, showing the random thickness of each correcting region before optimization.

well as the cavity height (H_{Cavity}) are optimized at the same time, which is another advantage over the unit-cell based approaches. Therefore, it is a 10-dimensional problem, for which we use Particle Swarm Optimization (PSO). PSO is a nature-inspired optimization technique proposed in 1995 [54] and brought to the electromagnetic community in 2002 [55]. Since then, numerous electromagnetic components have been designed using various PSO-based approaches [56–64]. Other nature-based optimization algorithms such as neural network and ant colony can also be used for such microwave and electromagnetic applications [65–72]. In order to find the 10 parameters associated with the NFCS, a PSO algorithm was implemented in MATLAB, where all data processing and decision making are carried out. A VBA channel is then created between MATLAB and CTS MWS for data transfer, as depicted in Fig. 6. Such an optimization procedure is known as simulation-driven optimization, which has recently found a wide application in the antenna community [25, 57, 59, 62, 73–75]. This method is particularly advantageous when a large scale of data mining needs to be carried out, which is the case in designing a wideband NFCS, as both magnitude and phase distributions at several frequencies on multiple reference planes need to be monitored and corrected. In addition, it provides more flexibility, compared to built-in optimizers, in terms of controlling and training the swarm, by varying PSO parameters such as social and cognitive coefficients, condition of solution boundaries, allowed particle velocity etc. [60, 62, 73, 74, 76]. Some efficient techniques have recently been proposed to expedite multi-objective optimization of real-world problems, such as a combination of low and high fidelity simulations along with co-kriging [74].

The PSO was initialized by 4 particles with a maximum movement of 20% of their corresponding solution spaces, defined by

$$h1, ..., h8 \in= [0, 1.5\lambda_0] \tag{2.3}$$

$$H_{Cavity} \in= [0.3\lambda_0, 0.7\lambda_0] \tag{2.4}$$

$$H_{Gap} \in= [0.02\lambda_0, 0.07\lambda_0] \tag{2.5}$$

where $h1, ...h8$ are the heights of the correcting regions in the NFCS, and tabulated in Table 2.2. As shown in Fig. 2.5, H_{Cavity} and H_{Gap} are the updated cavity height and the gap between the PRS and the NFCS, respectively. In this algorithm, a reflecting boundary condition was imposed to confine particles to the legitimate solution space. In this procedure, a fitness function is defined to aggregate both the phase and magnitude-correcting performance of each candidate. Therefore, we define Phase Index (2.6) and Mag. Index (2.7) to quantify the phase and magnitude corrections, which can then be aggregated in a simple fitness function. To do so, (2.6) is used to calculate the average standard deviation of the phase distribution along the x and y axes at 5 distinct frequencies (11,...,15 GHz) on two observation surfaces, as shown in Fig. 2.6. Using two observation surfaces decreases the errors associated with the field distortion created by the NFCS. The observation surfaces are at distances of $1.3\lambda_0$ and $2\lambda_0$ from the PRS, as shown in Fig. 2.6. The Mag. Index is defined by (2.7) to calculate the deviation from a Cosine-Squared distribution, which results in minimum Side-Lobe Levels (SLLs) in linear arrays [77]. The PRS can be assumed as an array, due to multiple reflections inside the cavity [46]. So, we borrow this concept to avoid undesirable SLLs over the large bandwidth. A fitness function for this multi-objective multi-dimensional optimization problem is calculated by (2.10), which is an aggregation of phase and magnitude effects.

$$\begin{aligned} Phase\ Index = \frac{1}{2} \times (&\sqrt{\frac{1}{5}\sum_{i=1}^{5}(\phi(x)_i - \mu(x))^2} + \\ &\sqrt{\frac{1}{5}\sum_{i=1}^{5}(\phi(y)_i - \mu(y))^2}) \end{aligned} \tag{2.6}$$

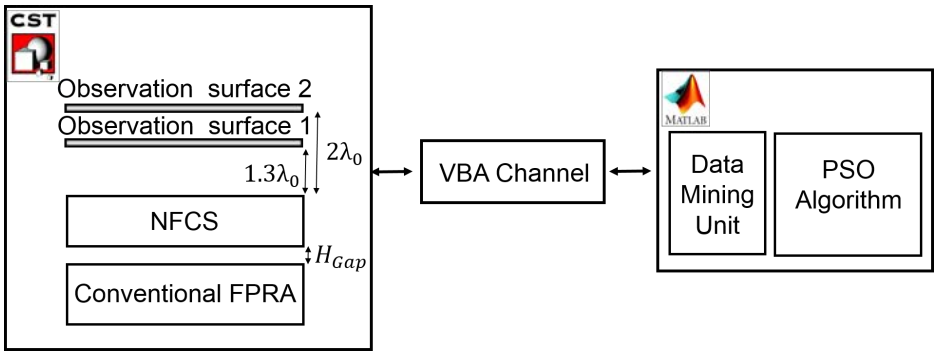

Figure 2.6: Implemented setup for NFCS design.

$$Mag.\ Index = \frac{1}{2} \times (\frac{1}{5}\sum_{i=1}^{5} \mid Mag(x)_i - I(x) \mid + \frac{1}{5}\sum_{i=1}^{5} \mid Mag(y)_i - I(y) \mid) \tag{2.7}$$

where

$$I(x) = cos^2(\frac{\pi}{l}x) \tag{2.8}$$

$$I(y) = cos^2(\frac{\pi}{l}y) \tag{2.9}$$

where l is the aperture length in each axis, and ϕ and μ are the actual and mean phase values at each point along each axis.

$$Fitness = 10 \times Phase\ Index + 2 \times Mag.\ Index \tag{2.10}$$

2.5 Results

The PSO was run for 180 iterations and delivered a candidate with the highest fitness value of -55.88, found at the 135^{th} iteration. The values of the 10 parameters optimized

by the algorithm are shown in Table I, based on which the NFCS was realized. 2-D views of the phase distribution at various frequencies are plotted in Fig. 2.7, underscoring the significant improvement in phase distribution. To give a better view of the drastic enhancement in the phase distribution, a normalized 1-D distribution of the near-field phase along the x-axis is plotted in Fig. 2.8 for three frequencies of 11 GHz, 13 GHz, and 15 GHz. It can be seen that the NFCS has been very successful in the wideband phase correction, decreasing the phase error to 40^o at all three frequencies throughout the bandwidth. In relation to the near-field magnitude enhancement, 1-D magnitude distributions of the antenna, both with and without NFCS, are depicted in Fig. 2.9, showing that the deviation from a Cosine-Squared distribution has been significantly decreased.

Table 2.1: Optimized dimensions of NFCS, unit :millimeter

$h1$	$h2$	$h3$	$h4$	$h5$	$h6$	$h7$	$h8$	H_{Cavity}	H_{Gap}
22.2	34	28.8	24.8	20.3	17.7	10.1	6.1	16.3	1.7

Table 2.2: Optimization solution areas

Solution range of the height of phase regions	Solution range of H_{Cavity}	Solution range of H_{Gap}
$[0, 1.5\lambda_0]$	$[0.02\lambda_0, 0.07\lambda_0]$	$[0.02\lambda_0, 0.07\lambda_0]$

A prototype of the synthesized NFCS was fabricated and placed at a distance of 1.7 mm, chosen by the optimization algorithm, from the PRS, to verify the predicted

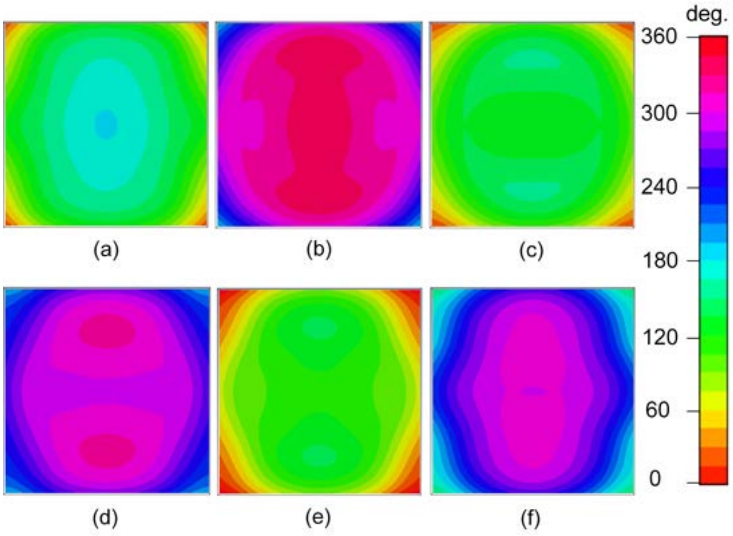

Figure 2.7: 2-D views of the near-field phase distribution for various frequencies at a distance of $2\lambda_0$ from the NFCS. (a) 10 GHz, (b) 11 GHz, (c) 12 GHz, (d) 13 GHz, (e) 14 GHz, (f) 15 GHz.

results computed by CST MWS. A photo of the antenna under NFCS loading is shown in Fig. 2.10, where its cavity is excited by a waveguide-fed slot placed in the center of the ground plane with dimensions of 14 $mm \times 9$ mm. The magnitude of the input reflection coefficient, shown in Fig. 5.8, was measured by an Agilent PNA-XN5242A vector network analyzer. The measured 10-dB return loss bandwidth extends from 9.66 GHz to 15.47 GHz, equal to 46%, showing good agreement with the predicted results. As can be seen, the introduction of NFCs has caused multiple resonances in S11, due to the non-uniform height of the correcting rings in the NFCS.

Far-field results of the antenna versus frequency are shown in Fig. 7.13, showing a peak measured directivity of 21.1 dB at 12.4 GHz. The 3-dB measured directivity bandwidth is 41%, from 10.35 GHz to 15.76 GHz. The measured gain bandwidth extends from 10.48 GHz to 15.70 GHz, which equals a fractional bandwidth of 40%, an outstanding improvement compared to other PCSs [21, 22, 25, 49, 50]. The measured peak gain is 20.6

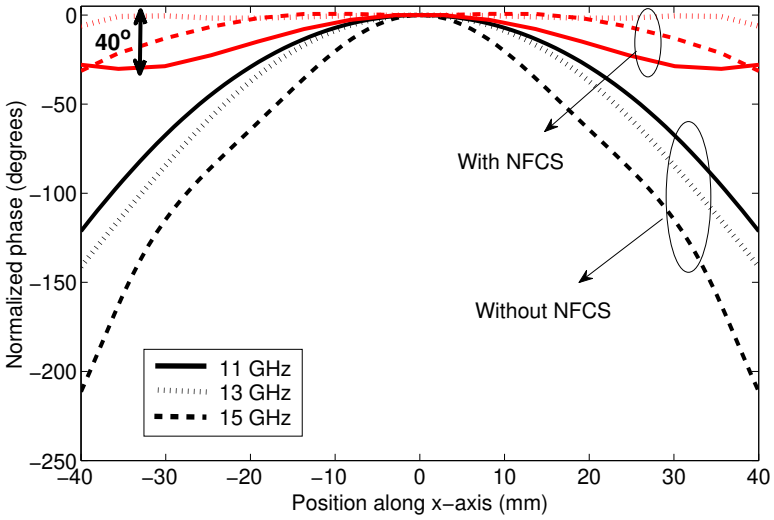

Figure 2.8: 1-D near-field phase distribution of the FPRA at a distance of $2\lambda_0$.

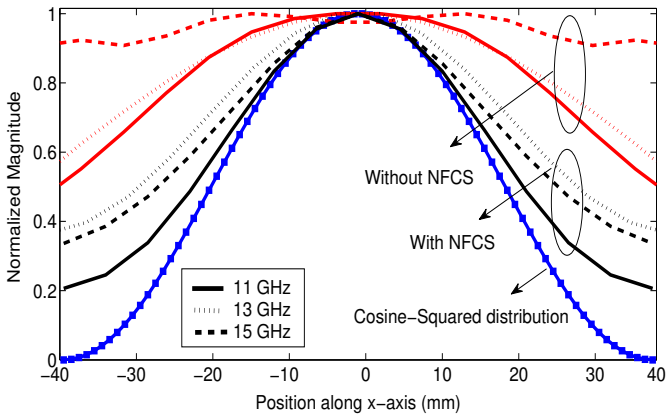

Figure 2.9: 1-D near-field magnitude distribution of the FPRA at a distance of $2\lambda_0$.

dB, showing a remarkable enhancement of almost 10 dB over the bare classical FPRA. The radiation patterns of the antenna under NFCS loading at 6 frequencies within the bandwidth are plotted in Fig. 2.13, showing stable SLLs, due to the successful near-field correction. It can be seen that the SLLs in the H and E-planes remain close to -20 dB and -11 dB, respectively, throughout the bandwidth. The area of the NFCS is $11.33{\lambda_{0c}}^2$ which is almost one third that of all other PCSs reported in [21, 25, 49, 50], where λ_{0c} is the free-space wavelength at the central frequency (13.09 GHz).

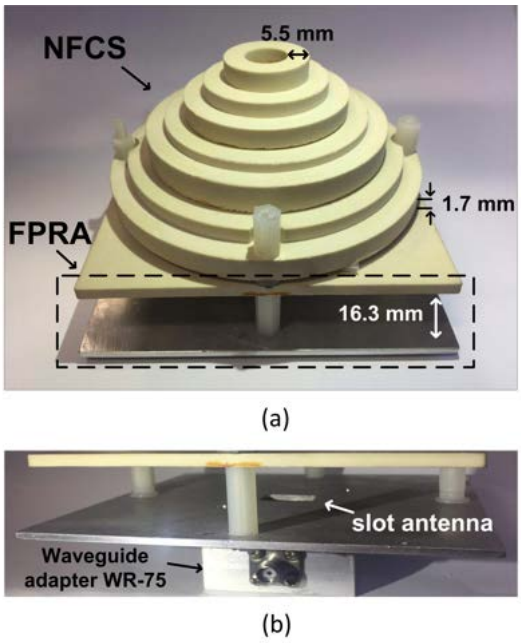

Figure 2.10: Photos of the fabricated prototype. (a) FPRA under NFCS loading. (b) Cross-sectional view of the feed antenna. The dimensions of the slot antenna placed in the center of the ground plane are 9 $mm \times 14$ mm. The pillars are insulating.

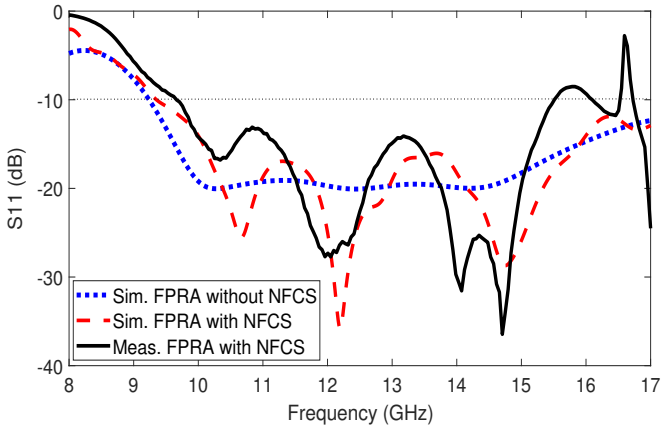

Figure 2.11: Magnitude of input reflection coefficient of the antenna.

2.6 Conclusion

A detailed systematic procedure of designing a wideband Near-Field Correction Structure (NFCS) for Fabry-Perot resonator antennas is presented for the first time. In this method,

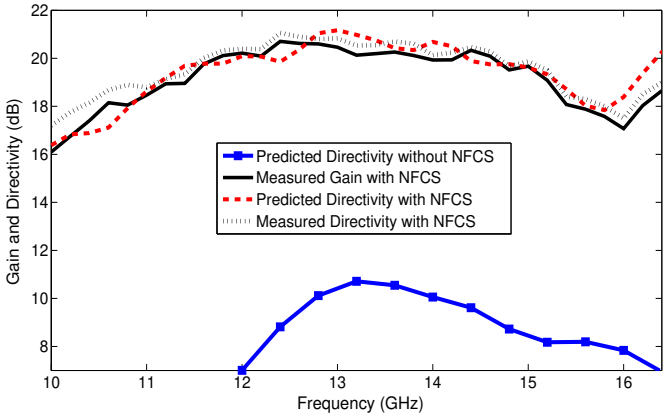

Figure 2.12: Gain and directivity of the antenna with and without NFCS.

a novel approach, based on the time-average Poynting vector and phase gradient analysis, is proposed to suggest the critical physical conditions of an NFCS to perform over a wide frequency band. Such conditions are then imposed on a customized PSO algorithm to correct the near-field phase errors and at the same time apply a Cosine-Squared distribution to the near-field magnitude. The NFCS synthesized has a large operational bandwidth of 40%, which is almost 300% larger than the bandwidth of other unit-cell based PCSs, while the NFCS is significantly smaller. The antenna system has a peak gain of 20.6 dB with a 3-dB gain bandwidth of 40%, extending from 10.48 GHz to 15.7 GHz, and stable SLLs in both planes, -20 dB and -11 dB in the H and E planes, respectively. The proposed method can also be used for near-field correction of other aperture antennas.

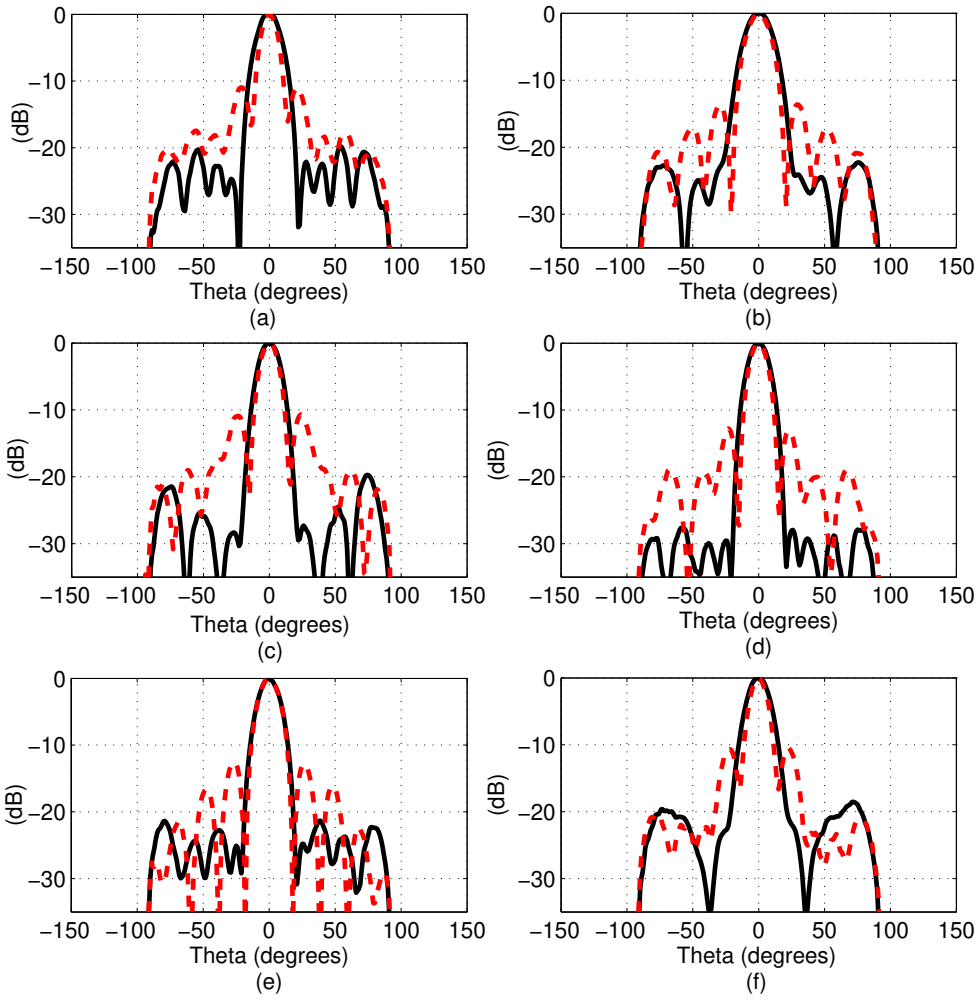

Figure 2.13: Measured radiation patterns at 6 distinct frequencies over the bandwidth. Solid and dotted lines represent H and E-planes, respectively. (a) 10.8 GHz, (b) 11.6 GHz, (c) 12.4 GHz, (d) 13.2 GHz, (e) 14.0 GHz, (f) 14.8 GHz.

CHAPTER 3

All-dielectric Beam-Scanning Metasurface

3.1 Abstract

The paper proposes an electromagnetic-wave beam-scanning antenna system using a simple rotation of a pair near-field graded-dielectric plates (GDPs). The antenna system requires an electromagnetic (EM) illuminator, with nearly symmetric aperture field distribution, as the base antenna and two types of GDPs: one radially graded dielectric (RGD) and two linearly graded dielectric (LGD) plates. The RGD first focuses the beam of the base EM illuminator in the broadside direction and the LGD then tilts the focused beam at an offset angle. For some types of base antennas, having fairly uniform aperture phase distributions, an RGD may not be required and only a pair of LGDs are sufficient. Irrespective of the antenna configuration, using simple rotation of the two LGDs, the beam can be scanned to any position within a large conical region. The antenna system presented as a proof of concept has a resonant-cavity antenna (RCA) as the base illumi-

Published as: Muhammad U. Afzal, Ali Lalbakhsh, Karu P. Esselle, "Electromagnetic-wave beam-scanning antenna using near-field rotatable graded-dielectric plates," *Journal of Applied Physics*, vol. 124, no. 23, pp. 912–915, Jul. 2018.

nator and three graded-dielectric plates. The aperture length of the antenna system is $6\lambda_0$ and its height is $2.2\lambda_0$. The results predicted by numerical simulations indicate that the antenna system has highest peak directivity of 21 dBi. The beam can be scanned to any direction within a cone having an apex angle of 82.2°.

3.2 Introduction

Beam-scanning high-gain antennas are widely anticipated for future wireless communication technologies such as the Fifth Generation of cellular communication (or 5G) and satellite internet services [78–81]. The beam-scanning ability at one or both ends of a communication link is inevitable also for energy-efficient smart wireless communication devices. Due to the immense growth of wireless systems and the anticipated expansion in the near future, this area of research is one of the most widely investigated topics in the field of wireless communication. In the quest of finding an efficient beam-scanning solution for high-gain antennas, several techniques have been investigated and are reported in the literature. Beam-scanning antennas can be classified into two broad categories, based on the method of operation: electrical and mechanical. Most of the widely used beam-scanning antennas are passive mechanically steered bulky reflector dishes, which occupy a large 3D volume [82]. On the other hand, the more-agile, slim, beam-scanning antennas are electronically scanned phased arrays, which are extremely lossy and expensive, particularly, at millimeter wave frequencies [83–85]. In general, electrical beam scanning is complex, lossy and expensive, but compact and convenient. Mechanical beam scanning is relatively cheap and more efficient than the electronic but bulky, heavy, and often slow due to the large inertia of the moving parts.

This paper simultaneously addresses the challenges faced with the two existing scanning techniques and presents a solution based on a third method of beam scanning. The solu-

tion is totally passive and thus possesses all the energy-efficient characteristics of a typical mechanically scanned antenna system. It needs to be clarified that the automated versions of this beam scanning system needs some power to drive motors to spin the plates. At the same time, its maximum height is extremely small and is comparable to that of electrically scanned systems based on printed arrays. The core of the solution is the dynamic near-field phase-transformation methodology, which has been recently demonstrated using printed planar metasurfaces [86].

Instead of metasurfaces, this paper explores the use of graded-index dielectric materials to presents an alternative all-dielectric beam-scanning antenna system. Graded-index dielectric materials have been investigated in the past to alter the optical beam of light [87,88]. One classic example is the dielectric lens, where a beam is focused by transforming a spherical phase front into a planar and vice versa [89–95]. The principle has been used here to develop graded-dielectric plates (GDPs) to focus and tilt the microwave beam of an EM illuminator in a particular direction. Two different types of GDPs are designed: radially graded dielectric (RGD) and linearly-graded dielectric (LGD) plates. A RGD focuses the beam of EM illuminator in the broadside direction and is also referred in the literature as transverse permittivity gradient phase-correcting structure (PCS) [96]. Depending on the radiation characteristics of an EM illuminator, the RGD may or may not be necessary. The beam-scanning is performed by a pair of LGDs where each LGD tilts the antenna beam at an offset angle away from the broadside direction. Simple rotation of a LGD pair scans beam to any position in a large conical space.

The operation of the proposed beam-scanning method, based on the rotation of an LGD pair, is similar to the optical beam-scanning method of Risley prisms [97–99]. A similar approach has also been used for scanning a microwave-antenna beam using thick dielectric wedges [100] and printed planar phase-shifting surfaces [101]. The total height of an antenna system based on printed phase-shifting surfaces that are located in the far-

field is $8.3\lambda_0$ (where λ_0 is the free space wavelength at the operating frequency), which is mainly because the surfaces are placed at several wavelengths from the radiating source. Although the electrical performance of the proposed antenna is similar to those reported earlier, the total height of the proposed antenna is only $2.2\lambda_0$ that is 74% shorter than the antenna having phase-shifting surfaces in the far-field. This is because the LGDs are placed at subwavelength spacing and within the near-field region of the EM illuminator. The proposed antenna may appear similar to variable-inclination continuous transverse-stub (VICTS) antennas [102, 103]. VICTS antennas have two rotating parts: an upper section with radiating stubs and a highly complex lower section with impedance matching elements, a line source, absorbers and a ground plane. The two parts of the antenna are rotated independently. Further, unlike VICTS antennas that require an external polarizer for a circularly polarized (CP) field, the proposed antenna configuration is compatible with both linear and circular base antenna without any additional component. Compared with a commercially available VICTS based antenna, which has maximum height of $7\lambda_0$ [104] at the lowest transmitting frequency, the maximum height of the proposed antenna in free space wavelengths is 69% less. It should be mentioned that the antenna system in [104] has a larger diameter. The proposed scanning technique is most closely related to the near-field scanning method presented using metasurfaces [86]. That near-field metasurface base antenna has a maximum height of $1.3\lambda_0$, which makes it the thinnest beam-steering antenna of this type and is 40% shorter than even the proposed beam-scanning method. However, in contrast to metasurfaces that are made of multi-layered printed phase-shifting unit cells, a simpler approach is used here and phase shifting is achieved by varying dielectric permittivities.

A detail description of this beam scanning method is given in Section II. Section III details design procedure of all GDPs used in this scanning method. Section IV presents a design example and Section V discusses the numerical results predicted using a commercially

available EM simulator. Finally, the paper is concluded in Section VI.

3.3 Beam Scanning Using GDPs

The core of the beam-scanning method is dynamic control of the electric near-field aperture phase distribution using GDPs. The technique is based on a pair of rotatable planar beam-tilting linearly graded dielectric (LGD) plates that are placed within a fraction of a wavelength spacing from an EM illuminator. An LGD is a simple planar plate of finite thickness having spatially distributed dielectric materials as shown in Fig. 3.1. The LGD has a permittivity gradient along one of the linear axes, referred to as the varying-permittivity axis (VPA) hereafter, and a constant permittivity along the other, orthogonal, axis. The plate when used with an EM illuminator that has a far-field beam in the broadside direction, simply tilts the beam in the direction of the VPA by an angle θ_o away from the broadside.

A complete 2D beam-scanning antenna system uses a pair of LGDs in a stacked configuration as shown in Fig. 3.2. The tilt angles introduced by LGD I and LGD II, denoted by δ_1 and δ_2, respectively, are the same and equal to θ_o, or $\delta_1 = \delta_2 = \theta_o$. The inter spacing between the LGD plates and between the illuminator and the first LGD plate is only fraction of a wavelength.

The directions of the VPAs in the xy-plane, representing the orientation of LGD I and LGD II, are denoted by ψ_1 and ψ_2. The angles ψ_1 and ψ_2 are measured in anticlockwise direction, from the positive x-axis to the arrow marking the VPA of the each LGD. The beam scanning in the azimuth and elevation planes by varying ψ_1 and ψ_2 is explained with three special cases below.

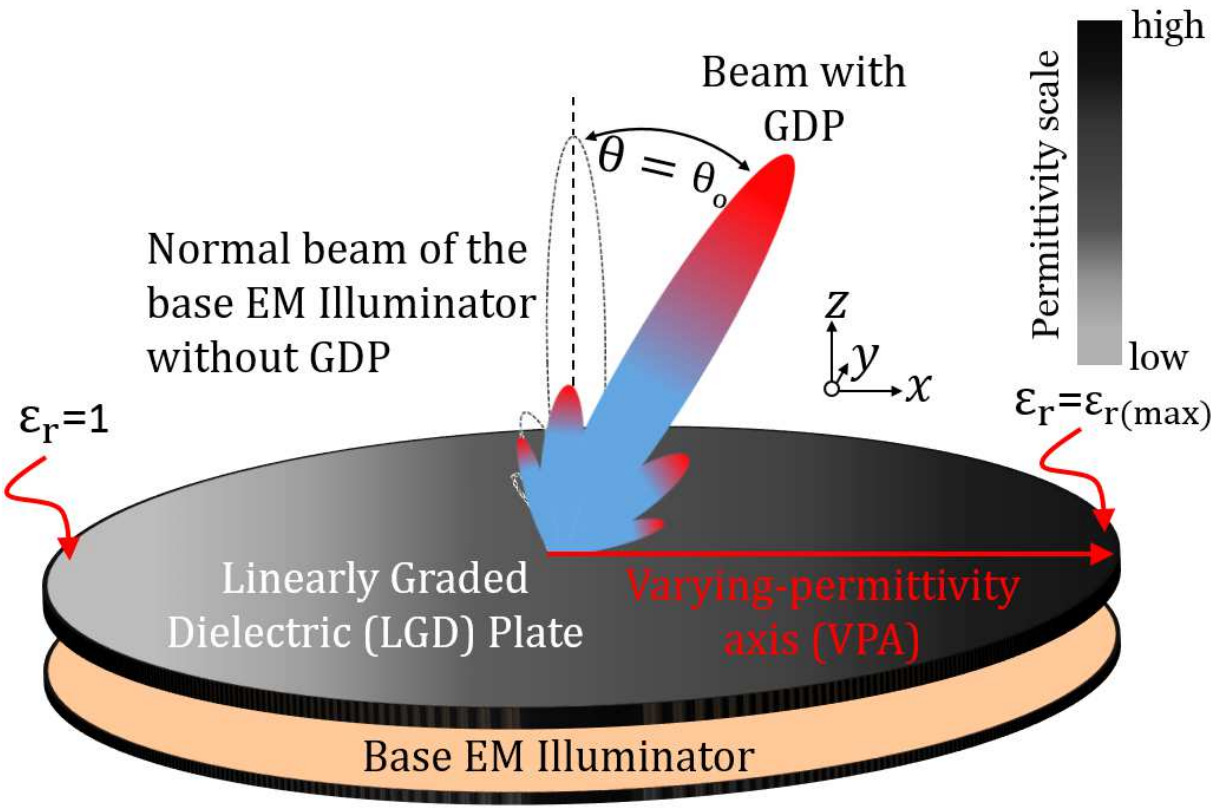

Figure 3.1: A view of beam-tilting linearly graded dielectric plate having uniform thickness but varying permittivity along a radial direction.

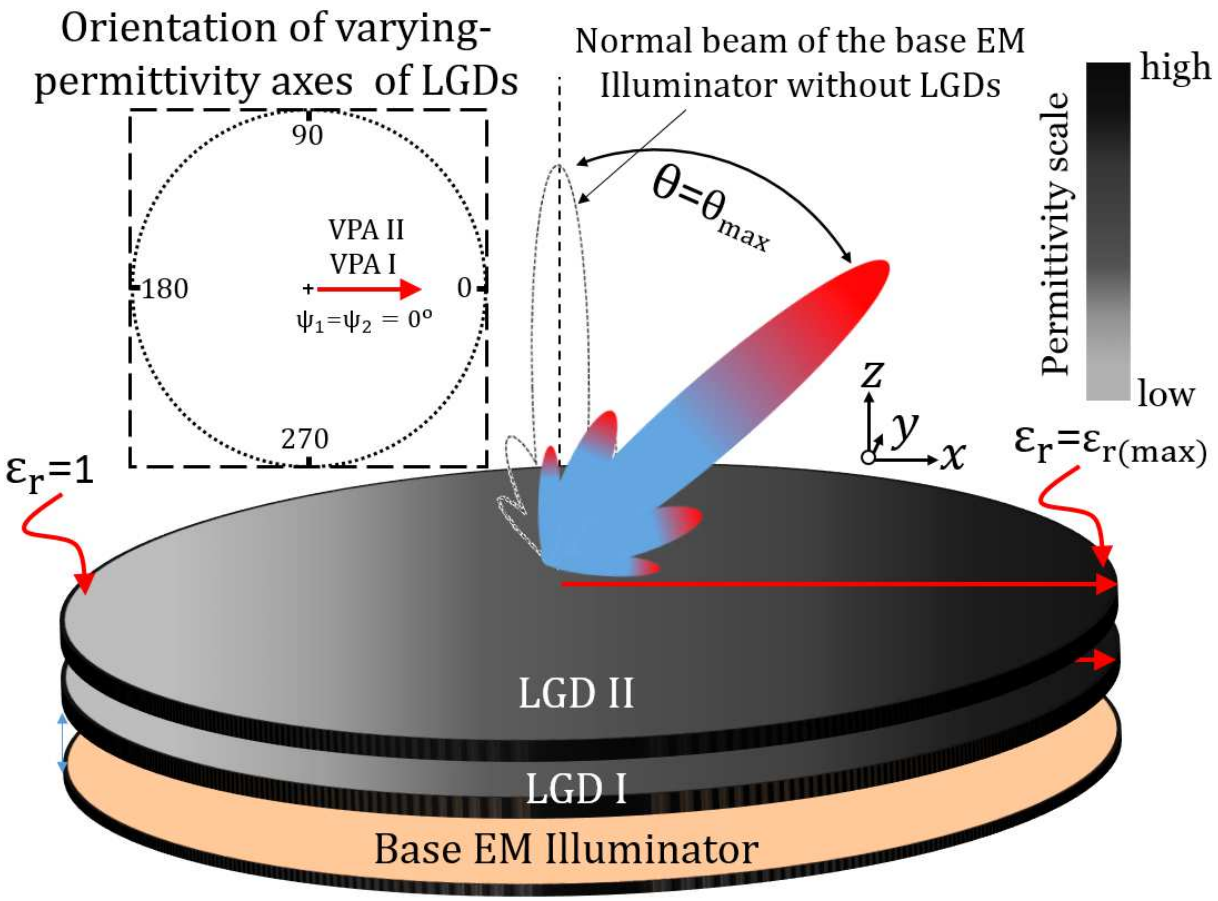

Figure 3.2: A perspective view of the beam-scanning antenna for maximum beam tilt in the elevation plane. The VPAs of the two LGDs are aligned in a radial direction.

3.3.1 Case I: Maximum Tilt

The maximum beam tilt away from the broadside is achieved when the VPAs of the two LGDs are co-aligned in a radial direction, or $\psi_1 = \psi_2$. The arrangement is pictorially represented in Fig. 3.2, where the VPAs are aligned along the x-axis of the Cartesian coordinates and $\psi_1 = \psi_2 = 0$. In this case, each LGD plate tilts the beam in the same elevation plane, thus constructively adding to maximize the beam tilt angle in the elevation plane and $\theta = \theta_{max}$. For LGDs with smaller tilt angles, θ_{max} is simply a sum of the beam tilt introduced by each LGD or $\theta_{max} = \delta_1 + \delta_2 = 2\theta_o$. For larger values of θ_o, or δ_1 and δ_2, θ_{max} will be more than than $2\theta_o$. This maximum tilt in the elevation plane can be achieved for any azimuth angle (or ϕ) between 0 and 360^o by simply rotating and aligning the VPAs of the two LGDs to the desired ϕ.

3.3.2 Case II: Minimum Tilt

The minimum beam tilt in the elevation plane is achieved when the VPAs of the two LGDs are pointing in opposite radial directions or when $\psi_1 - \psi_2 = 180^o$, as shown in Fig. 3.3. In this case, the two LGDs negate or cancel each others' tilt, as they tend to push the beam in opposite radial directions resulting in a minimum or no tilt at all. If the two LGDs are identical, or $\delta_1 = \delta_2$, the beam is scanned to the broadside direction. However, if the two LGDs are not identical, meaning $\delta_1 \neq \delta_2$, the beam peak is scanned to minimum elevation angle, or θ_{min}.

3.3.3 Case III: Intermediate Tilt

For any orientation other than the two mentioned above, the beam out of the LGD pair is scanned to an intermediate elevation and at a distinct azimuth angle, i.e. θ, ϕ. As an example, if the VPA of LGD I is fixed along the x-axis or $\psi_1 = 0$ and ψ_2 has any value

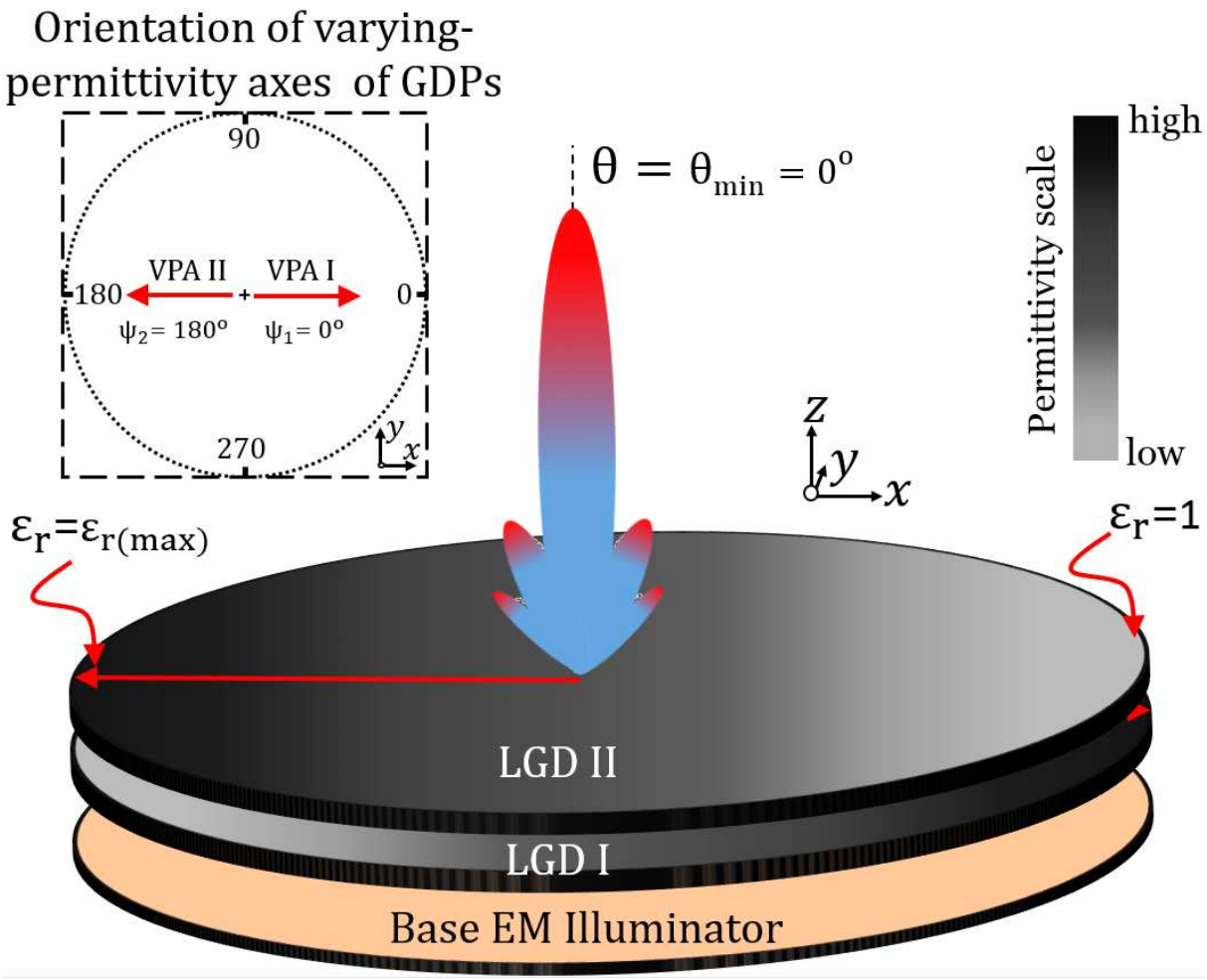

Figure 3.3: A view of the beam-scanning antenna for minimum or no tilt in the elevation plane. The VPAs of the two LGDs are pointing in opposite radial direction.

between 0 and 180° then the elevation angle of the beam has a value between 0° and θ_{max}. The exact values of the azimuth and elevation angles can be estimated using ψ_1, ψ_2, δ_1, and δ_2 using the method explained below.

The method is based on the first-order paraxial approximation and vector addition [99]. In this method a pair of vectors is used in the 2D ij-plane – one vector for each LGD – as explained in an earlier publication [86]. The first vector, associated with LGD I, has magnitude proportional to δ_1 and angle ψ_1. The second vector, associated with LGD II, has magnitude proportional to δ_2 and the angle ψ_2. The two vectors are added to calculate the resultant vector, and the magnitude and the angle of the resultant vector are then used to find θ and ϕ of the beam peak, respectively. The Cartesian components of the resultant vectors are given as:

$$\delta_i = \delta_1 \cos(\psi_1) + \delta_2 \cos(\psi_2) \tag{3.1}$$

$$\delta_j = \delta_1 \sin(\psi_1) + \delta_2 \sin(\psi_2) \tag{3.2}$$

The two Cartesian components are used to compute θ and ϕ:

$$\theta = \sqrt{{\delta_i}^2 + {\delta_j}^2} = \sqrt{{\delta_1}^2 + {\delta_2}^2 + 2\delta_1\delta_2 \cos(\psi_1 - \psi_2)} \tag{3.3}$$

$$\angle OC = \tan^{-1} \frac{|\delta_j|}{|\delta_i|} = \tan^{-1} \frac{|\delta_1 \sin(\psi_1) + \delta_2 \sin(\psi_2)|}{|\delta_1 \cos(\psi_1) + \delta_2 \cos(\psi_2)|} \tag{3.4}$$

$$\phi = \begin{cases} \angle OC & \delta_i \geq 0 \ \& \ \delta_j \geq 0 \\ 180^\circ - \angle OC & \delta_i < 0 \ \& \ \delta_j \geq 0 \\ 180^\circ + \angle OC & \delta_i < 0 \ \& \ \delta_j < 0 \\ 360^\circ - \angle OC & \delta_i \geq 0 \ \& \ \delta_j < 0 \end{cases} \tag{3.5}$$

3.4 Components of the Beam-Scanning Antenna

The beam-scanning solution discussed above is based on a rotatable pair of LGDs. As mentioned before, for an EM illuminator that has a fairly uniform phase of the electric field, a pair of LGDs are sufficient. However, an EM illuminator that radiates an electric field with a non-uniform aperture phase distribution needs an additional RGD plate to first create a uniform phase for the LGD plates. Since the RGD is required with most of the base EM illuminator, the design procedure of RGD is explained in detail along with the LGD in this section.

3.4.1 Radially Graded Dielectric (RGD) Plate

A radially graded dielectric (RGD) is a circular plate with a finite physical aperture matching that of base EM illuminator. A RGD atop a base EM illuminator transforms its non-uniform aperture phase distribution into a nearly uniform phase distribution, resulting in a focused broadside beam. Unlike traditional phase-correcting techniques, such as those used with optical lenses, the RGD plate is based on near-field transformation methodology. The prime advantage of the near-field phase-transformation technique is that the RGD is placed at a sub-wavelength spacing from the illuminator [105–107]. Thus the RGD, being a part of the illuminator, does not increase the maximum height of the illuminator.

An RGD carries out the phase transformation by providing a spatially distributed transmission-phase delay. The transmission-phase delay through the RGD is due to the radially distributed dielectric materials $\varepsilon_r(r)$. It is known that the phase delay in a dielectric material depends on the length of the dielectric and the relative permittivity value. Therefore, a differential phase delay in an RGD can be established by spatially distributing dielectrics with the same length but having different permittivity values. The spatial distribution of dielectric material in on RGD is only along a radial direction. A pictorial representation

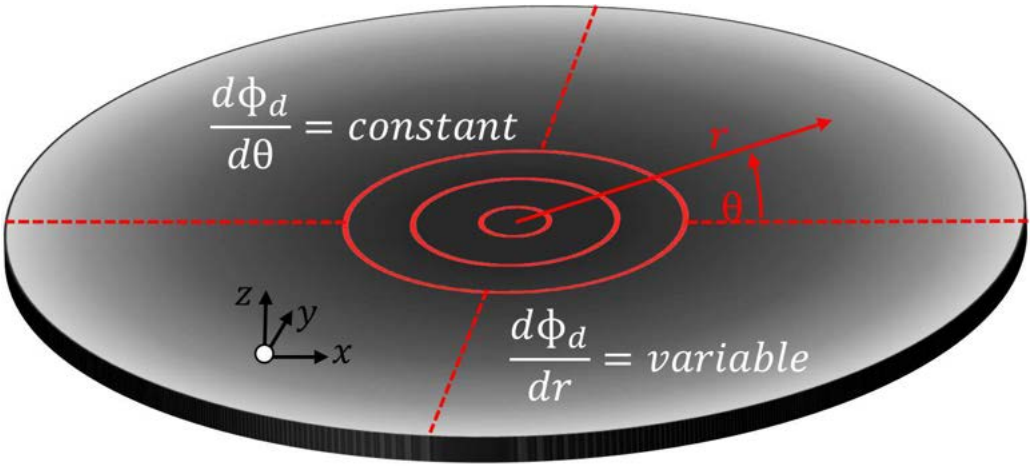

Figure 3.4: A perspective view of radially graded dielectric (RGD) material. The relative permittivity of the RGD varies radially outward from the center to the edges.

of the RGD plate is shown in Fig. 3.4. The transmission-phase delay in an RGD is represented by ϕ_d and can be expressed as a function of the radial distance r from the center of aperture such that $d\phi_d/dr = variable$ [108]. The radial dielectric and phase variation of the RGD plate, or $d\phi_d/dr$, corresponds to the phase non-uniformity of the base EM illuminator. Ideally the transmission-phase delay variation in the RGD must be continuous along the radial direction. However, because of the complexity in implementing and designing such structures, the RGD is divided into discrete concentric circular sections, each having a width of $\lambda_0/3$, which is small enough to correct the phase errors throughout the antenna aperture. The RGD is designed follwing procedure explained for PCSs [105]. First a virtual plane is defined on the aperture of the base EM illuminator, as depicted in Fig. 3.5. The actual phase of the field radiated by the illuminator is predicted in the virtual plane using numerical electromagnetic (EM) simulators. The phase is sampled precisely at the points lying at the center of the circular concentric sections of the RGD. The phase is then used to calculate the phase delay, or $\phi_d(r)$, required from the RGD to achieve a uniform phase at its output. Once the phase-delay profile is known then appropriate permittivity values are determined for normal field propagation through a dielectric material. Electric field through a dielectric material is analysed in [109] – the

analysis has been used to derive a simplified phase-delay equation:

$$\phi_d(\varepsilon_r, h) = \angle\left(\cos(k_d h) + j\sin(k_d h)\left(\tfrac{1+\varepsilon_r}{2\sqrt{\varepsilon_r}}\right)\right), \tag{3.6}$$

where $h = h_0$ is the fixed height of the dielectric material and k_d is the guided wavenumber inside the dielectric, or $k_d = k_0\sqrt{\varepsilon_r}$. Through (3.6), phase data is first plotted by fixing h and varying ε_r between $\varepsilon_r = \varepsilon_{r(min)} = 1$ to $\varepsilon_r = \varepsilon_{r(max)}$. For convenience, the phase data is unwrapped and normalized with the minimum phase value, or $\phi_{d(min)} = \phi_d(\varepsilon_{r(min)}, h_0)$, so that the absolute phase-delay range can be calculated. The normalized phase-delay plot can then be used to find values of ε_r against $\phi_d(r)$ for each section of the RGD.

3.4.2 Linearly Graded Dielectric (LGD) Plate

An LGD tilts the broadside beam to an offset angle away from the broadside – pictorially depicted in Fig. 3.1. The LGD achieves this beam tilt by introducing a laterally varying phase delay $\phi_d(x, y)$ that transforms a uniform phase at its input into a linearly increasing phase at its output – a concept inspired from phased arrays in the microwave antenna regime.

In a 2D phased array, a relative phase difference is introduced between antenna elements using

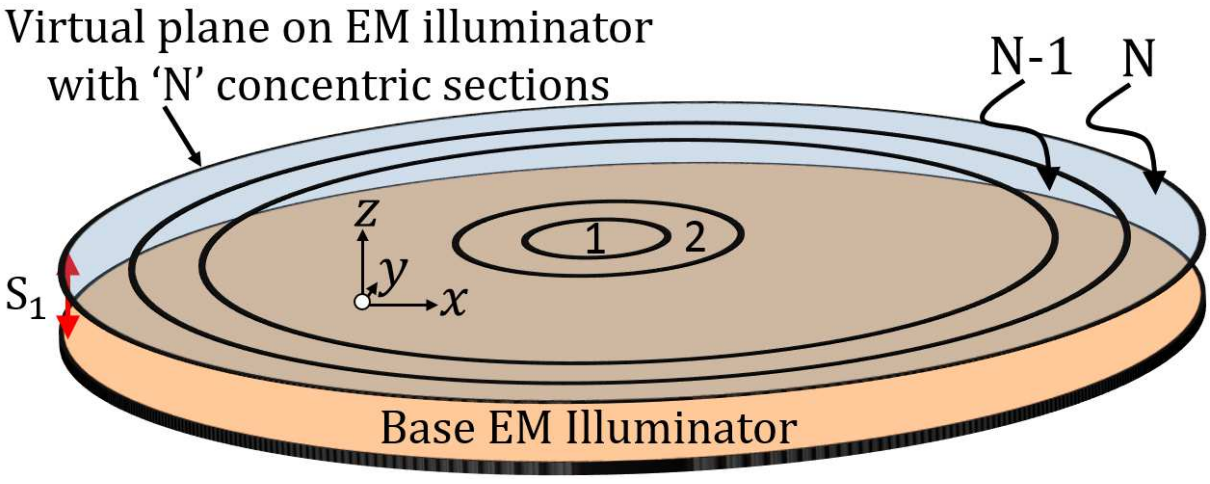

Figure 3.5: Virtual plane defined for base EM illuminator for probing non-uniform electric near-field aperture phase distribution.

phase shifters. The resulting interference pattern of the field radiated by the antennas and the direction of constructive interference in the far field is directly controlled by the phase shifts. An LGD mimics the 2D phase-shifter network of a phased array, with the subtle difference that the LGD introduces the phase shift in the radiated field, unlike a phase shifter that inserts a desired phase in the guided wave before it is radiated.

To mimic a 2D array, the aperture of the LGD is divided into discrete grid using Cartesian coordinates, as shown in Fig. 3.6. In the example shown in Fig. 3.6, the dielectric varies along the x-axis (labelled as VPA) and is constant along the y-axis. The permittivity is varied such that the phase delay in the LGD has a constant gradient along the x-axis or $d\phi_d/dx = c$ (where c is a constant). Similarly to the RGD, first the required phase-delay profile of the LGD is calculated using array theory. The array theory states that for two antenna placed side by side at a spacing of d, the beam can be made to interfere constructively at an angle θ_o by introducing

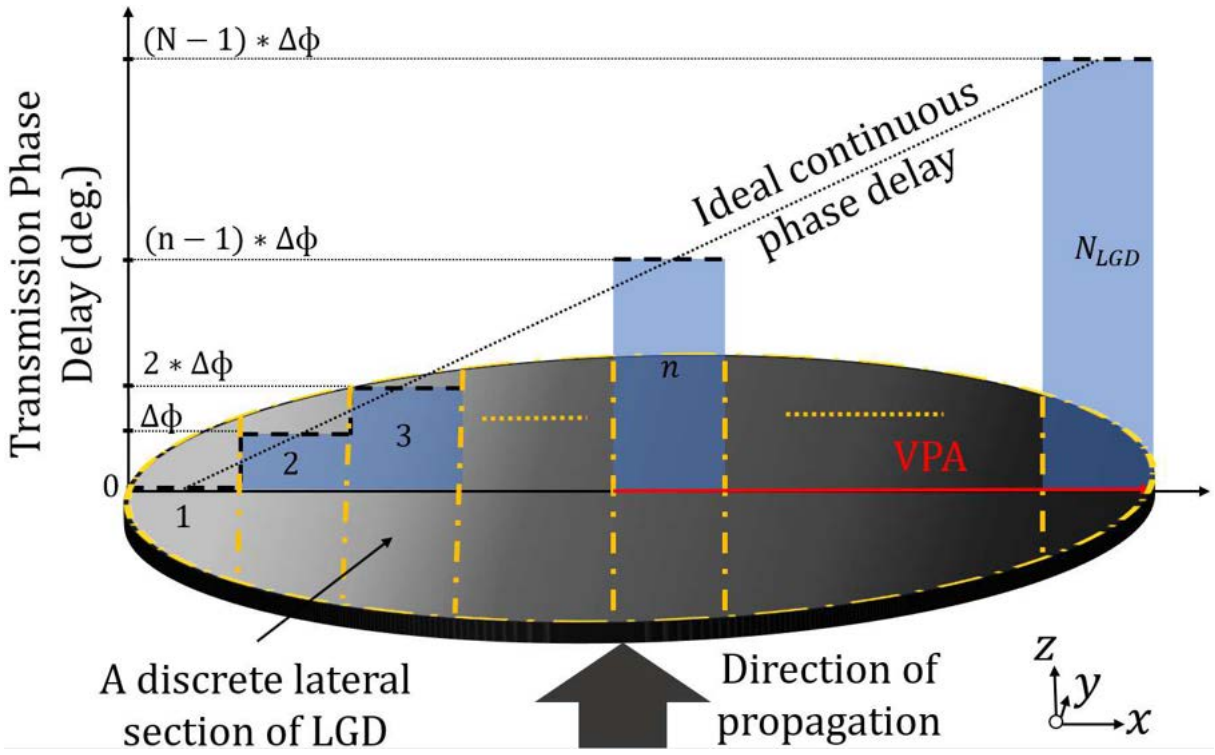

Figure 3.6: Transmission phase-delay along the varying-permittivity axis of the LGD plate. Transmission phase delay is visually depicted by rectangular bars.

a relative phase difference ($\Delta\phi$), given as:

$$\Delta\phi = \frac{2\pi}{\lambda} d \sin\theta_o \tag{3.7}$$

$\Delta\phi$ is the gradient of the LGD's phase-delay profile. For the purpose of mapping the phase delay on the aperture of the LGD, the section at one extreme of the LGD is assigned a transmission-phase delay of 0^o and all the subsequent sections have an incremental phase value of $\Delta\phi$ as shown in Fig. 3.6. The value of the dielectric permittivity is then estimated following procedure similar to that explained for the RGD.

3.5 Example

To verify the working of the proposed beam-scanning antenna, a design example is presented. The antenna is designed to operate in X-band at a frequency of 11 GHz. The base EM illuminator of the system is a classic resonant-cavity antenna (RCA). In the antenna community, the RCA is also known by the name of Fabry-Perot antenna, electromagnetic bandgap resonator antenna, and partially reflecting surface antenna [110–114].

The RCA comprises a simple patch, as an EM source, with a circular full ground plane and an all-dielectric reflecting superstrate, as shown in Fig. 3.9. The patch is printed on 0.787 mm thick Rogers 5880 substrate and the superstrate is a circular unprinted 3.17 mm thick slab of Rogers TMM4. The diameter of the superstrate and the ground plane is $6\lambda_0$ and both are separated by a physical spacing of $\sim \lambda_0/2$ or $t = 12.4$ mm. The spacing is essential for the cavity, formed between the ground plane and the superstrate, to resonate at the operating frequency. This type of classical RCA is known to have a non-uniform electric near-field aperture phase distribution [86]. Therefore, an RGD was required with the pair of LGDs to scan the RCA beam.

3.5.1 RGD Plate

The RGD is designed following procedure explained above and reported in publications on PCSs [96, 105]. A virtual plane of $6\lambda_0$ diameter (matching that of base illuminator) is defined at a spacing of $\lambda_0/4$ from the PRS, or $S_1 = \lambda_0/4$. The plane is discretized into nine concentric radial sections, each having a width of $\lambda_0/3$, as shown in Fig. 3.5. The RCA was simulated with the finite-integration technique (FIT) based solver of CST Microwave Studio.

The phase of the dominant field component (E_y) was computed at the center of each section along the x-axis in the virtual plane. The phase is normalized and is plotted along the physical position on the aperture in Fig. 3.7. This phase is symmetric around the antenna center and can be referred as input phase, or $\phi_{in}(r)$. The input phase data is then used to calculate the phase-delay profile, or $\phi_d(r)$, of the RGD plate such that a uniform output phase, or $\phi_{out}(r) = \phi_o$, is obtained at the output of the RGD. The $\phi_d(r)$ is related to the $\phi_{in}(r)$ and $\phi_o(r)$ with a simple relation $\phi_d(r) = \phi_{in}(r) - \phi_o$. The ϕ_o can be any value smaller than or equal to the minimum value of $\phi_{in}(r)$. The value of ϕ_o used here is 285.5°. The $\phi_d(r)$ is plotted in Fig. 3.7 and is given along the region numbers in Table 3.1. To estimate the appropriate permittivity value in each radial section, the phase delay in an ideal dielectric slab is first analytically computed using (6). In (6), h (or the dielectric thickness) is a fixed variable and is critical because it affects the $\varepsilon_{r(max)}$ required for the design. To elaborate this point further, the phase delay (ϕ_d) in a dielectric is calculated, using (6), for several values of h and a fixed range of ε_r between 1 and 40. For each iteration, the phase data is unwrapped and normalized so that the absolute achievable phase-delay range ($\phi_d(max) - \phi_d(min)$) can be easily obtained. The data obtained from this analysis is given in Table 3.2. As can be seen from the table, the phase-delay range increases with increasing dielectric height for a fixed permittivity variation. It can be concluded that, for a large required phase delay, thicker dielectric must be used if a limited range of ε_r is available. In the case of the RGD, the phase range required is 286°. For any fixed dielectric height, the range of ε_r that provides a normalized phase delay of more than 286° is sufficient for this RGD design.

Table 3.1: Phase of the dominant field component radiated by the RCA and transmission-phase delay compensation calculated to improve phase uniformity.

Region No.	Input phase (Deg.)	Phase delay (Deg.)(ϕ_d)	ε_r
1	0	285.5	9.3
2	-28.2	257.3	8.3
3	-68.8	216.7	7.1
4	-98.2	187.3	6.2
5	-132.9	152.6	4.8
6	-139.1	146.4	4.5
7	-187.5	98	2.9
8	-285.4	0.1	1
9	-134.1	151.4	4.7

Table 3.2: Phase delay range for several thickness and fixed permittivity range.

h(mm)	h (λ_0)	ϕ_d range ($\phi_{d(max)} - \phi_{d(min)}$ (Deg.))
5	0.18	373.7
10	0.37	687.9
15	0.55	1071.9
20	0.74	1435.4
25	0.92	1749.6
30	1.1	2142.9

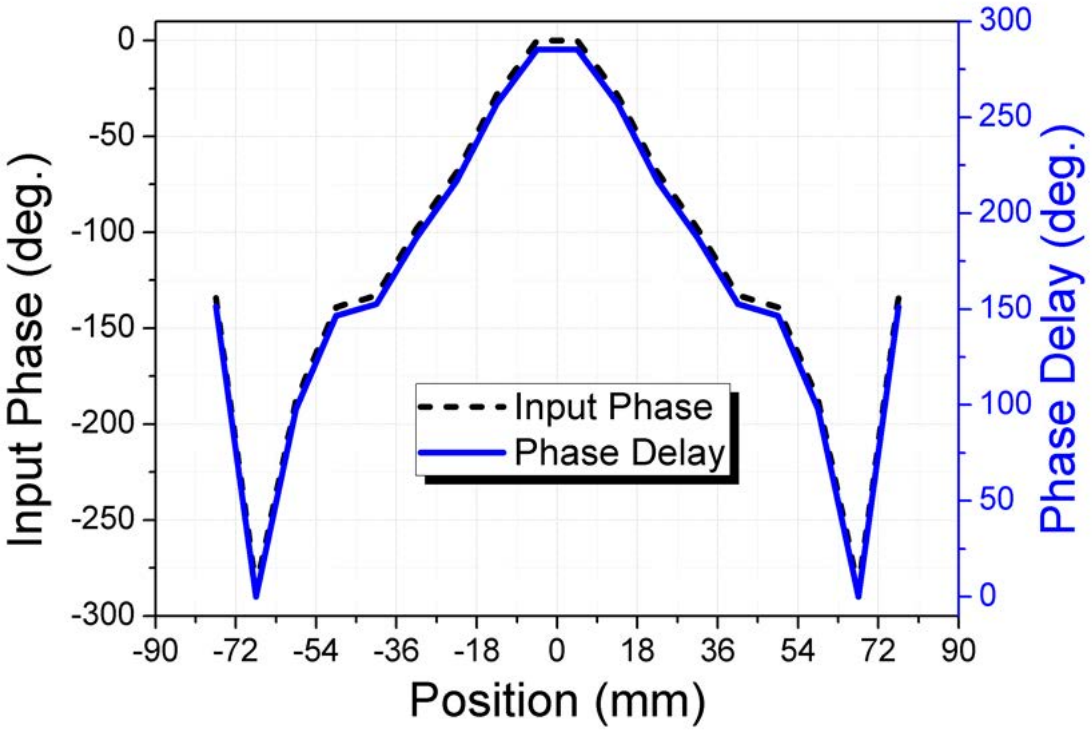

Figure 3.7: Non-uniform phase of the dominant electric field (E_y) component on RCA aperture and the required transmission-phase delay of the RGD.

For the RGD and LGD designs, the dielectric thickness is set to 10 mm and ε_r is varied between 1 and 40. The phase delay ϕ_d is computed using (6). A plot of unwrapped normalized phase delay against ε_r is shown in Fig. 3.8. As can be seen from the figure, the phase-delay range of 286^o can be achieved by varying ε_r between 1 and 10. Using the phase-delay plot, the exact values of ε_r were selected for the required phase delay in each radial section of the RGD. The values of ε_r are given in the last column of Table 3.1.

A 3D model of the RGD plate was created with the RCA and radiation performance was numerically predicted using finite-integration technique (FIT) based solver of CST Microwave Studio. Using the numerically predicted results, the thickness of the RGD was further optimised to 6.5 mm. A 3D model of the RCA with optimised RGD is shown in Fig. 3.9. Radiation perfor-

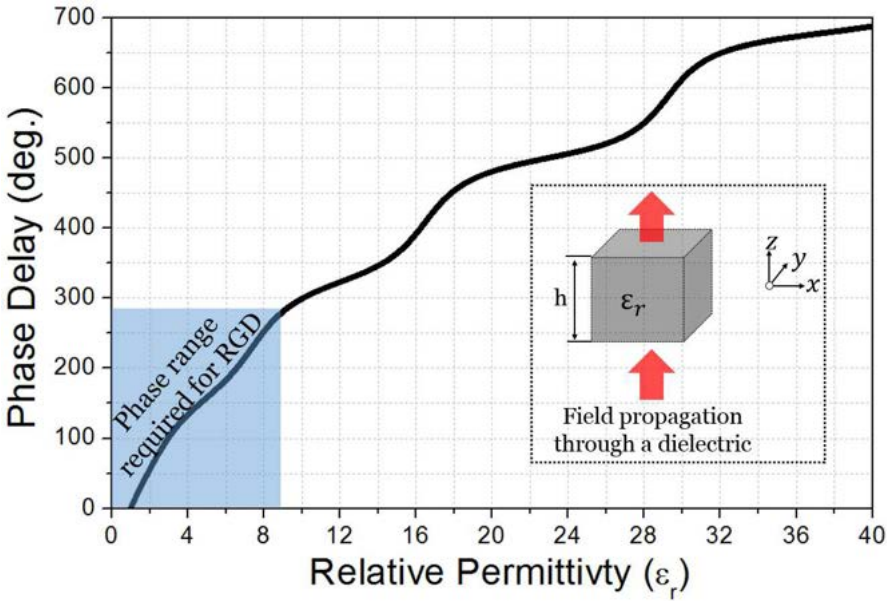

Figure 3.8: The transmission-phase delay through a dielectric material having varying permittivity and fixed thickness.

mance of the optimised antenna is verified using an independent finite-element method (FEM) based full-wave solver of CST Microwave Studio, in addition to the use of FIT based CST solver. These numerically predicted results will be discussed in Section V.

3.5.2 LGD Plate

To complete the beam-scanning antenna, a pair of identical LGDs are designed, each having a beam tilt angle of 20° or $\theta_o = 20°$. The physical layout of the LGD plate is based on the description given in Section III. The LGD has a physical aperture same as RCA and the RGD, i.e. $6\lambda_0$ diameter. The aperture is divided into eighteen vertical section, or $N_{LGD} = 18$, each having a width of $\lambda_0/3$. The phase-delay gradient across vertical sections is calculated using (7). At the operating frequency, to create a tilt of 20° this phase is 41°, or $\Delta\phi = 41°$. From this value, the transmission-phase delay of the entire LGD plate is obtained by progressively increasing the phase delay of each dielectric section with a step of 41°, starting from 0°. The values of the phase delay in vertical sections of the LGD along with the center position of each section is given in

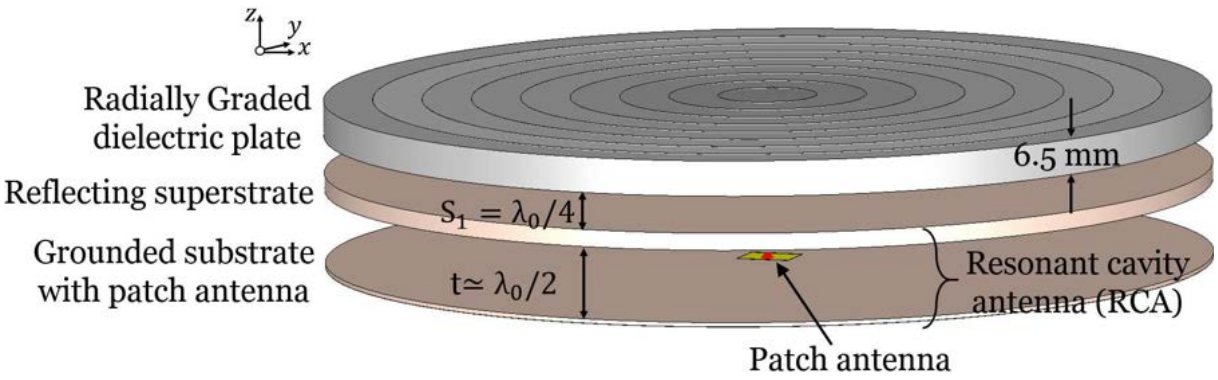

Figure 3.9: Models of the RCA and RGD used for numerical simulations.

Table 3.3 – the physical center of the plate lies at the origin of the coordinate system. Unlike RGD, the maximum transmission-phase delay required for the LGD is $\sim 700^o$. To obtain this value of transmission-phase delay with a 10 mm thick dielectric material, the maximum value of relative permittivity is 40 or $\varepsilon_{r(max)} = 40$. The value of $\varepsilon_{r(max)}$ can be reduced by wrapping the transmission-phase delay between 0 and 360°. In the case of the wrapped transmission-phase delay the maximum value of relative permittivity is 15 or $\varepsilon_{r(max)} = 15$. The phase wrapping, however, has its own technical challenges such as amplitude modulation and propagation of undesired Floquet modes – these aspects are not investigated here and are beyond the scope of this work.

The normalized phased delay plot of Fig. 3.8 was used to find exact values of dielectric permittivity against the ϕ_d for the LGD, which are given in Table 3.3. A 3D model of the LGD pair was created and used with 3D models of RCA and RGD as shown in Fig. 3.10. The spacing between the RGD and LGD I and between LGD I and LGD II was optimised to $0.09\lambda_0$ or $S = 2.5$ mm. The thickness of two LGDs is not optimised further due to very long simulation times and may be carried as an extension to this work in the future. It should be mentioned that dielectric materials with relative permittivity greater than 12 are difficult to fabricate and are likely to be heavy.

3.6 Radiation Performance

The radiation performance of the antenna system (RCA with GDPs) is numerically predicted at the operating frequency using the FIT-based solver of CST Microwave Studio.

Table 3.3: Transmission phase delay in a LGD plate and permittivity values of the dielectric materials within various sections.

Region No.	Region center	Phase delay (ϕ_d) (Deg.)	ε_r
1	-76.5	0	1
2	-67.5	41	1.7
3	-58.5	82	2.5
4	-49.5	123	3.6
5	-40.5	164	5.2
6	-31.5	205	6.7
7	-22.5	246	7.8
8	-13.5	287	9.3
9	-4.5	328	12.5
10	4.5	369	15.2
11	13.5	410	16.5
12	22.5	451	17.9
13	31.5	492	21.6
14	40.5	533	27.1
15	49.5	574	28.8
16	58.5	615	30.1
17	67.5	656	32.7
18	76.5	697	40

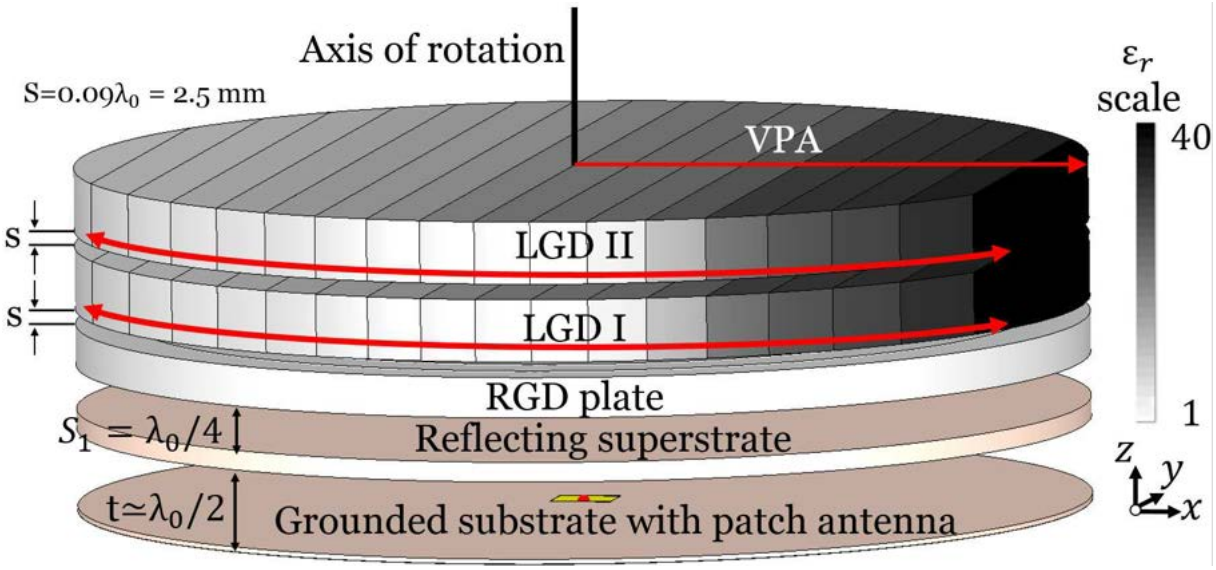

Figure 3.10: Final configuration of the beam-scanning antenna system, comprises 3D models of the RCA, RGD, and a pair of LGDs.

Initially, 3D models of the RCA and the RGD (shown in Fig. 3.9) were simulated and key performance indicators such as aperture phase distribution and far-field directivity patterns were extracted. The phase of the dominant radiated-field component (E_y) was computed at a spacing of $0.2\lambda_0$ above RGD along the x-axis and is plotted in Fig. 3.11. For comparison, the phase of the same field component radiated by the RCA without the RGD is also included in the figure. A noticeable uniformity in the phase is achieved with the RGD, having maximum efficiency in the central region of the aperture.

The physics of aperture antennas states that an aperture that radiates a perfect plane wave – a wave that has parallel wave fronts – has most directive radiation in the far field. The peak directivity of the RCA with the RGD is $\sim$ 23 dBi, which was only 12 dBi without the RGD. The numerical results predicted by FIT-based solver were verified with an independent Finite-Element Method (FEM) based solver of CST Microwave Studio. The exact values of parameters such as peak directivity, 3dB beamwidth and sidelobe levels predicted by both solvers and are compared in Table 3.4. As can be observed from the table, the peak directivities predicted by the two solvers differ by 0.1 dB. The 3dB beam width in both principal planes has a difference

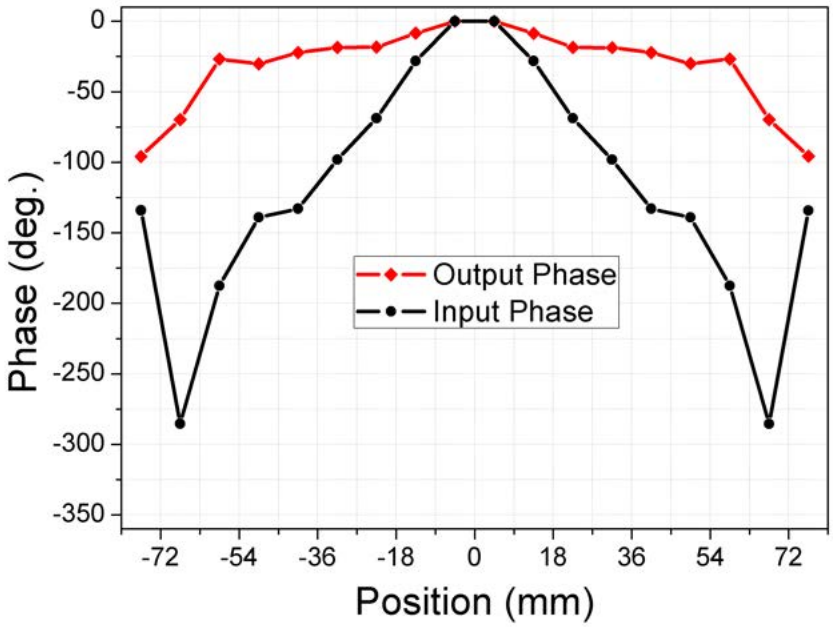

Figure 3.11: Phase of the field radiated by the base EM illuminator with and without RGD plate.

of 0.3 dB and the SLLs are nearly identical. The pattern cuts in the E-Plane differ beyond the main beam direction. These discrepancies can be attributed to the difference between Tetrahedral and Hexahedral meshes implemented by the FEM and FIT solvers, respectively. It should be mentioned that the higher SLLs in the E-plan patterns are due to the feed of the antenna system and not the scanning plates.

For beam scanning, the 3D model of antenna system shown in Fig. 3.10 was simulated with the FIT based CST simulator. The RCA (base EM illuminator) and the RGD are fixed, and LGD I and LGD II are rotated around the antenna axis. The scanning of beam peak, in an angular position (θ, ϕ) within a conical region, is explained with three rotation modes.

Table 3.4: Comparison of far-field radiation characteristics predicted by numerical solvers based on FEM and FIT.

Parameters	E-Plane		H-Plane	
	FIT	FEM	FIE	FEM
Peak directivity (dBi)	22.9	22.8	22.9	228
3dB Beamwidth (deg.)	12.2	11.9	13.4	13.6
SLLs (dB)	-20.2	-20.2	-26.4	-26.9

3.6.1 Mode I

To scan the azimuth and elevation plane together, LGD I is fixed and LGD II is rotated in an anticlockwise direction with a fixed step, or $\psi_1 = 0^o$ and $\psi_2 = 0^o, 30^o \ldots, 180^o$. At each combination of ψ_1 and ψ_2, the beam peak moves in both azimuth and elevation planes to a distinct θ and ϕ. Far-field patterns are predicted by numerical simulations. All the elevation cuts, taken at azimuth angles, containing beam peaks are plotted in Fig. 3.12. When $\psi_1 = \psi_2 = 0^o$, the beam peak is scanned furthest in the elevation plane, or $\theta = \theta_{max}$, and at an azimuth angle $\phi = 0$. With increasing ψ_2, the beam peak moves closer to the broadside direction, traversing through a series of intermediate (ϕ, θ) points. The azimuth angles (or ϕ) of the beam peaks are given in the legend of Fig. 3.12. The elevation angle (or θ) is the position of the beam peak on the horizontal axis of Fig. 3.12. The highest peak directivity of 20 dB is achieved when the beam is in the broadside direction for $\psi_1 = 0^o$ and $\psi_2 = 180^o$. The minimum peak directivity of 17 dBi is when the beam is scanned furthest in the elevation for $\psi_1 = 0^o$ and $\psi_2 = 0^o$. The precise angular position of the beam peak predicted by numerical simulation and that estimated using equations (1) – (5) are given in Table 3.5.

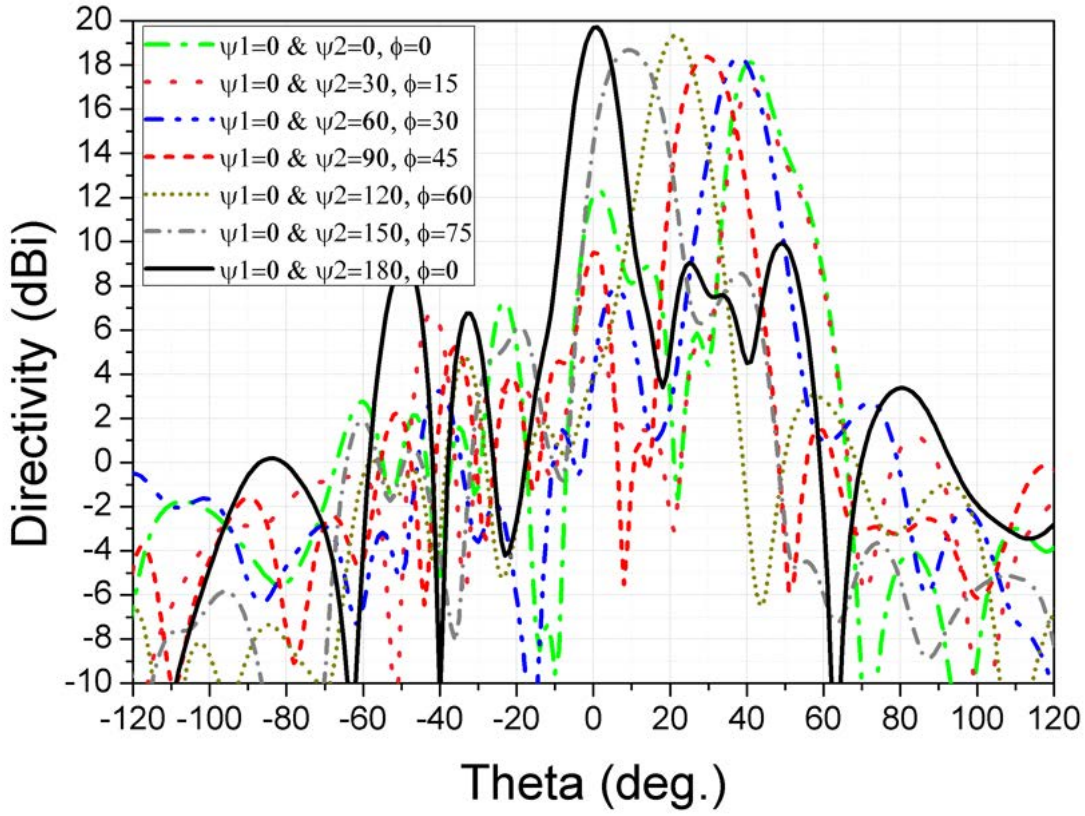

Figure 3.12: Elevation cuts taken at azimuth angles containing the beam peak. For each pattern cut, the azimuth angle and the orientation angles of LGD I and LGD II are given in the legend.

3.6.2 Mode II

To scan the beam only in the elevation plane, without affecting the azimuth angle, the two LGDs are rotated with equal magnitude but in opposite directions. If LGD I is rotated clockwise then LGD II must be rotated anticlockwise with the same value, or $\psi_1 = -\psi_2$. To verify the elevation-only scan, numerical simulation was carried for several combinations of ψ_1 and ψ_2. ψ_1 is varied between 0^o and 90^o with a step of 15^o and ψ_2 is varied between 0^o and -90^o with a step of -15^o. For each combination of ψ_1 and ψ_2, the radiation performance is numerically

Table 3.5: Angular position of beam peak predicted by numerical simulations.

Orientation of LGDs		Estimated		Predicted	
ψ_1(deg.)	ψ_2(deg.)	ϕ(deg.)	θ(deg.)	ϕ(deg.)	θ(deg.)
0	0	0	40	0	41.5
0	30	15	38.6	15	40.91
0	60	30	34.6	29	37.9
0	90	45	28.3	45.5	29
0	120	60	20	61.8	21.8
0	150	75	10.4	73	10
0	180	0	0	0	0

predicted. The beam peak scanned the elevation plane for a fixed azimuth angle of 0^o, or $\phi = 0^o$. All the elevation cuts containing the beam peak (taken at $\phi = 0^o$) are plotted in Fig. 3.13. Similarly to the mode I scan, the maximum peak directivity is achieved when the beam is in the broadside direction for $\psi_1 = 90^o$ and $\psi_2 = -90^o$. The peak directivity decreases as the beam is scanned in the elevation plane away from the broadside. Unlike the mode I scan where the highest peak directivity was 20 dB in the broadside direction, the mode II scan yields the highest peak directivity of 21 dB in the same direction. The orientation of the LGDs along with the angular position of the beam peaks estimated using equations (1) – (5) and predicted by the numerical simulations are given in Table 3.6.

3.6.3 Mode III

To scan an azimuth plane for a fixed elevation angle, the two LGDs are synchronously rotated around the antenna axis. The synchronous rotation of the two LGDs moves the beam in the azimuth plane without affecting the beam position in the elevation plane. This scanning mode

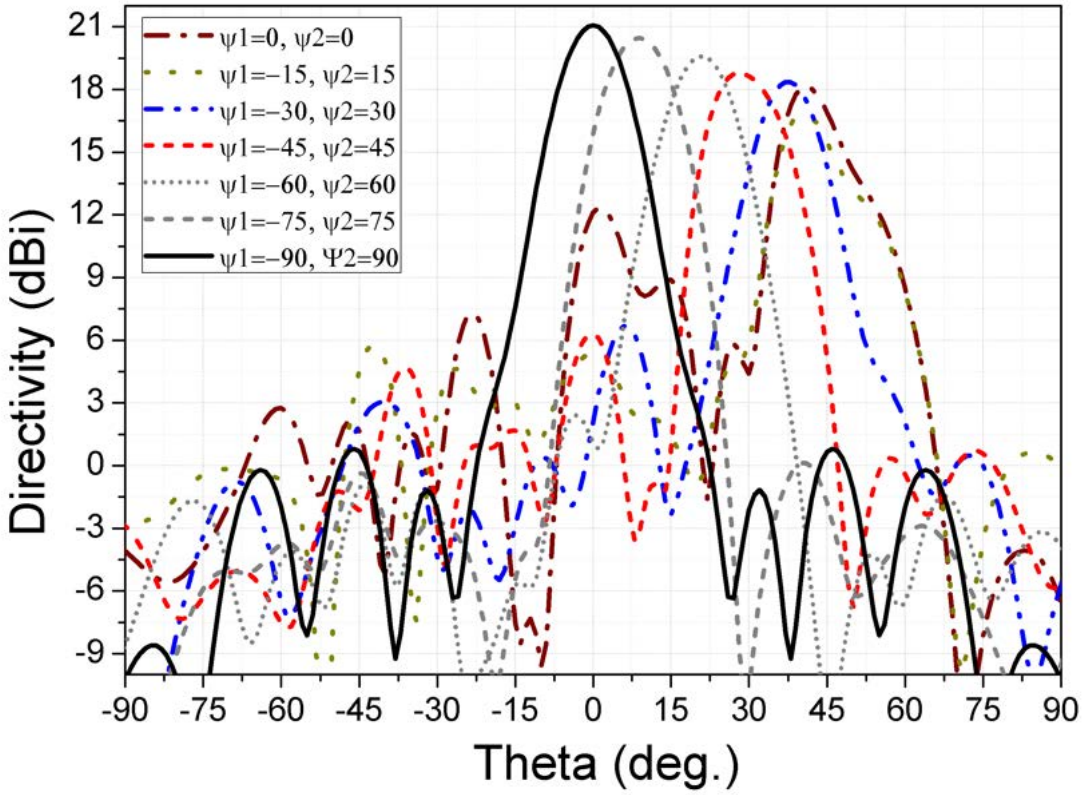

Figure 3.13: Elevation cuts taken at $\phi = 0^o$ for the different orientation angles of LGD I and LGD II.

can be applied to any orientation of LGD I and LGD II or initial values of ψ_1 and ψ_2. The mode III scanning is verified for the case when $\psi_1 = 45^o$ and $\psi_2 = -45^o$ and the beam peak is estimated at $\phi = 0^o$ and $\theta = 28^o$.

In the selected configuration, the inter-angular spacing between two LGDs is 90^o and will remain fixed throughout the scan. Two LGDs are then rotated anticlockwise synchronously with a step of 45^o and the far-field patterns were numerically computed. For each combination of ψ_1 and ψ_2, elevation cuts taken at the azimuth angles containing beam peaks are plotted in Fig. 3.14. It can be seen from the figure that the elevation angle of the beam peak is fixed to $\sim 28^o$, or $\theta = 28^o$, while the azimuth angle (or ϕ), indicated in the legend, changes from 0^o to 315^o with a

Table 3.6: Angular position of beam peak predicted by numerical simulations.

Orientation of LGDs		Estimated		Predicted	
ψ_1(deg.)	ψ_2(deg.)	ϕ(deg.)	θ(deg.)	ϕ(deg.)	θ(deg.)
0	0	0	40	0	41.5
-15	15	0	38.6	0	40.7
-30	30	0	34.6	0	38
-45	45	0	28.3	0	28
-60	60	0	20	0	21
-75	75	0	10.4	0	9
-90	90	0	0	0	0

step of 45°. The beam peak is consistent with a slight variation in SLL for some combinations of ψ_1 and ψ_2. The angular position of the beam peaks predicted by numerical simulation and estimated by analytical equations are compared in Table 3.7. For azimuth scanning at any other elevation angle smaller than θ_{max}, the desired elevation angle can first be achieved using either model I or mode II scan.

Using combinations of mode I and mode III or mode II and mode III, the beam can be scanned to any azimuth angle between 0° and 360° for any elevation angle smaller than $\theta_{max} = 41.2°$. This forms a conical scannable region having an apex angle of 82.4°, or $2\theta_{max}$. As observed from the numerically predicted results, during the beam scanning, the peak directivity drops, the beam widens, and the side-lobes appear. However, the peak directivity stays within the 3 dB limit of the highest directivity – a number used as a reference in beam-scanning antenna applications. The proposed solution of beam scanning is extremely thin and planar. The total height of the system is $\sim$ 60 mm, which is approximately $2.2\lambda_0$. Additionally, the solution is totally passive and could be developed into an extremely efficient antenna solution using low-loss dielectric materials. Typically, dielectric losses increase with frequency and can be one limiting

Table 3.7: Angular position of the beam peak when LGD I and LGD II are rotated synchronously.

Orientation of LGDs		Estimated		Predicted	
ψ_1(deg.)	ψ_2(deg.)	ϕ(deg.)	θ(deg.)	ϕ(deg.)	θ(deg.)
-45	45	0	28.3	0.6	28.9
0	90	45	28.3	45.9	29.3
45	135	90	28.3	90.9	29.8
90	180	135	28.3	134	28.9
135	225	180	28.3	179	28.2
180	270	225	28.3	226.9	29.9
225	315	270	28.3	271.5	30.9
270	360	315	28.3	314.9	29.9

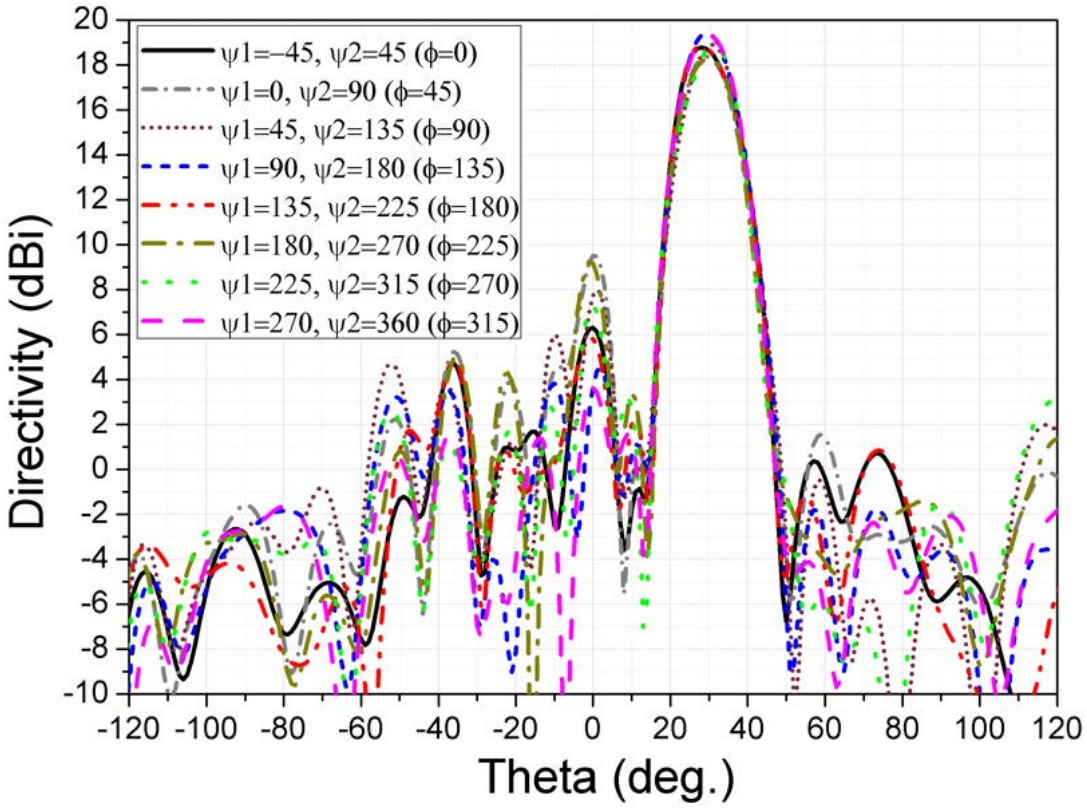

Figure 3.14: Elevation cut taken at different azimuth angles containing beam peak. For each pattern cut, the azimuth angle (ϕ) and the orientation of the LGD I and LGD II are given in the legend.

factor for this antennas system designed to operate at millimeter wave frequencies.

It is to be mentioned here that the proposed beam-scanning technique using LGDs in the near-field region is not dependent on the type of base antenna. An RCA has only been used because of its planar profile, smaller aperture, and our extensive experience of working with RCAs. Any type of antenna with an aperture of more than few wavelengths such as a radial line slot array (RLSA) or even an array of patches can be used as EM illuminators. These illuminators do not need a reflecting superstrate and may also not require the RGD, resulting in a much simpler antenna structure in terms of stacked layers. A detailed study on the comparison of base

illuminators is beyond the scope of this work, which is aimed at introducing the beam-scanning technique using rotation of near-field LGDs.

Lack of a prototype and measurement results at this stage should not be considered as a limitation of the proposed beam-scanning antenna. As an extension, two separate research streams are being investigated to develop a prototype. One of the research directions is creating a dielectric material having customized permittivity values by volumetric combination of a high-permittivity dielectric such as Strontium Titanate ($SrTiO_3$) and low-permittivity dielectrics such as polydimethylsiloxane (PDMS) [115]. The two dielectrics are mixed at a certain volume ratio before being cured at a proper temperature. The permittivity value is verified with a dielectric measurement kit. In the second research direction, additive manufacturing or 3D printing is explored to develop a double layer of meta-atoms having effective permittivity required for the RGD and LGDs [116]. Further developments on the prototyping will be reported in subsequent publications on the subject.

3.7 Rotation Mechanism

There are several possibilities for rotating the mechanical system for the pair of LGDs. One method, implemented in a separate project, uses magnetic and direct gears. A cross-sectional view of the mechanical system is shown in Fig. 3.15. The mechanism is based on two 3D-printed cylindrical rings, a rigid conduit, and two gears: a magnetic gear for rotating LGD I and a direct gear for rotating LGD II.

At the bottom, the conduit is attached to the ground plane that carries the RF cable and cables for the two motors. The first cylindrical ring, which is hollow inside, encapsulates the RCA and the RGD. The ring has an opening on the top side where the LGD I is fixed. The bottom of the ring is attached to the conduit via a cylindrical bearing. Additionally, a magnetic gear is attached at the bottom inside face of the ring.

The second cylindrical ring wraps around the first ring; it also has an opening on the top face for LGD II and at the bottom face attached to the conduit via a cylindrical bearing. The bottom

face of the second ring has gear teeth, which are directly connected with the rotor of a stepper motor. The rotor of the other motor has a magnetic gear, which rotates the first ring and hence LGD I with coupled magnetic field.

This first prototype of the mechanical system is tall and heavy because of the thick magnetic gears. The maximum height of that mechanical system is 13.5 cm, which is $5\lambda_0$ at the operating frequency. The total weight of that mechanical system is 3 kg, mainly due to the weight of magnetic gears. Two commercially available SS250 stepping motors are used, each capable of supporting the required inertia while maintaining a speed of 100 rotations per minute. The direct gear used with the second stepper motor has teeth ratio of 16:128, where 128 teeth are in the driven gear side attached to the outer ring for LGD II and 16 teeth on the driver gear side attached to the stepper motor. The maximum speed of the LGD I is restricted to 12 rotations per minute. The total cost of the mechanical system including 3D printing of various parts and components is approximately 450 USD. The maximum height of proposed antenna system even with the first prototype of rotating mechanical structure is $4.7\lambda_0$, which is still two wavelengths shorter than the VICTS technology based beam-steering antenna [104].

It is worth emphasizing here that there is no blockage caused by any element of the rotating structure. The cylindrical walls are made of a low-permittivity dielectric material and hence have little effect on the propagating field. Additionally, the ring walls are at the outer periphery of the LGDs, where EM field strength is very small, which has maximum intensity at the center of the aperture. All of the other components including motors and magnetic gears are below the metallic ground plane. There is no interference caused by these components to the field propagation, which is naturally shielded by the ground plane.

3.8 Conclusion

The paper presented a low-profile, planar, and all-dielectric beam-scanning antenna system. The antenna system comprises a resonant-cavity antenna (RCA) and three graded-dielectric plates: one radially graded and two linearly graded. The radially graded dielectric (RGD) is stationary

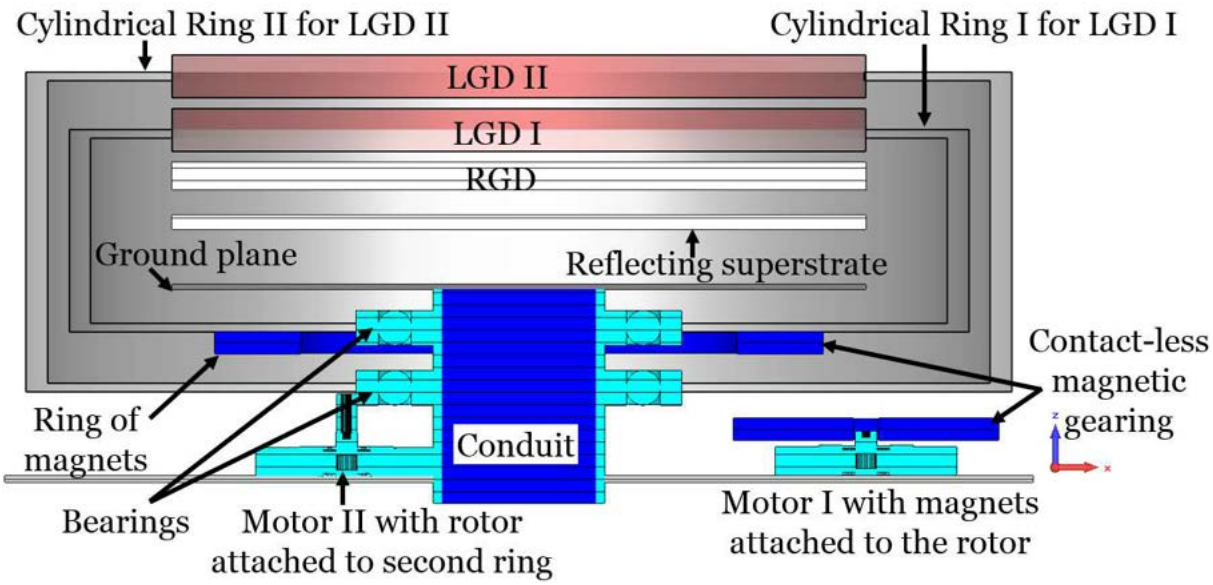

Figure 3.15: Cross-sectional view of one rotation mechanism using magnetic and direct gearing system. Some of the supports used for suspending the reflecting superstructure are not shown in the figure.

while the two linearly graded dielectric (LGD) plates are rotated around the antenna axis. The far-field patterns are predicted by numerical simulations for different beam scanning modes. Numerical results predicts that antenna system has maximum peak directivity and gain of 21 dBi and 20.2 dB, respectively. The aperture efficiency is around 23%. Using three different beam-scanning configurations, it is estimated that the beam can be scanned within a large conical region with an apex angle of 82.2^{o}.

The total height of the antenna system is $2.2\lambda_0$, which is significantly less than mechanically scanned reflector dishes. Due to the low and planar profile of the antenna system, it can be used to develop Ka and Ku band beam-scanning antennas for ground and mobile terminals to communicate with upcoming LEO and MEO satellites. Two separate approaches are being investigated to synthesize the materials required for prototyping. The first is based on a volumetric combinations of a low-permittivity dielectric polydimethylsiloxane (PDMS) and a high-permittivity dielectric Strontium Titanate ($SrTiO_3$) to achieve an intermediate permittivity value. The second uses additive manufacturing to develop meta-atoms having the desired effective permittivity

values.

CHAPTER 4

Printed Wideband Metasurface for Compact High-gain Resonant Cavity Antennas

4.1 Abstract

This paper presents a design methodology for a compact, low-cost Partially Reflecting Surface (PRS) for a wideband high-gain Resonant Cavity Antenna (RCA) which requires only a single commercial dielectric slab. The PRS has one non-uniform double-sided printed dielectric, which exhibits a negative transverse-reflection magnitude gradient and at the same time a progressive reflection phase gradient over frequency. In addition, a partially shielded cavity is proposed as a method to optimize the directivity bandwidth and the peak directivity of RCAs. A prototype of the PRS was fabricated and tested with a partially shielded cavity, showing good agreement

Published as: Ali Lalbakhsh, Muhammad U. Afzal, Karu P. Esselle, Stepanie L. Smith, Basit A. Zeb, "Single-dielectric Wideband Partially Reflecting Surface with Variable Reflection Components for Realization of a Compact High-gain Resonant Cavity Antenna," *IEEE Transactions on Antennas and Propagation*, vol. 67, no. 3, pp. 1916–1921, Jan. 2019.

between the predicted and measured results. The measured peak directivity of the antenna is 16.2 dBi at 11.4 GHz with a 3-dB bandwidth of 22%. The measured peak gain and 3-dB gain bandwidth are 15.75 dBi and 21.5%, respectively. The PRS has a radius of 29.25 mm ($1.1\lambda_0$) with a thickness of 1.52 mm ($0.12\lambda_g$), and the overall height of the antenna is $0.6\lambda_0$, where λ_0 and λ_g are the free-space and guided wavelengths at the center frequency of 11.4 GHz.

4.2 Introduction

Resonant Cavity Antennas (RCAs), also known as electromagnetic band gap resonator antennas, PRS antennas, 2-D leaky-wave antennas and Fabry-perot cavity antennas, have attracted a lot of interest from the antenna community over the past decade, due to their planar configuration, highly directive radiation patterns and simple feed mechanism [75, 117–121].

These desirable characteristics have made this type of antenna a good replacement for arrays with complex feed networks and bulky reflector antennas. RCAs generally consist of a Partially Reflecting Surface (PRS) placed above a ground plane containing a small feed antenna to make a resonant cavity. Numerous reflections inside the cavity spread the electromagnetic field within the cavity, leading to boresight radiation. The PRS is generally made of 1-D periodic layers of dielectric [122–124], one or multiple 2-D Frequency Selective Surfaces (FSSs) [25, 28, 125] and [7–12, 126, 127], or 3-D EBG structures [128]. The application of such passive periodic structures is not limited to RCAs and they are extensively used for other antenna designs and beamsteering purposes [129, 130].

Early high-gain RCAs had a small bandwidth of less than 3% [122, 128, 131] and, therefore, several attempts have been made to increase the bandwidth of this class of antennas [6–12, 126, 127, 132, 133]. One approach is using several layers of the same or different dielectrics as a superstructure [132,133]. The key idea of using a multi-layer PRS is to create multiple resonances which can be controlled and tuned by adjusting the spacing between the dielectric layers and/or using dielectric slabs with different permittivities.

Such techniques, on the downside, increase the antenna volume and upset the mechanical

stability of the antenna. To address these deficiencies, a class of all-dielectric PRS composed of different concentric dielectric materials has recently been introduced [6, 117]. However, the manufacturing process and mass-production capability have not been addressed, as such heavy composite-based structures require several thick dielectric layers and various bonding techniques. Additionally, achieving a good impedance matching is difficult, due to the losses associated with the large volume of the dielectric employed in the PRS. Consequently, the 10-dB $|S11|$ bandwidth is considerably smaller than the radiation bandwidth, reducing the effective bandwidth of the RCA [6]. In a different approach, Frequency Selective Surfaces (FSSs) have been proposed as a class of wideband PRS [7–12, 134, 135]. It should be mentioned that FSSs can also be used for mutual coupling reduction [136, 137]. Several PRSs composed of multiple printed dielectric substrates have been designed to produce a progressive reflection phase gradient over a finite band, which creates a broadband response [7–10]. As an example, the positive reflection phase gradient is around 30% of the overall 3-dB directivity bandwidth achieved using a dual-layer FSS structure [10]. In an attempt to minimize the number of FSSs in the superstructure, single-dielectric FSSs have been designed for high-gain RCAs at the price of both large lateral areas and limited bandwidths [11, 135].

Reviewing the literature reveals that the design of a PRS having all the critical characteristics, such as a single commercial dielectric layer, compactness, stable $|S11|$ bandwidth, high gain and wideband response, is a real challenge in relation to RCAs. In this paper we deal with this challenge by introducing a non-uniform thin printed PRS which not only provides a positive reflection phase gradient, but also produces a negative transverse-reflection magnitude gradient. The first phenomenon has already been realized using either multiple printed dielectric surfaces or a large single FSS, while our PRS is made of a compact single dielectric. The second phenomenon was realized in [6] by bonding thick and heavy dielectric materials, whereas our proposed PRS is thin, light and low cost.

The rest of the paper is organized as follows: the design methodology of the proposed PRS is explained in Section II, where a PRS composed of resonating elements is designed at 11 GHz to meet the two aforementioned conditions. This satisfies the cavity resonance condition over

a wider range of frequencies without sacrificing peak gain or compactness. A partial shielding technique is then investigated, showing 0.6 dB and 4% improvements in the peak directivity and 3-dB directivity bandwidth, respectively. Section III discusses the measurement results of the antenna.

4.3 Partially reflecting Surface Design

4.3.1 Resonance Condition of the Cavity

According to the conventional PRS design procedure, the thickness of an unprinted slab is a quarter wavelength, which results in a small defect-mode bandwidth, leading to a limited gain bandwidth [12]. Multi-layer superstrates have been used to create multiple resonant inclusions to produce a wider transmission band [132]. To achieve the above characteristic without sacrificing the compactness and low fabrication cost, printed resonating elements can be made to resonate at two adjacent frequencies, to produce a wide transmission band.

However, this is not a sufficient condition to ensure a wideband performance of RCAs [11]. Based on the analysis of ray tracing [9, 46], the resonance condition for maximum boresight radiation at the operating frequency is

$$\phi_{sup} - \pi - \frac{4\pi}{\lambda}h = 2N\pi \tag{4.1}$$

where N is an integer, h is the cavity height, λ is the free-space wavelength at the operating frequency, and ϕ_{sup} is the reflection phase of the superstructure for normal incidence.

In order to have a large operational bandwidth, the above equation should ideally remain valid over the bandwidth. To do so, the reflection phase of the PRS needs to increase with frequency, which is not possible with the conventional PRSs.

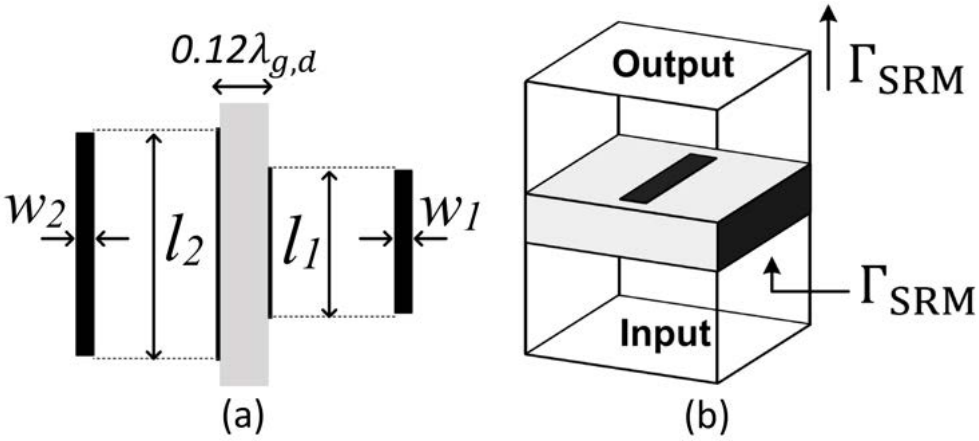

Figure 4.1: (a) A unit cell of the proposed PRS. (b) Superstructure Reflection Model (SRM) required to characterize the unit cell.

4.3.2 Positive Reflection Phase Gradient

It is well-proven that components behave differently around their resonant frequencies. Owing to this fact a positive reflection phase gradient can be achieved by taking advantage of the resonance [11]. Therefore, two periodic arrays of resonating parallel strips, each printed on the opposite sides of a dielectric slab (Rogers TMM 4), were designed at 11 GHz for our PRS, as shown in Fig. 4.1(a).

The dimensions of the two resonator strips are $l_1 \times w_1$ and $l_2 \times w_2$, the thickness of the dielectric is 1.52 mm, and the square unit cell length is 4.5 mm ($0.165\lambda_{0,d}$), where $\lambda_{0,d}$ is the free-space wavelength at the design frequency (11 GHz). It should be noted that periodic boundary conditions, assuming infinite repetition of unit cells in transverse directions, are used in the PRS design to significantly reduce the computation time [7–9].

To determine the initial size of the resonators, identical conductive strips are initially used on both sides of the dielectric slab, resulting in a single strong resonance, dominantly controlled by the length of the conductors. The input impedance of the unit cell for a constant value of w and varying l is shown in Fig. 4.2. As can be seen, zero reactance shifts from 10 GHz to 14 GHz with slight changes in l. This verifies that the resonance can be reasonably controlled by the

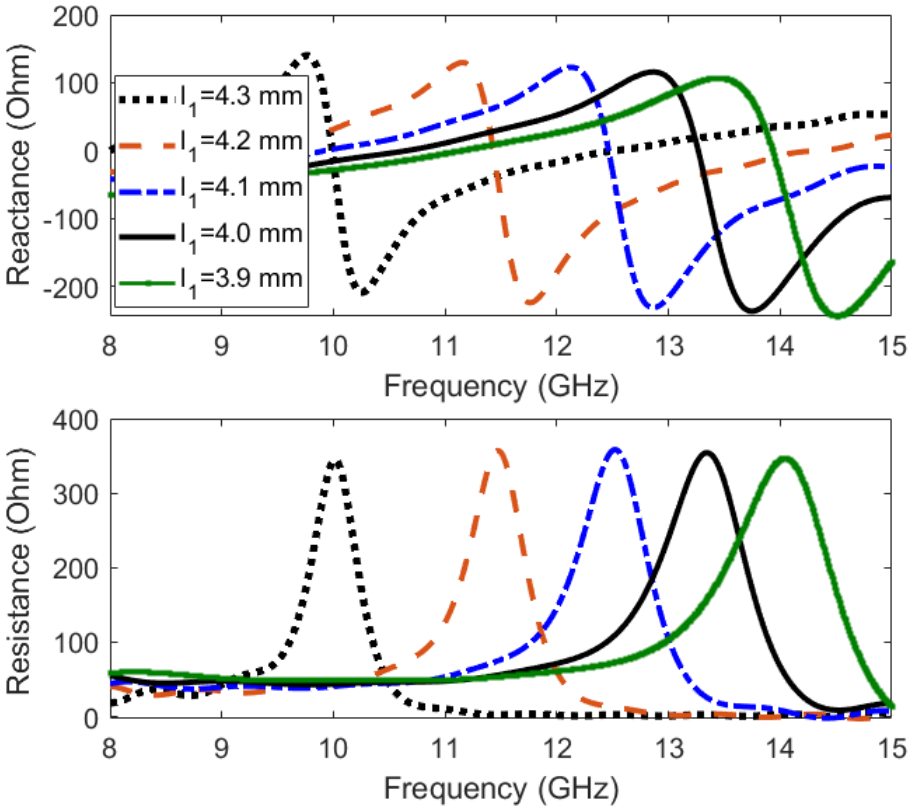

Figure 4.2: Impedance of the proposed unit cell with varying identical strip lengths (l) and a constant width $w = 0.4\ mm$.

length of the conductive elements. Having the initial dimensions of the resonating strips, as well as the required reflection characteristics, the resonance can be tuned to acquire the phase and magnitude reflection requirements. Therefore, the next step is to define the magnitude reflection conditions which need to be satisfied by the proposed unit cell.

4.3.3 Negative Transverse-Reflection Magnitude Gradient

According to our near-field investigation into a conventional RCA composed of a PRS with a permittivity of 4.5, shown in Fig. 4.3, the magnitude of the electric field decreases towards the edges of the cavity, which results in poor aperture efficiency and sub-optimal peak gain. This led to the hypothesis that an unconventional PRS with nonuniform magnitude reflection characteristics can be developed to address this deficiency. Therefore, our PRS is divided into

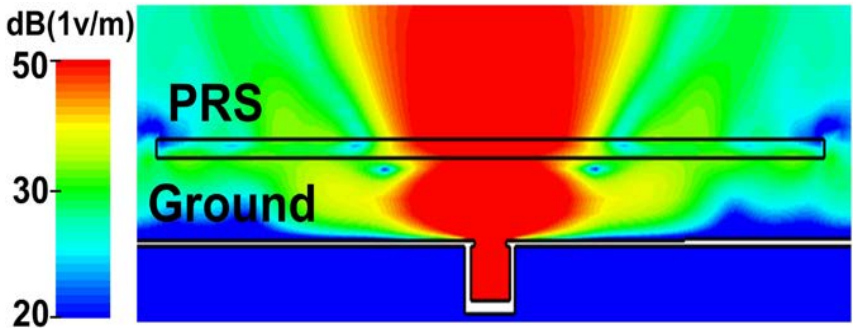

Figure 4.3: Electric field distribution ($|E_y|$) in the cavity of the conventional RCA at 11.4 GHz. The PRS is an unprinted Rogers TMM4 with a thickness and area of $\lambda_g/4$ and $6\lambda_0 \times 6\lambda_0$, respectively. λ_g and λ_0 are the guided and the free-space wavelengths at the center frequency of 11.4 GHz, respectively.

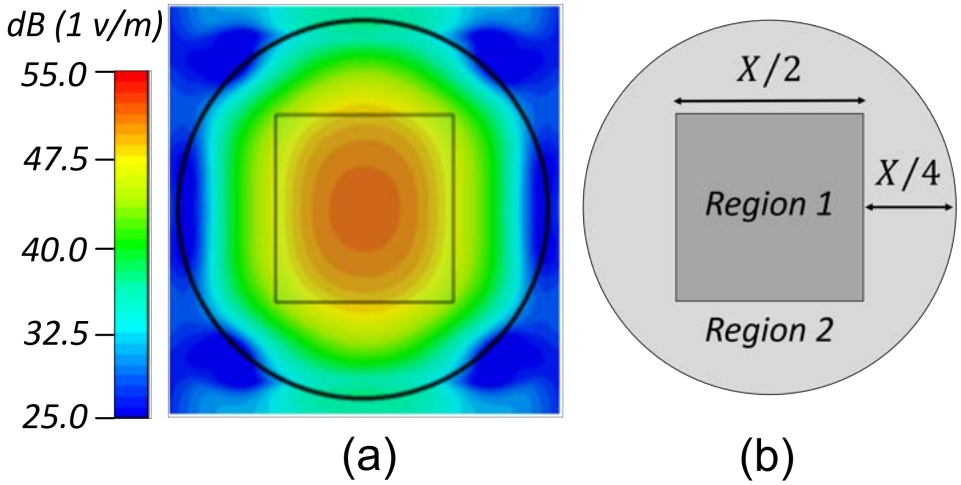

Figure 4.4: RMS values of the dominant electric field (Y component) on the aperture of an RCA at 11 GHz. The PRS is an all-dielectric substrate with a permittivity and thickness of 4.5 and $0.12\lambda_{g,d}$, where $\lambda_{g,d}$ is the guided wavelength at 11 GHz. (b) Two regions of our unconventional non-uniform PRS with a length of $X = 2.2\lambda_{0,d}$, where $\lambda_{0,d}$ is the free-space wavelength at the design frequency of 11 GHz.

two regions; Region 1 which is a high-reflection zone and Region 2 representing a low-reflection area, as depicted in Fig. 4.4. These two zones are collaboratively responsible to equalize the magnitude of the electric field throughout the cavity, by enforcing more reflection in the central areas and less in the outer regions. The size of the regions is chosen based on the magnitude of the electric field on the aperture. The RMS values of the electric field are visualized in the reactive near-field region in a reference plane at a distance of $0.03\lambda_{0,d}$ (1 mm) from the PRS, where $\lambda_{0,d}$ is the free-space wavelength at the design frequency of 11 GHz. The size of Region 1 is selected to moderate the electric field values in the areas with at least 75% of the peak RMS. As shown in Fig. 4.4(a), the 75% RMS cut-off of Region 1 is 47.5 V/m.

In order to choose the reflection magnitude values in the two regions of the PRS, more investigation into a heavily truncated PRS and the relationship between the reflection coefficients and the radiation patterns of a miniaturized RCA is required. To do this, the same antenna in Fig. 4.4 was simulated with different reflection magnitudes of the same-size PRS. As shown in Fig. 4.5, there is a trade-off between the peak directivity and the 3-dB directivity bandwidth for various reflection magnitudes of the truncated PRS. According to a design requirement, at the operating frequency, a suitable reflection magnitude can be adopted for a PRS. In the proposed design, the desired least directivity bandwidth and the least peak directivity are 20% and 15 dBi, respectively. According to Fig. 4.5, for the desired directivity bandwidth, the reflection magnitude of the PRS needs to be smaller than -7 dB. On the other hand, the reflection magnitude of the PRS must be greater than -3 dB in order to achieve a peak directivity of more than 15 dBi. The two desired design parameters have conflicting requirements on the reflection magnitude. Therefore, instead of satisfying one condition at the cost of the other, both are marginally reduced by choosing a PRS having a reflection magnitude between -3 dB and -7 dB. For Region 1, the PRS used has a reflection coefficient of -4 dB at the operating frequency (11 GHz). It should be noted that the choice of -4 dB within -3 dB to -7 dB is arbitrary and any other realizable value that can also satisfy the condition of a positive phase gradient for the PRS design can be used. For Region 2, apart from all the above considerations, an additional condition imposed is to have a reflection magnitude smaller than that of Region 1. These criteria

need to be satisfied at the operating frequency and preferably within a finite band around the operating frequency. In the proposed design, the reflection magnitude of the PRS used in Region 2 is -5 dB. As explained above, other realizable choice values can be possible if the positive phase gradient is achieved in the PRS design.

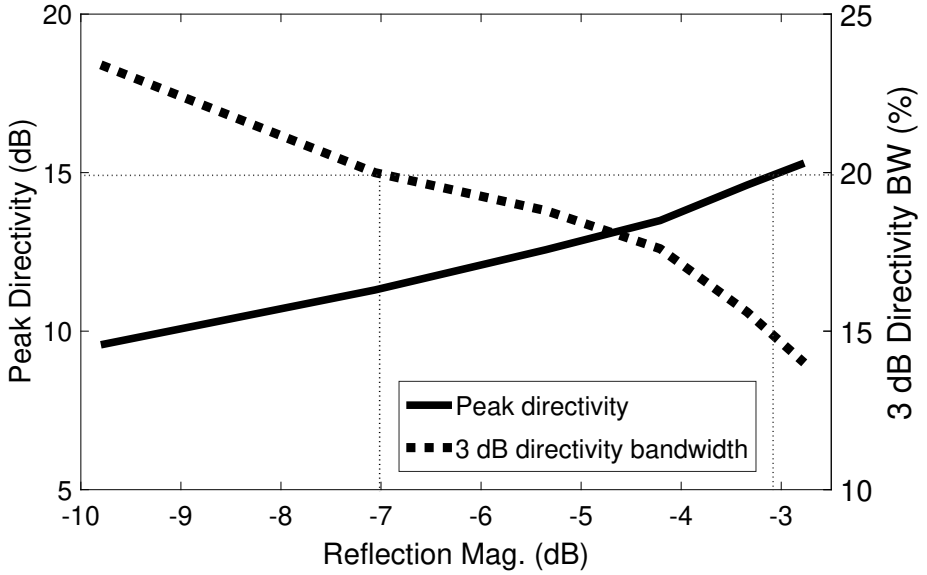

Figure 4.5: Peak directivity and 3 dB directivity bandwidth versus reflection magnitude in a heavily truncated PRS. The PRS is an all-dielectric substrate with a thickness of $0.12\lambda_{g,d}$, where $\lambda_{g,d}$ is the guided wavelength at 11 GHz.

For a higher minimum reflection magnitude in Region 1, a weaker resonance is created using two strips which are very different in length. In contrast, a stronger resonance is realized using identical strips; however the lengths of the two strips in Region 2 are not identical and are chosen to be close to -5 dB. To do this, a fine parametric sweep of the conductive lengths was performed using the initial geometrical values to simultaneously satisfy both phase and magnitude gradient requirements. The dimensions of the conductive strips are given in Table I.

The computed reflection magnitude and phase of the unit cells in both zones, shown in Fig. 4.6, verify the realization of the predefined reflection requirements. Region 1, the central area of the PRS, provides a higher reflection magnitude (around -4 dB), while Region 2, the outer area of the PRS, is less reflective (-5 dB) at the design frequency (11 GHz); hence, a

Table 4.1: Dimensions of the strip resonators in different regions

Dimension (mm)	l_1	w_1	l_2	w_2
Region 1	4.4	0.4	3.3	0.4
Region 2	4.3	0.4	4.1	0.4

negative transverse-reflection magnitude gradient has been achieved. Both regions also exhibit a positive reflection phase gradient versus frequency in a finite band. Fig. 4.6 compares the reflection components of the unit cells designed at 11 GHz with that of a conventional PRS with $\lambda_g/4$ thickness. It is observed that the reflection phase gradient is not always positive throughout the band, however it does not violate the PRS wideband performance, as reported in [7, 10, 132].

To optimize the peak directivity and directivity bandwidth without enlarging the antenna, a partial shield (Fig. 4.7(c)) is proposed. The effects of the surrounding metallic wall on the directivity of the RCA are depicted in Fig. 4.8. The optimal height of the shield is $0.022\lambda_0$ (6 mm), resulting in 0.6 dB and 4% improvements in peak directivity and 3-dB bandwidth, respectively. It should be mentioned that higher gain can be achieve using this technique at a price of larger aperture size.

4.4 Results

The layout of the printed PRS along with a photo of the fabricated antenna prototype are shown in Fig. 4.7. The RCA was simulated using the time-domain solver of CST Microwave Studio to verify the design. The proposed PRS was placed at a distance of $0.55\lambda_0$ from the ground plane, where λ_0 is the free-space wavelength at the center frequency (11.4 GHz). It should be noted that the analytically calculated cavity height is $0.50\lambda_0$ which was slightly tuned to attain the resonance at the operating frequency.

The PRS was made of Rogers TMM4 slab with a diameter and thickness of 58.5 mm ($2.2\lambda_0$)

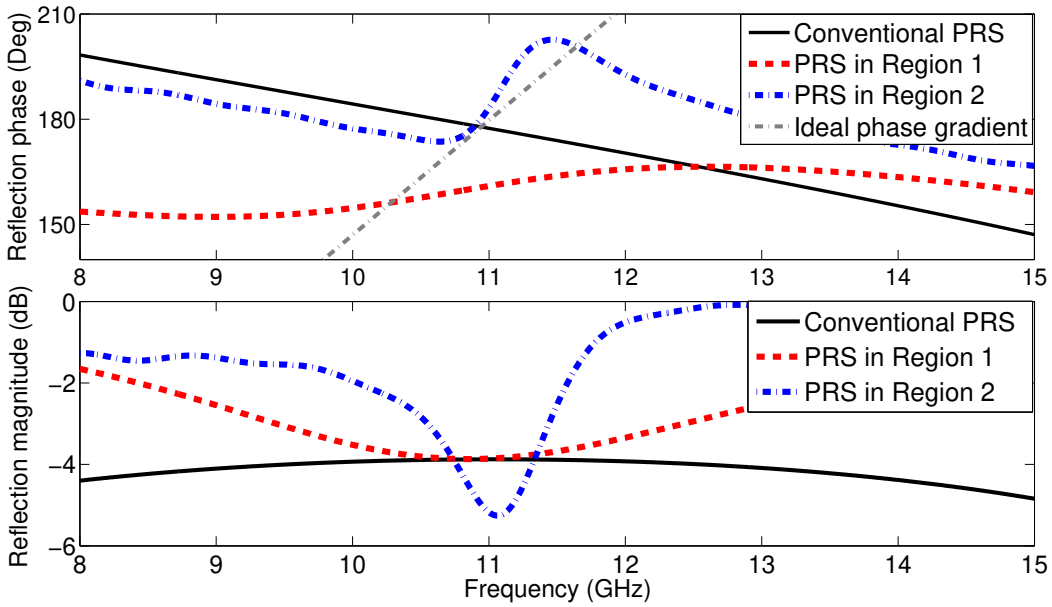

Figure 4.6: Reflection phase and magnitude of two different unit cells designed for Region 1 and Region 2 of the PRS are compared with that of a conventional PRS.

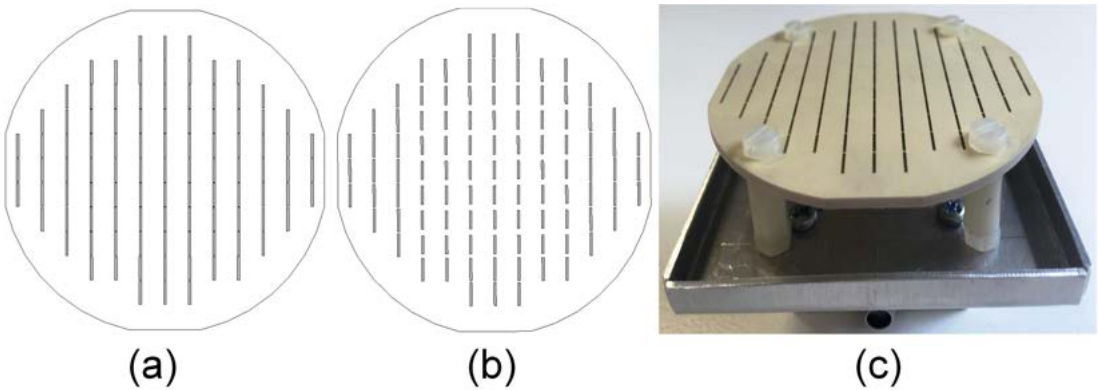

Figure 4.7: Proposed PRS. (a) Strip resonators on the upper surface. (b) Strip resonators on the lower surface. (c) A photo of the fabricated RCA with partially shielded cavity.

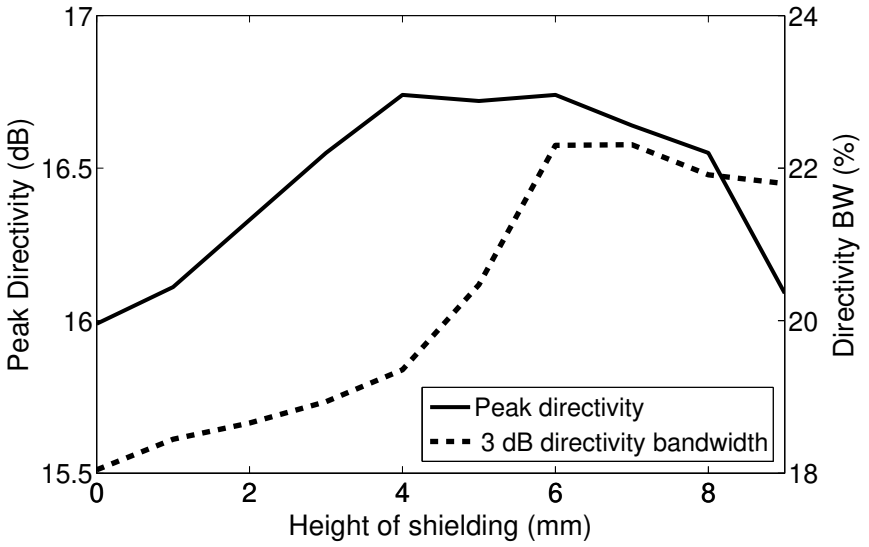

Figure 4.8: The effects of partial shielding on the directivity and bandwidth of the RCA.

and 1.52 mm ($0.12\lambda_g$), respectively. The feed antenna is a waveguide-fed slot placed in the center of the ground plane with dimensions of 13 $mm \times 6$ mm ($0.49\lambda_0 \times 0.23\lambda_0$). Near-field results, shown in Fig. 4.9(a), verify that the magnitude of the electric field ($|E_y|$) is stronger in a larger area in the cavity, due to the application of varying reflection magnitudes. The addition of the shield makes the field even stronger throughout the cavity, as shown in Fig. 4.9(b).

This phenomenon has increased the calculated aperture efficiency, reaching 71% and 83% for the case of unshielded and partially shielded RCAs, respectively.

4.4.1 Measurement Results

The input reflection coefficient was measured using an Agilent PNA-X N5242A vector network analyzer. As shown in Fig. 4.10, the measured 10-dB $|S11|$ bandwidth is 38%, from 10.1 to 14.9 GHz.

Table 4.2: Comparison with a few recently proposed PRSs

Reference number	No. of Spacings	No. of dielectrics	Area (λ_0^2)	Thickness (λ_g)	Mass (gr)	Gain (dB)	BW (%)	Structure
[11]	0	1	20.2	0.1	42	16.2	12.6	Single FSS
[6]	0	3	3.3	1.3	24	16.4	37	Composite with bonding
[125]	0	1	13	0.48	–	16.5	2.4	Single FSS
[126]	2	2	6.0	–	–	15.5	8.26	Multiple FSS
[134]	2	3	14.3	–	39	20	15	Multiple FSS
[10]	1	2	10.8	–	–	16.8	12.5	Multiple FSS
[135]	0	1	10.6	0.08	–	19.67 (dir.)	7	Single FSS
This work (Meas.)	0	1	3.8	0.12	9	15.75	21.5	Single FSS
This work (Sim.)	0	1	3.8	0.12	9	16.1	22.8	
This work (Conv. ground)	0	1	3.8	0.12	9	15.5	18.7	

Note: f_0 is the center frequency of the effective bandwidth of the antenna. Both λ_0 and λ_g are defined at the center frequency of the effective bandwidth (f_0). BW is the effective 3-dB gain bandwidth (input reflection coefficient is less than -10 dB throughout the bandwidth).

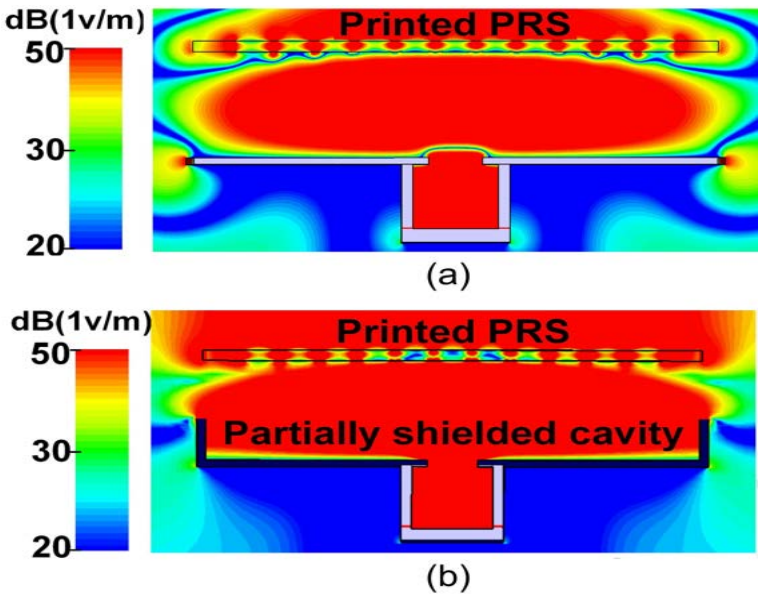

Figure 4.9: Electric field ($|E_y|$) distribution in the cavity of the new RCA at the center frequency of 11.4 GHz with (a) unshielded cavity and (b) partially shielded cavity with an optimized height of 6 mm.

The prototype RCA exhibits a large 3-dB directivity bandwidth from 10.23−12.76 GHz, equal to 22%, with a VSWR better than 1.5 throughout this bandwidth. A peak directivity of 16.2 dBi occurs at 11.3 GHz, as shown in Fig. 4.11. Its 3-dB gain bandwidth extends from 10.18 to 12.63 GHz, i.e. 21.5%. A good agreement between predicted and measured results is also observed. The radiation patterns, measured in an NSI spherical near-field range at four frequencies within the directivity bandwidth, are shown in Fig. 4.12.

Although the PRS is symmetric, the overall patterns from the antenna are not identical in the two principal planes, as shown in Fig. 4.12. This is, due to the unsymmetrical field radiated by the primary feed inside the cavity. It should be noted that the increase in the SLLs around the edges of the operating band is contributed by the high SLLs of the primary feed. From a physical point of view, the PRS is very thin (1.52 mm), light (9 gr), compact and low cost, which can make wideband array RCAs an economically feasible option. A comparison with some published wideband PRSs is made in Table II, highlighting the functionality of the proposed

structure. Although the composite antenna in [6] exhibits the largest bandwidth, the fabrication cost is considerably higher, due to employing multiple thick substrates and the high volume of dielectric wastage in the fabrication process.

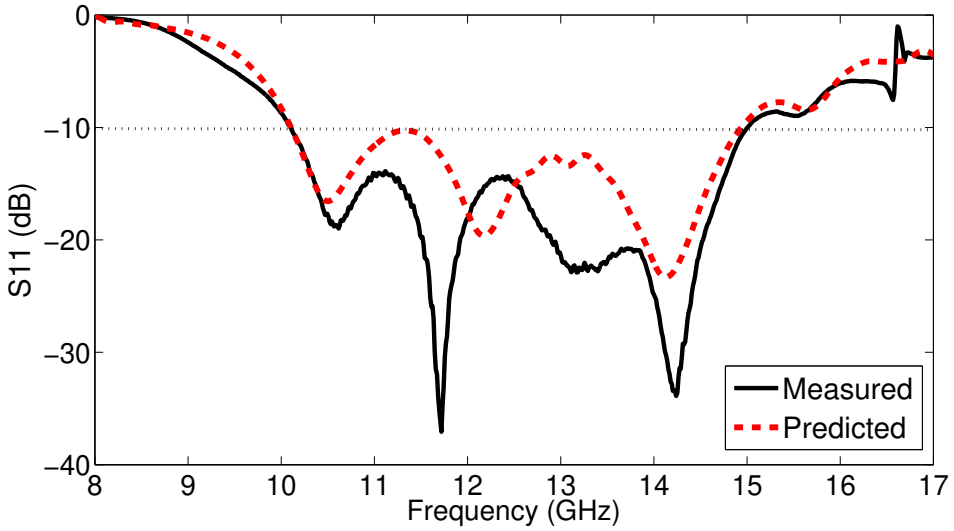

Figure 4.10: Input reflection coefficient of the antenna.

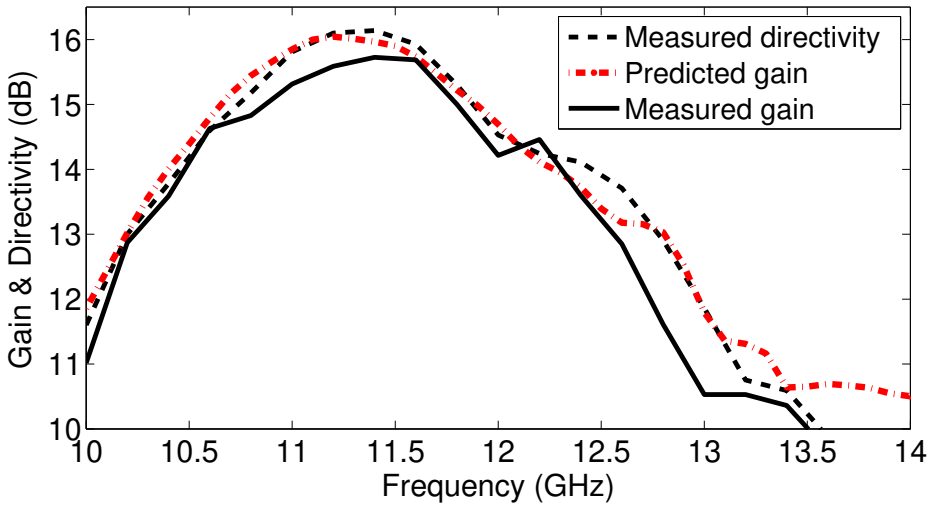

Figure 4.11: Gain and directivity of the new RCA.

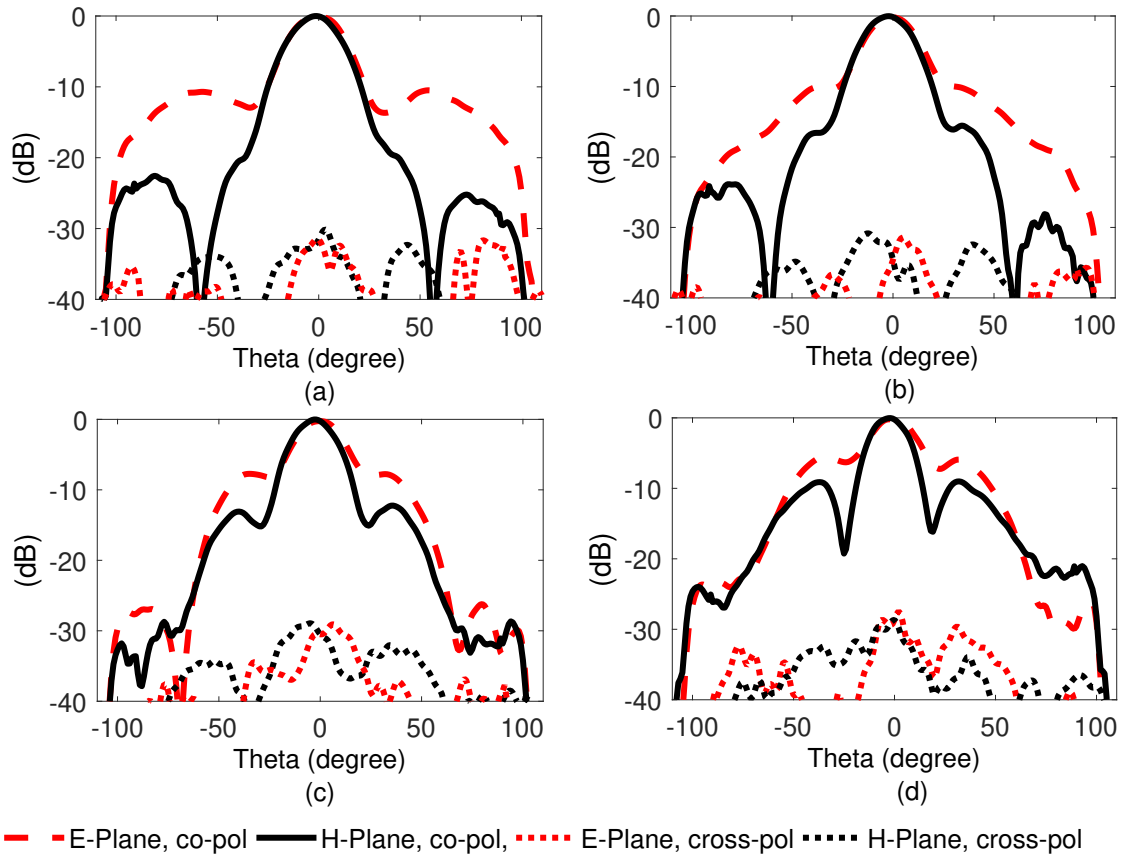

Figure 4.12: Normalized radiation patterns of the RCA at four equally spaced frequencies as measured in NSI-700S-50 spherical near-field chamber. (a) 10.8 GHz. (b) 11.2 GHz. (c) 11.6 GHz. (d) 12 GHz.

4.5 Conclusion

A single-layer non-uniform Partially Reflecting Surface (PRS) is presented for realization of a high-gain wideband Resonant Cavity Antenna (RCA). The PRS is composed of arrays of resonating elements printed on both sides of a dielectric slab to create two phenomena which have never been used simultaneously. The non-uniform PRS exhibits different reflection magnitudes on the aperture, creating a negative transverse reflection magnitude gradient and at the same time a progressive reflection phase gradient over frequency. The combination of these two features results in a compact wideband PRS without sacrificing ease of fabrication and gain. In addition,

unlike the conventional RCAs, a partially shielded ground is proposed for further bandwidth and peak directivity improvement. The PRS has been fabricated and tested with this ground, producing a 16.2 dB peak directivity with 22% 3-dB directivity bandwidth. The measured peak gain is 15.75 dBi at 11.4 GHz with a 3-dB gain bandwidth of 21.5%. The PRS is compact, light, with a thickness and area of $0.12\lambda_g$ and $3.8\lambda_0^2$, respectively. Considering the radiation and physical characteristics of the proposed PRS, it is a good candidate for realization of wideband high-gain RCAs.

CHAPTER 5

Dielectric-Less Narrowband Phase-Correcting Metasurface

5.1 Abstract

This paper addresses a critical issue, which has been overlooked, in relation to the design of Phase Correcting Structures (PCSs) for Electromagnetic Bandgap (EBG) Resonator Antennas (ERAs). All previously proposed PCSs for ERAs are made either using several expensive Radio Frequency (RF) dielectric laminates, or thick and heavy dielectric materials, contributing to very high fabrication cost, posing an industrial impediment to the application of ERAs. This paper presents a new industrial-friendly generation of PCS, in which dielectrics, known as the main cause of cost and loss, are removed from the PCS configuration, introducing an All-Metallic PCS (AMPCS). Unlike existing PCSs, a hybrid topology of fully-metallic spatial phase shifters are developed for the AMPCS, resulting in an extremely lower prototyping cost as that of other state-of-the-art substrate-based PCSs. The APMCS was fabricated using laser technology and tested with an ERA to verify its predicted performance. Results show that the phase uniformity of the ERA aperture has been remarkably improved, resulting in 8.4 dB improvement in the

Published as: Ali Lalbakhsh, Muhammad U. Afzal, Karu P. Esselle, Stepanie L. Smith, "Low-Cost Non-Uniform Metallic Lattice for Rectifying Aperture Near-Field of Electromagnetic Bandgap Resonator Antennas," *IEEE Transactions on Antennas and Propagation, Vol. 68, 2020*

peak gain of the antenna and improved sidelobe levels (SLLs). The antenna system including APMCS has a peak gain of 19.42 dB with a 1-dB gain bandwidth of around 6%.

5.2 Introduction

In modern communication systems, directive antennas play an essential role in various applications such as satellite reception, point to point microwave links and back-haul networks. Reflector antennas are perhaps considered as one of the most conventional directive antennas with stable radiation patterns [138]; however their parabolic shapes along with their large sizes become problematic in some applications, such as communication on-the-move. Another category of the narrow-beam antennas are array antennas which occupy considerably less space; however a complex feed network is required which potentially increases the loss throughout the antenna system, and the fabrication cost. The third category of the directive antennas are cavity-based antennas, such as electromagnetic bandgap (EBG) Resonators Antennas (ERAs) also known as resonant cavity antennas and Febry-Perot resonator antennas which have the advantage of a single feed and a planar structure [7–9, 38, 39, 42, 53]. Despite the mentioned desired ERAs' characteristics, the near-field phase defect of this class of antenna was revealed in 2015 [49] and since then, several solutions have been proposed to tackle this deficiency in the hope of making ERAs a practical solution, when volumetric features along with electromagnetic characteristics are critical [21,22,25,43,49,50,60,75,139–149]. It is important to re-iterate that the lens theory cannot be applied on ERAs or any similar antennas to estimate their phase errors, as neither of the two essential conditions of single point source and reflection-free medium is satisfied in relation to ERAs, as explicitly discussed in [49]. As a result, the first generation of Phase Correcting Structure (PCS) for ERAs was proposed and tested successfully, suggesting significant improvement in the near-field phase uniformity, leading to highly directive radiation patterns with stable side lobe levels [49]. This very first class of PCS is composed of several dielectric heights to effectively manipulate the local aperture-phase values for phase-error minimization at the operating frequency [49, 56, 60, 139, 148]. However, the non-planar configuration, very high

fabrication cost, as well as undesirably heavy weight of such PCSs were a serious impediment to fully introduce the modified ERAs as a viable industrially justified solution. To mitigate some of these issues, semi-planar configurations were proposed, in which high-profile single-dielectric in the PCS configurations was replaced by composite-based dielectrics, leading to a lighter PCS with a smaller profile at the expense of more complex fabrication process. [50].

The second generation of PCS has been recently introduced [21,22,25], in which undesirably thick phase-correcting regions, in the first generation, have been replaced by completely planar surfaces. This class of PCSs is composed of multiple printed dielectric layers stacked together to impose localized time-delay throughout the aperture of the antenna. The second generation of PCSs have been successful in replicating almost the same electromagnetic performance as that of the first; nevertheless, the presence of multiple large dielectric substrates and the associated bonding techniques contribute to an expensive antenna system, limiting its applications in highly specialized practices.

Reviewing literature reveals that, while there has been a promising trajectory on evolution of PCSs for aperture antennas like ERAs, the critical aspect of market affordability has been overlooked, posing a serious barrier for ERAs to find their applications in today's industry. This paper introduces the third generation of the PCSs, where industrial justification and cost is equally weighted along with the electromagnetic performance. Here, in the third generation of PCS, dielectric substrates are made redundant for the first time, making a breakthrough in relation to the fabrication cost, while the electromagnetic performance is not sacrificed and comparable with the previous high-cost generations. The proposed All-Metallic PCS (AMPCS) is made of three stainless steel surfaces segregated with a sub-wavelength air-gap, without the need for any bonding techniques, as opposed to all other classes of PCS which either require thick and lossy dielectric thicknesses, or multiple of expensive printed RF laminates. The rest of this paper is organized as follows. Section 5.3 describes briefly the phase defect of a typical ERA and suggest the macroscopic and microscopic configurations of the AMPCS. Section III discusses the fabrication process of the proposed AMPCS and some special considerations need to be taken into account for metal manufacturing. Section IV presents the near-field and far-field results of

the antenna system, highlighting the AMPCS performance.

5.3 Design of the AMPCS

The design procedure of AMPCS can be divided into two major steps, in which a macroscopic configuration of the AMPCS is firstly suggested based on the nature of the near-field non-uniformity of the electromagnetic (EM) source under examination. To do so, an ERA is used as an example case of an aperture EM source suffering from a highly spherical wavefront. In the second step, microscopic topology is discussed, where the configurations of all-metal phase-correcting elements are proposed.

5.3.1 Macroscopic topology of the metallic PCS

A conventional ERA is composed of a partially reflecting surface (PRS) placed at a half wavelength from a ground plane containing a simple feed. The feed excites the cavity formed between the PRS and the ground plane [38]. In a different approach, fully reflecting surfaces can also be engineered to form an ERA as explained in [20, 47, 48]. Fig. 5.1(a) shows the ERA under examination with a flat unprinted surface as its PRS. The PRS is made of Rogers TMM 4 with a thickness of 3.17 mm, which is close to $\lambda_g/4$, as recommended in the literature [38, 39], and placed at a distance of $\lambda_0/2$ from the ground plane to construct a cavity, where λ_0 and λ_g are the free-space wavelength and guided wavelength within the PRS at the operating frequency of 11 GHz. The cavity was excited using a single slot antenna with an opening of 13.2 mm$\times$8 mm placed in the center of the ground. In order to calculate the phase errors in the antenna aperture originating from the transversal prorogation of the slot antenna, an imaginary plane is considered at a sub-wavelength distance of 7 mm from the antenna where the local phase values are measured and depicted by a 2D plot in Fig. 5.1(b). As can be seen from this plot, the near-field phase values are approximately independent with respect to ϕ in the cylindrical coordinates.

In order to discretize the aperture phase distribution, the actual phase values along the

$\phi = 0$, with an interval of $\lambda_0/3$ are captured in the imaginary plane, resulting in 7 discrete values, which are used to quantify the aperture phase-errors with respect to an arbitrary constant. The sampling interval is critical and chosen following the recommendations in [49,50,150,151], as large intervals would result in sub-optimal correction, due to discretization error and too small ones would cause fabrication complexity, especially for an all-metal structure. To correct such circularly symmetrical, yet highly non-uniform, phase distribution of the antenna, the proposed AMPCS needs to follow the same symmetry, resulting in a semi-rotational orientation of 7 different phase-correcting elements, as shown in Fig. 5.2. It should be noted that such arrangement is not singular and any other circular patterns inspired by the actual near-field phase distribution of the EM source can be used. Knowing the macroscopic structure of the AMPCS and the required localized phase correction, next step is to design phase-correcting element of the AMPCS.

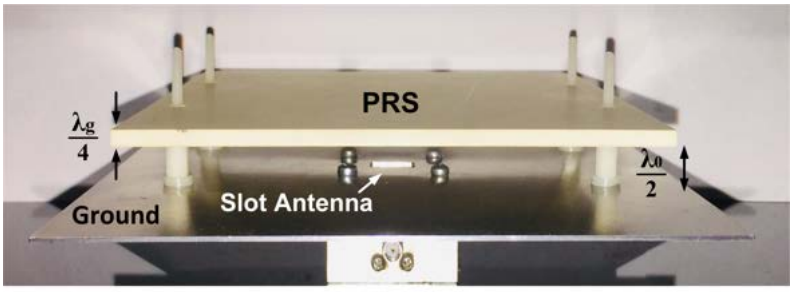

(a)

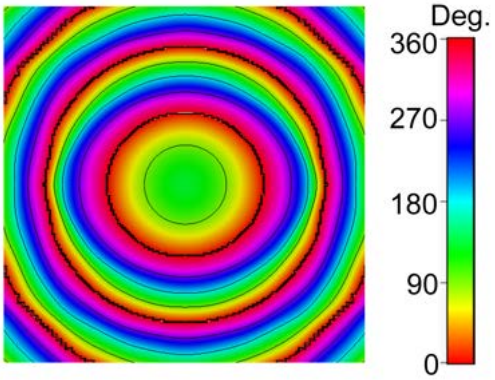

(b)

Figure 5.1: (a) A photo of the fabricated ERA with an unprinted PRS made of Rogers TMM 4. (b) 2D presentation of the phase distribution of E_y 7 mm above the antenna aperture.

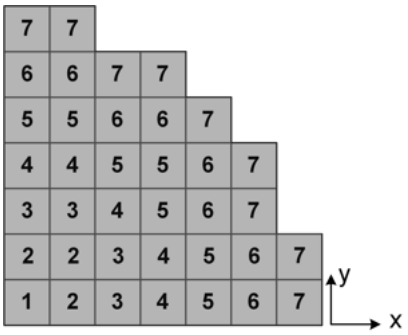

Figure 5.2: Quasi-circular arrangement of the phase-correcting elements used for the AMPCS realization.

5.3.2 Microscopic topology of AMPCS

The Second generation of PCSs are generally composed of localized spatial phase shifters developed by stacking multiple expensive RF laminates. The use of dielectric as a substrate for the metallic patterns along with a wide variety of available substrates (numerous dielectric constants and thicknesses) provides PCS designers with an extremely large degree of freedom to achieve the transmission properties required throughout the PCSs [17,18,21,22,25,141]. Indeed, any conductive patterns, resonant or non-resonant elements, with any commercially available substrates can be used to achieve a transparent structure with the required phase delay at the operating frequency. On the other hand, such flexibility does not exist with all-metal configurations. Therefore, none of the proposed configurations of printed phase-correcting elements in the literature can be implemented in a fully metallic topology.

To tackle this issue, we propose a hybrid all-metal configuration for the phase-correcting elements, in which different numbers of segregated conductive layers are used. In the proposed configuration, the consistency and the mechanical integrity, which are the main barriers to the all-metal EM devices, are ensured by an inductive metallic grid extending throughout AMPCS structure. The justification to use such a high-impedance metallic network is grounded by the fact that the resonance condition can be potentially satisfied by a combination of the inductive effects of two segregated metallic grids and the capacitive effects of the transmission line placed

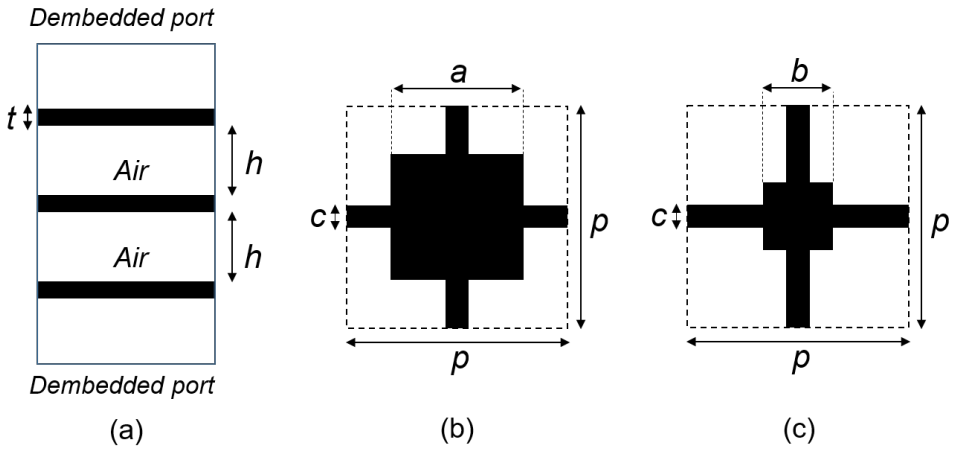

Figure 5.3: Unit-cell configuration of the proposed all-metal phase shifters. (a) Side view of a unit cell of the AMPCS. (b) Top and bottom conductive patterns of a unit cell of the AMPCS. (c) The middle conductive pattern of a unit cell in the AMPCS. In each unit cell, the square paths are held by the inductive strips with a constant width of c. The inductive strips running throughout the three surfaces, responsible for the integrity of the structure.

between the two grids. Consequently, it can be hypothesized that a pair of inductive grids will create a high-transmission window around their resonance, making them a possible phase-correcting element, in addition to their primary role of ensuring mechanical consistency of other metallic patterns used in the future phase-correcting elements.

To verify this hypothesis, a parametric analysis of two identical metallic grids separated by 10 mm ($\approx \lambda_0/3$) with varying widths from 0.4 mm to 1.6 mm and a step of 0.1 mm was carried out using CST MWS. According to the numerically computed transmission coefficients, a phase range of 100 degrees (125° to 225°) with reasonably high transmission magnitude can be achieved by this simple structure. The significance of this relatively small phase range will be revealed when other patch-based phase-correcting topologies are designed in the following and appear to fail to fill the same phase-range.

The proposed all-metal phase-correcting element consists of three inductive grids separated by nearly $\lambda_0/3$ as a base to hold the three metallic patches as shown in Fig. 5.3. The size of each element is set to $\lambda_0/3$ and denoted by p in Fig. 5.3. To ensure simplicity of the proposed AMPCS,

the top and bottom patches are designed to be identical with a maximum size of $p = \lambda_0/3$. In this configuration, the width of the grid and the thickness of both patches and girds are set to 0.4 mm and 1 mm, respectively, considering the limitations associated to the laser cutting which is used in the fabrication process and discussed in Section Section III. The size of the square patches, however, are varied to achieve the required phase shifts using a parametric study with a step size of 0.3 mm chosen based on the fabrication tolerance.

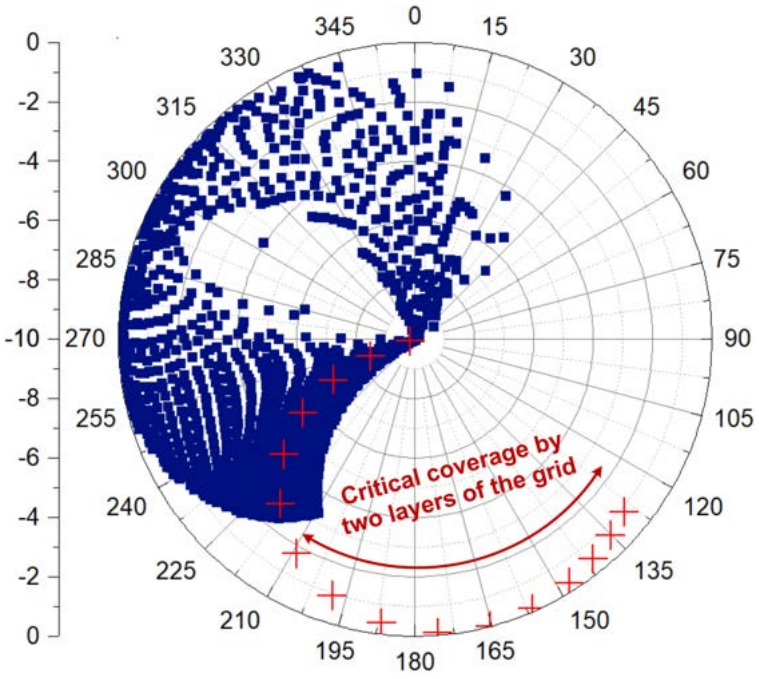

Figure 5.4: Polar representation of the transmission coefficients generated by the proposed hybrid all metal configuration. The blue squares represent the transmission components of three square patches connected by the three layers of the metallic grid. Red crosses show the transmission coefficients of two layers of the grid in the absence of metallic patches.

The transmission phase and magnitude at the operating frequency of 11 GHz are extracted from the parametric study and illustrated through a polar graph shown in Fig. 5.4. In this plot, the transmission characteristics of each phase-correcting element is presented by a blue square, suggesting the incapability of the unit-cell configuration in Fig. 5.3 in covering the phase values of 45° to to 210°, which would be a barrier for the phase correction of EM sources with a severe

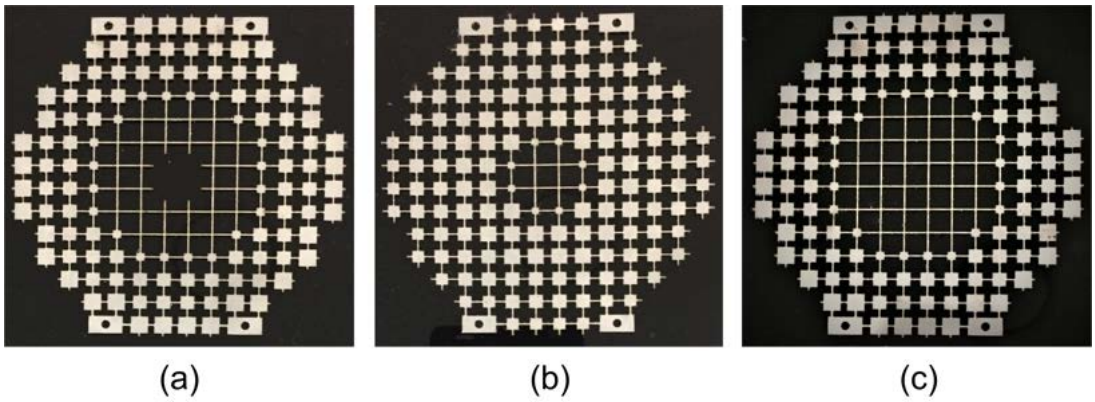

Figure 5.5: Laser cut AMPCS made of stainless steel sheet with a thickness of 1 mm.(a) top layer, (b) middle layer, (c) bottom layer.

aperture phase non-uniformity like the ERA under consideration. This problem is rectified by using a pair of standalone inductive grids as phase-correcting elements, as explained earlier, and shown in red crosses in Fig. 5.4. In order to cover the phase range of 45 to 120, one more layer needs to be used in the AMPCS configuration. The final stage of designing AMPCS is choosing the suitable candidates from the element bank shown in Fig. 5.4 and arrange them in the pre-designed macroscopic regime discussed in Section 5.3.1, in which only 7 discrete correcting elements are required. The geometrical and EM properties of the unit cells used in the APMCS are tabulated in Table I.

5.4 Fabrication Considerations

There are a variety of fabrication methods which can be employed for realization of the proposed AMPCS, thanks to the recent advancements in the metal manufacturing technology. There are five possible prototyping procedures including Computer Numerical Control (CNC) machining [152], plasma cutting [153], metal additive manufacturing [154], waterjet cutting [155] and laser cutting [156]. Amongst them, we highly recommend the last two methods for the AMPCS prototyping. Indeed, the sharp vertex of the perforated polygons cannot be achieved using CNC machining, due to the round tip of CNC bits, additionally there is a high chance of metal

Table 5.1: Geographical and electromagnetic properties of the phase correcting elements used in the AMPCS at 11 GHz.

Ring no.	$\lvert S21\rvert$ (dB)	$\Delta\phi$ (Deg.)	No. of Layers	a (mm)	b (mm)	c (mm)
1	00	187	2	0	0	0.8
2	-2.7	214	3	0	2.7	0.4
3	-0.1	255	3	0	6.2	0.4
4	-0.2	296	3	3.3	6.2	0.4
5	-0.5	330	3	5.4	5.5	0.4
6	-0.5	330	3	5.4	5.5	0.4
7	-3.0	12	3	6.8	4.8	0.4

failure during drilling because of the small thickness of the metal sheet. Secondly, plasma cutting performs efficiently only for large cutting areas with simple patterns, while the AMPCS has many miniature segments which would be damaged due to the destructive influence of plasma cutting on the confluences. Metal additive manufacturing is a very precise method for prototyping metallic objects with delicate segments; however, it is not recommended in the case of AMPCS, as the 3D printed AMPCS would be highly subject to damage, when it is removed from the printer bed, due to its small thickness. Either water-jet cutting and laser cutting can be used to fabricate the proposed AMPCS, as both method are capable to finely perforate metal sheets; nevertheless, the water-jet cutting is a lengthier process than laser cutting, leading to a higher fabrication cost, hence the AMPCS was fabricated using laser cutting technology.

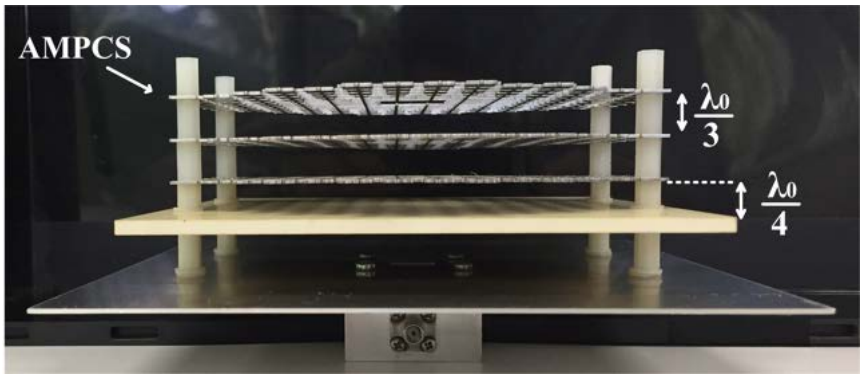

Figure 5.6: A prototype of the fabricated AMPCS loaded on the ERA. The AMPCS and the PRS are made of thin sheets of stainless steel, and Rogers TMM4, respectively.

The proposed AMPCS was made of stainless steel sheets using cutting-edge laser technology. The thickness of the metallic sheets plays a critical role in both fabrication and durability of the AMPCS. From the packaging points of view, greater thickness is preferred, as it is more sustainable and removes the need for any extra supports, such as radome or foam substrate. However, increase in the metal thickness would escalate the chance of metal failure during the fabrication process, due to the excessive heat absorbed by the thick metal sheet. Therefore, there is a trade-off which needs to be addressed at the beginning of the design process. In this design, the thickness of 1 mm is recommended considering the large volume of perforation performed on each surface of the AMPCS. Such selection ensures both fabricability and robustness of the freestanding AMPCS.

5.5 Near-field and Far-field Results

Fig. 5.5 shows three layers of the AMPCS fabricated by a laser cutting machine (HL-6060C) with a maximum line cutting speed of 800 mm/s. The layers are separated with 4 nylon spaces to form the AMPCS, and placed on the antenna at a distance of $\lambda_0/4$ from the PRS, as depicted in Fig. 5.6. The near electric field of the antenna system was numerically calculated using the time-domain solver of CST Microwave Studio (CST MWS) and shown in Fig. 5.7. It can be

seen that a remarkable enhancement in the aperture phase distribution of the antenna system is achieved, extending the uniform phase region to more than double.

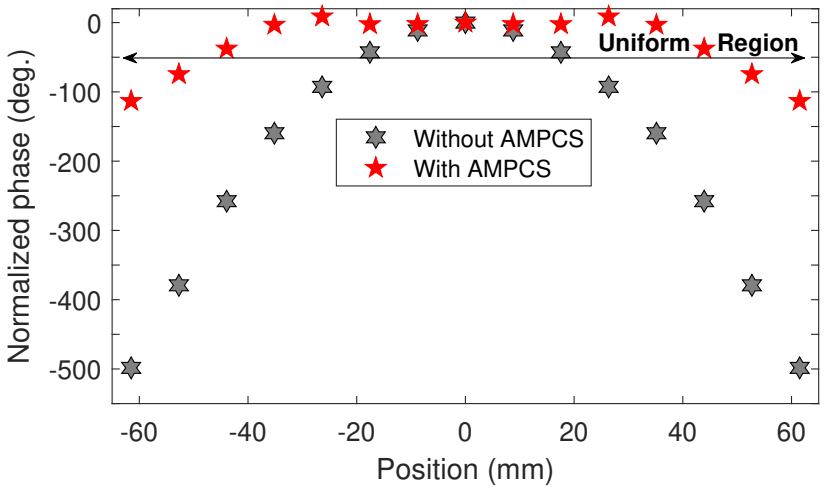

Figure 5.7: Phase distribution of the y-component of the electric field of the ERA under consideration at 11 GHz. Uniform phase region is more than doubled due to AMPCS.

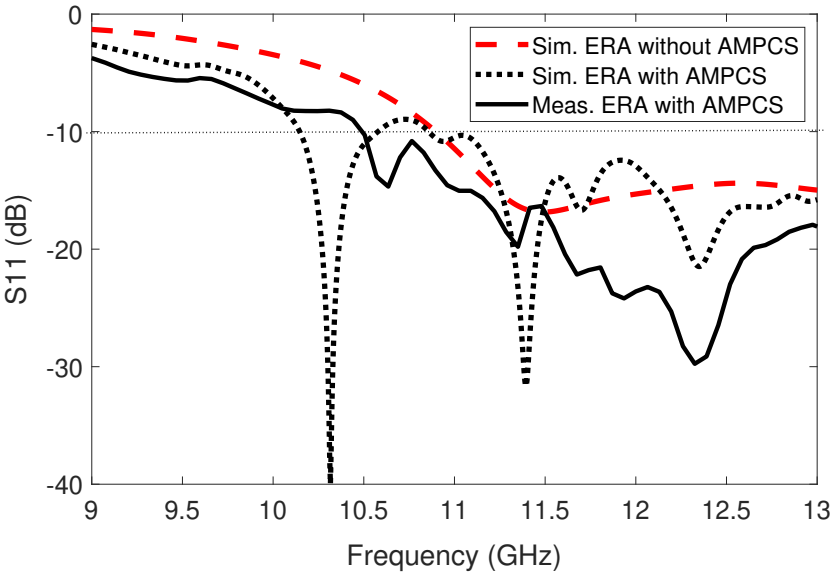

Figure 5.8: Input reflection coefficient of the antenna.

The input reflection coefficient of the ERA was simulated and measured using CST MWS and Agilent PNA-X N5242A vector network analyzer, respectively and plotted in Fig. 5.8. According

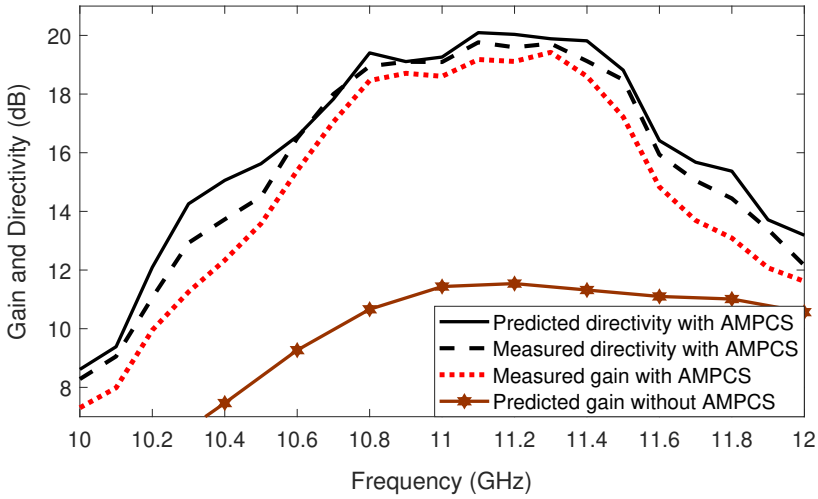

Figure 5.9: A comparison between the gain and directivity of the ERA with and without the AMPCS.

to the measured results, the 10 dB $|S11|$ bandwidth of the antennas with AMPCS is 42% from 10.6 to 16.3 GHz, which is in good agreement with the predicted values from CST MWS. Far-field peak gain and directivity of the ERA with AMPCS were measured in the Near-field Systems Inc. spherical near-field range, and compared with the predicated results in Fig. 5.9, verifying a significant improvement of 8.4 dB in the peak gain of the antenna, reaching to 19.42 dB at 11.3 GHz. According to the measurement, the 1 dB directivity and gain bandwidths are 6.4% and 5.9%, respectively, verifying stable far-field performance of the antenna system in a typical frequency band required for Ku-Band applications.

The improved directivity and gain of the ERA with the AMPCS is achieved due to the enhanced phase distribution of the antenna aperture, which can be seen from the visualized electric field radiation in the E-plane, shown in Fig. 5.10. This radiation snapshot depicts the transformation of the spherical wavefront to a nearly planar wavefront of the E_y, significantly increasing the aperture efficiency of the antenna from 4% to 28%, because of the AMPCS. The transparency of the AMPCS can be estimated by inspecting the colors representing the intensity of the electric field at the input and output of the AMPCS in Fig. 5.10. It can be observed that there are almost same colors (intensity) below and above the AMPCS, exhibiting a good

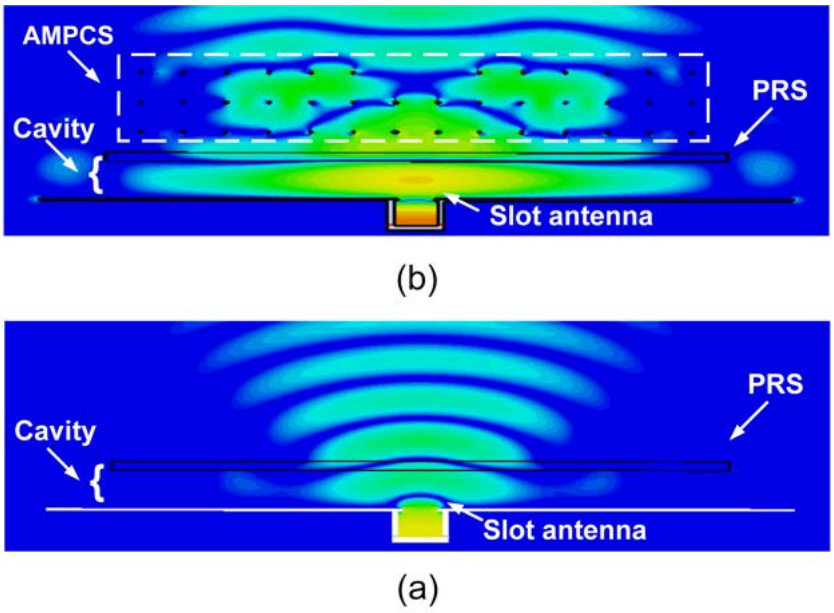

Figure 5.10: A visualized comparison between the E-plane electric field distribution of the antenna, (a) in the absence of AMPCS, (b) in the presence of the AMPCS.

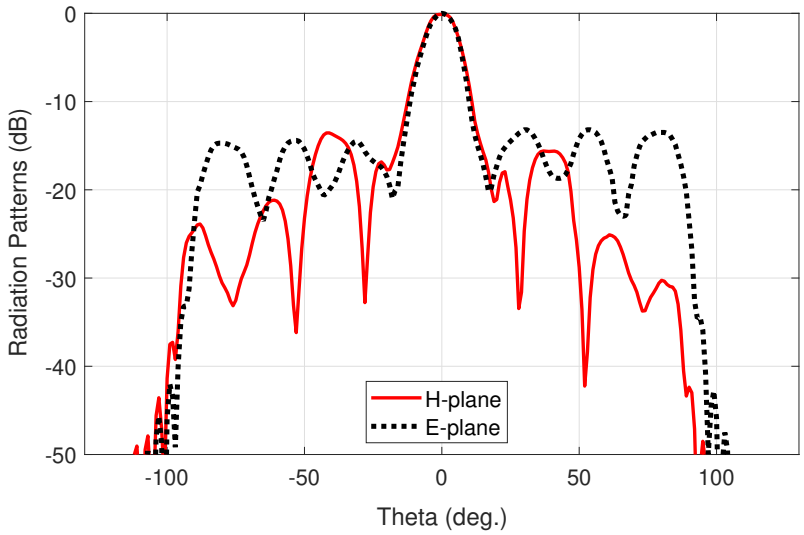

Figure 5.11: Measured radiation patterns of the ERA under the APMCS loading.

transmission properties in addition to the phase correction. Radiation patterns of the antenna in two principal planes are plotted in Fig. 5.11 showing, SLLs of -13.2 and -13.5 dB in the E- and H-planes, respectively, suggesting around 8 dB improvement in the SLLs in the E-plane over

the Bare ERA.

5.6 Conclusion

An industrially-justified approach has been proposed in this paper to rectify the near-field non-uniformity associated with the aperture antennas and successfully tested with an ERA. Unlike the first and second generations of the PCS, the proposed AMPCS neither requires expensive microwave substrates nor any bonding techniques, resulting in a substantially lower fabrication cost, removing the main industrial barrier to the ERAs applications. Additionally, the purely metallic configuration of the AMPCS does not add any further loss to the antenna system as opposed to all other substrate-based PCSs. A prototype of AMPCS was fabricated using available laser cutting technology and placed at a sub-wavelength distance from the ERA. The AMPCS has significantly compensate the non-uniform phase-delay of the antenna aperture, resulting in a considerable increase of 8.4 dB in the peak gain of the antenna, reaching a peak gain of 19.42 with a 1 dB gain bandwidth of around 6%. The measured radiation patterns are quite stable with SLLs better than -13 dB in both E- and H- planes, respectively. The proposed freestanding AMPCS does not need any mechanical support or protection and can be used for other aperture antennas for near-field enhancement.

CHAPTER 6

Dielectric-Less Wideband Frequency-Selective Surface Filter

6.1 Abstract

A novel technique to design a low-cost Frequency-Selective Surface (FSS) bandpass filter is presented in this paper. Wideband polarization-independent FSS bandpass filters are predominantly made of multiple microwave dielectric substrates, or non-commercially available composite materials with or without active components, contributing to a very high manufacturing cost. The presented FSS filter has neither microwave substrates, nor any active devices, while it has a large controllable operational frequency band, which can support all polarization, due to its symmetrical configuration. To the authors' knowledge, such polarization independent wideband bandpass response has never been achieved by any low-cost fully-metallic FSS filter. The proposed FSS filter is made of three thin metal sheets composed of an Engineered Metallic Substrate (EMS) and metallic Orthogonal Dipole Resonator (ODR). The EMS is responsible for ensuring mechanical

Under review as: Ali Lalbakhsh, Muhammad U. Afzal, Karu P. Esselle, Stepanie L. Smith, "Low-Cost Wideband Frequency-Selective Surface Bandpass Filter with a Polarization Insensitive All-Metal Structure," *IEEE Transactions on Antennas and Propagation.*

integrity of the filter without imposing electromagnetic restrictions throughout the desired frequency band. The integration of EMS and ODRs realizes a fully controllable wideband bandpass verified through both electronic- and electromagnetic-based analyses. According to the predicted and measured results, the filter has a large bandwidth of 31%, extending from 8.76 GHz to 11.96 GHz with sharp roll-offs for the normal incidence. The passband under oblique angles of 15°, 30° and 45° are 30% (8.81 GHz-11.91 GHz), 26.7% (9.1 GHz-11.88 GHz) and 23.4% (9.39 GHz-11.86 GHz), respectively.

6.2 Introduction

There is a wide variety of applications for Frequency-Selective Surfaces (FSSs) from radar and satellite communications to antennas and microwave systems [30, 42, 157–161]. FSS filters also known as spatial filters are a subgroup of FSSs which can provide lowpass, bandpass, highpass and bandstop frequency responses; however, unlike the microwave filters [162–175], the electric field polarization and the angle of incidence affect their frequency responses. Today, with acceleration of wireless communications development, the need for high data-rate transmission has created a high demand for broadband Electromagnetic (EM) devices. In the response to this need, various configurations for FSS filters have been proposed over the last decade [13, 23–30, 176–180].

One major design approach is based on using multiple printed dielectric layers, in which each layer exhibits non-resonance behavior, resulting in storing electromagnetic waves in the form of electric field and magnetic flux. In this class of filters, the desired frequency response is achieved by combining the mentioned magnetic and electric effects; [13, 23–25]. For example, sub-wavelength arrangements of capacitive square patches and wire grids are realized by multiple stacked Printed Circuit Board (PCB) to develop a bandpass spatial filter with around 20% bandwidth [13].

The other main design procedure of FSS filter is based on employing resonating elements, with or without resonating components, mainly polygonal patches or strips which are printed on one or multiple dielectric substrates. In this category of FSS filters, the desired frequency response

can be achieved by tuning the resonant frequencies of the resonating elements [26–30,181–183]. A fractional bandwidth of around 25% was reported by the these approaches. For example in [30], a combination of resonating printed structures with lumped elements on segregated dielectric substrates have been used to achieve a broadband dual-band spatial filter. Larger bandwidths would be possible by the combination of the methods explained above in conjunction with the application of active components in a more complex design [176–178,180]. In a different approach, three dimensional frequency selective configurations have been proposed to provide more degrees of freedom to realize a wideband frequency response [139, 184, 185]. For example in [184], an integration of the conventional printed FSSs with metallic rods connecting surfaces were proposed to eliminate higher spurious modes by tuning the inductance created by the rods.

Apart from the aforementioned design procedures, based on the commercially available dielectric substrates, some new frequency-selective structures have recently been proposed using metamaterials [51, 186–190]. It should be mentioned that some passive bandwidth extension methods based on dispersion engineered metasurfaces have been proposed in [191, 192].

Reviewing recent related works reveals that while there has been a prominent improvement in wideband polarization-insensitive FSS filters, critical aspect of manufacturing cost has been mostly sacrificed or even not been considered in the design methodology, making them a lavish high-end EM devices. It is mainly because the use of expensive microwave dielectric substrates, active devices and associated manufacturing techniques. Additionally, it may be preferred to avoid employing such substrates in applications with harsh environments, such as space exploration [193]. AP1911-2249 On the other hand, according to the literature, there are only a few all-metal wideband FSSs capable of bandpass filtering, which are all polarization dependent. [194,195]. This is because the existing knowledge from the extensive works on the dielectric based FSS filters cannot be directly implemented in an dielectric-less topology, due to the inconsistency created in conductive patterns.

Here, we address this challenge by presenting a mechanism, in which the mechanical integrity of the structure is ensured by an Engineered Metallic Substrate (EMS), which can also be tuned to shift the second harmonic to higher frequencies. The tunable wideband response is then real-

ized by introducing Orthogonal Dipole Resonators (ODRs), thanks to the structure consistency provided by the EMS. The role of each section of the proposed topology is theoretically discussed through equivalent-circuit models and modal analysis. It is shown that the odd-mode resonance can be independently controlled by the air-gap between the metallic layers of the filter and hence its passband can be tuned over a large frequency band. It should be mentioned here the integration of the EMS and ODR maintains the four-fold symmetry of the structure, and hence would not upset the polarization of the incoming waves. Additionally, the proposed spatial filter is optically transparent, light-weight, yet freestanding and robust, which can be used for outdoor high altitude/ harsh weather applications, without the need of any further protection.

6.3 Engineered Metallic Substrate (EMS) for the Spatial Filter

It is well-proven that a frequency filtering behavior can be expected when a resonance condition occurs in a circuit. Such condition can be met when either a resonator is designed within a FSS topology, or it consists of non-resonating inductive/ capacitive layers, which are stacked together. Both cases are generally implemented by either conductive patterns or conductive discontinuities, most of which are not possible without dielectric substrates. As a result, most of existing conductive patterns cannot be physically implemented on an all-metal structure, making a major barrier to design all-metal spatial filters. To tackle this issue, we propose an Engineered Metallic Substrate (EMS) which firstly ensures the physical consistency of the spatial filter, and secondly is able to hold other metallic resonators required for frequency-response tailoring. Apart from this mechanical capability, the EMS can be designed to not only exhibits a non-intrusive electromagnetic behavior over the desired frequency band, but it also can be tunned to suppress the second harmonic band, which is an advantage over the expensive commercial Radio Frequency (RF) dielectric substrates.

To meet both mechanical and electromagnetics requirements, an inductive Throughout Cross

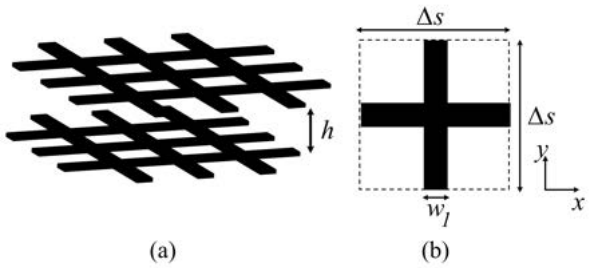

Figure 6.1: The proposed EMS. (a) Side view. (b) Top view of one unit cell.

(TC) with a constant thickness (t), a constant length (Δs) and a varying width (w_1) is proposed and shown in Fig. 6.1. Two layers of the inductive TCs placed at a distance of h can potentially create a resonance condition, which is controlled by w_1 and h. The thickness of the metal is chosen based on the robustness, weight and fabrication constraints. In this design, t and Δs are set to 1 mm ($\lambda_0/27$) and 9 mm ($\lambda_0/3$), respectively. Theses selections ensure the mechanical integrity of the structure through an affordable prototyping mechanism.

A resonance map of the EMS is plotted in Fig. 6.2 as a guide for choosing the appropriate combination of w_1 and h based on the EM and mechanical design requirements. In this design example, the center frequency and the 3-dB bandwidth of the spatial filter are to be 10.50 GHz and 30%, respectively. Hence, the combination of $h = 8$ mm and $w_1 = 0.4$ mm are chosen for the EMS to meet this requirement, as well as the fabrication constraints. We recommend the EMS's transmission pole to be tuned close to the upper edge of the desired bandwidth, as it would minimize the effect of the second harmonic of the EMS after integration with the new resonators.

6.4 FSS Filter Synthesis

6.4.1 Metallic Orthogonal Dipole Resonator (ODR)

To realize a bandpass response with a large bandwidth, more resonances are required to be introduced within the desired frequency band. This can be achieved by introducing an additional

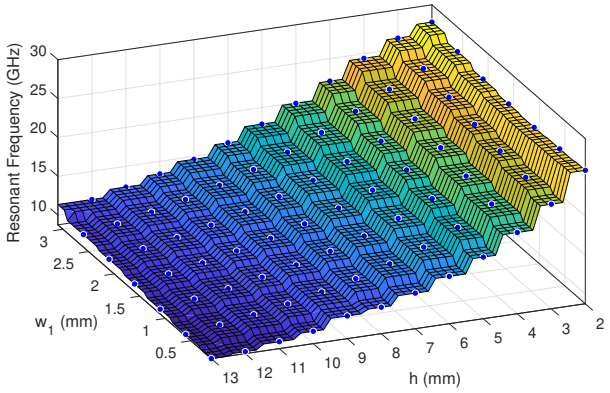

Figure 6.2: Resonance map for the proposed EMS.

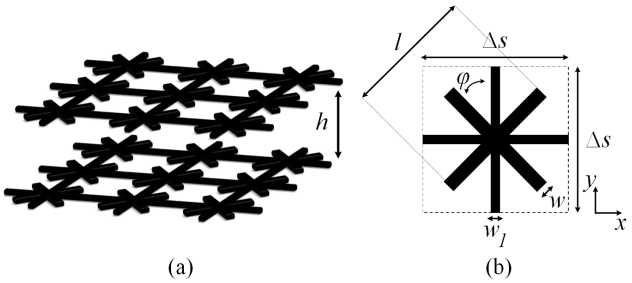

Figure 6.3: The integration of TCs and ODRs. (a) Side view. (b) Top view of one unit cell.

resonator into the EMS. It should be mentioned that any resonators even those with conductive discontinuity can be incorporated in the FSS filter configuration, thanks to the unconditional structure consistency ensured by the EMS explained in the previous subsection. So, two Orthogonal Dipole Resonators (ODRs) with an angle of ϕ with respect to TCs are incorporated into the EMS and shown in Fig. 6.3. In this design, ϕ is set to 45^o for maintaining polarization insensitivity of the FSS filter, and w is set to 0.6 mm, as the width of the dipoles is subordinate to their lengths. Hence, the number of unknown design parameters reduces to one, where l is the only parameter to control the ODRs' resonances, minimizing the tuning complexity of the proposed filter. A parametric analysis can be employed to find the most appropriate value of l. However, the placement of the second conductive layer at a distance of h results in the second resonance controlled by both l and h.

6.4.2 Even and Odd Mode Analysis

The presented configuration introduces two fully tunable resonances by which the passband can be adjusted. One resonance is merely controlled by the metallic segments, while both metallic and air-gap segments contribute into the other resonance. In order to give a better insight into the filtering mechanism and predict the electromagnetic behavior of the presented FSS filter, equivalent-circuit models are presented to electronically explain the controllability of the resonances using even and odd mode analysis. Two simplified equivalent-circuits are extracted from the FSS filter topology shown in Fig. 6.3 for the case of tight and loose coupling conditions that may occur for different values of h. In the case of tight coupling defined when $h =< 6$ mm, L_1 and L_t represent the inductive TC and the air transmission line, receptively, and C_g represents the coupling between the two conductive layers, as illustrated in Fig. 6.4 (a). The ODRs are modeled by a shunt-connected series L-C resonator, represented by L_2 and C_2 in Fig. 6.4 (a). The combined effects of the parasitic capacitances and the fringing fields are modeled by C_1. The equivalent-circuit associated to the loose coupling condition will be discussed afterwards.

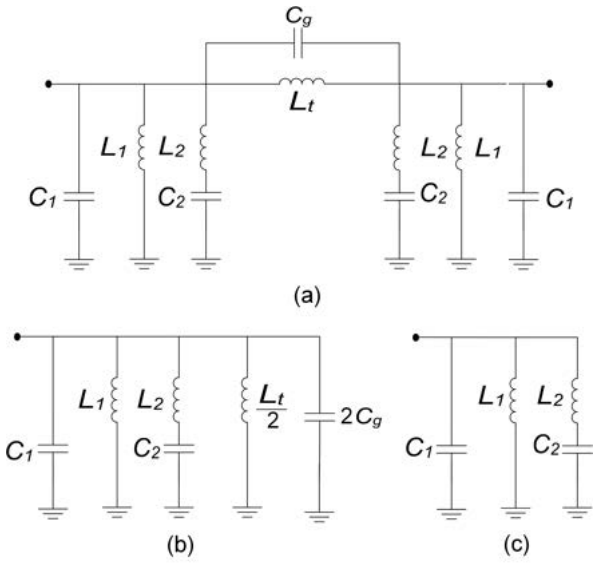

Figure 6.4: (a) Equivalent-circuit model of the proposed all-metal FSS filter for the case of tight coupling ($h =< 6$ mm). (b) Odd mode. (c) Even mode.

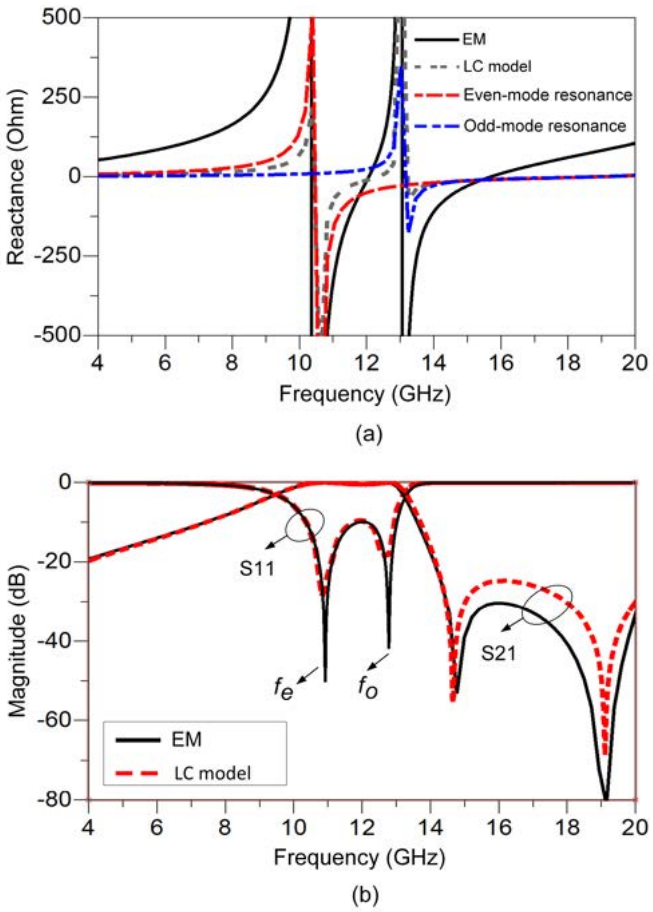

Figure 6.5: Equivalent-circuit models and EM simulation results of the proposed metallic FSS filter for the case of $h = 2$ mm. (a) Validation of the modal resonances. (b) S-parameters. The optimized lumped elements values for the example case of $h = 2$ mm are: $L_1 = 0.2438\ nH$, $L_2 = 0.24074\ nH$, $L_t = 0.15101\ nH$, $C_g = 0.77\ nH$, $C_1 = 0.50\ pF$, $C_2 = 0.2892\ pF$.

Modal analysis can be used to theoretically discuss the contribution of each section of the FSS filter to the resonances. In the odd-mode excitation, the symmetry plane of the circuit acts as an electric wall, resulting in the odd-mode equivalent-circuit, as shown in Fig. 6.4(b). This mode controls the upper resonance, which is also verified by the input reactance of the EM and LC models calculated for the example case of $h = 2$ mm shown in Fig. 6.5(a). A further verification is obtained through the good agreement observed in Fig. 6.5(b) between the S-parameters calculated for the EM and LC models. Therefore, varying the air-gap merely affects

the upper transmission pole and has no effects on the even-mode resonance. As a result, the upper edge of the passband can be easily adjusted by varying h modeled by L_t in the equivalent-circuit.

In the even-mode excitation a magnetic wall is created in the symmetry plane, resulting in the even-mode equivalent-circuit depicted in Fig. 6.4(c), which creates the lower resonant frequency. This can also be verified through the input reactance and the S-parameters of the even-mode equivalent-circuit, plotted in Fig. 6.5(a) and Fig. 6.5(b), respectively. To adjust this resonance, the length of the ODRs can be optimized, as this parameter directly controls the associated inductance (L_2).

In the case of loose coupling condition, defined when $h > 6$ mm, the air-gap is modeled by a capacitor (C_t) series with the transmission-line inductor (L_t) illustrated in Fig. 6.6(a), which causes the odd-mode resonance to occur at a lower frequency than that of the even-mode. Similar to the model presented in Fig. 6.4, the odd-mode resonance can be swept by only varying the air-gap (L_t in the LC model), while the even-mode transmission pole (the upper resonance) remains unchanged. This can be verified by comparing both S-parameters and the input reactances of the EM and LC models for an example case of $h = 8$ mm, which are plotted in Fig. 6.7(a) and Fig. 6.7(b), respectively. According to the presented equivalent models, the odd-mode resonance can be swept over a large frequency band, above and below the even-mode resonance, only by varying L_t, representing the air-gap (h) in the FSS filter configuration. This can be verified by plotting the magnitude of the reflection coefficient for various vales of h, as shown in Fig. 6.8. As can be seen from this figure, when air-gap (h) increases from 1 mm to 10 mm, the odd-mode resonance shifts to lower frequencies, while the even-mode resonance remains almost unchanged. As a result the passband of the FSS filter can be passively tuned by only varying h, without the need of any active devices or redesign and re-fabrication. In addition to the passband tunability of the filter, Fig. 6.8 verifies the accuracy of the equivalent circuit models for tight and loose coupling conditions, shown in Fig. 6.4 and Fig. 6.6, respectively as a very good agreement can be observed between the EM and LC models' results.

Based on the presented analysis, it can be hypothesized that the proposed configuration offers modular geometry reconfigurabilities, as the passband of the FSS filter (upper edge of the

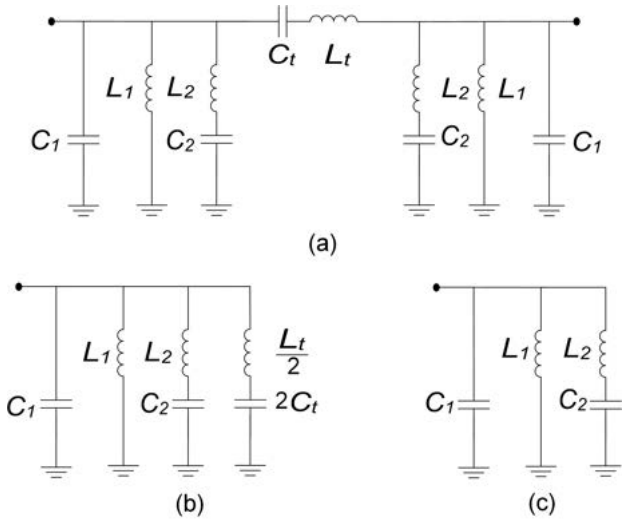

Figure 6.6: (a) Equivalent-circuit model of the proposed all-metal metasurface filter for the case of ($h > 6$ mm). (b) Odd mode. (c) Even mode.

passband in the case of tight coupling and the lower edge in the case of loose coupling) can be adjusted over a large frequency window which is a unique characteristic, considering the low-cost passive metallic configuration of the proposed FSS filter.

6.4.3 Current Distribution and Polarization Insensitivity

The generation of the resonances through induced currents on the FSS filter can be visualized using the current distributions of the FSS filter at the critical frequencies of transmission poles/zeros. Surface current distributions at lower and upper transmission poles are depicted in Fig. 6.9 and Fig. 6.10, respectively. In these figures the current direction and intensity are represented by arrows and colors, respectively. As can be seen from Fig. 6.9(a), at the lower transmission-pole frequency, the current is distributed on the ODRs as well as sections of the TCs which are parallel to the excited electric field (E_x). Similarly, in the case of y-polarized electric field (E_y), the current is dominantly induced on the whole metallic structure except for the perpendicular section of TC to the electric field. The same explanation can be said for the surface current at the upper transmission-pole frequency, as illustrated in Fig. 6.10. At the transmission-zero

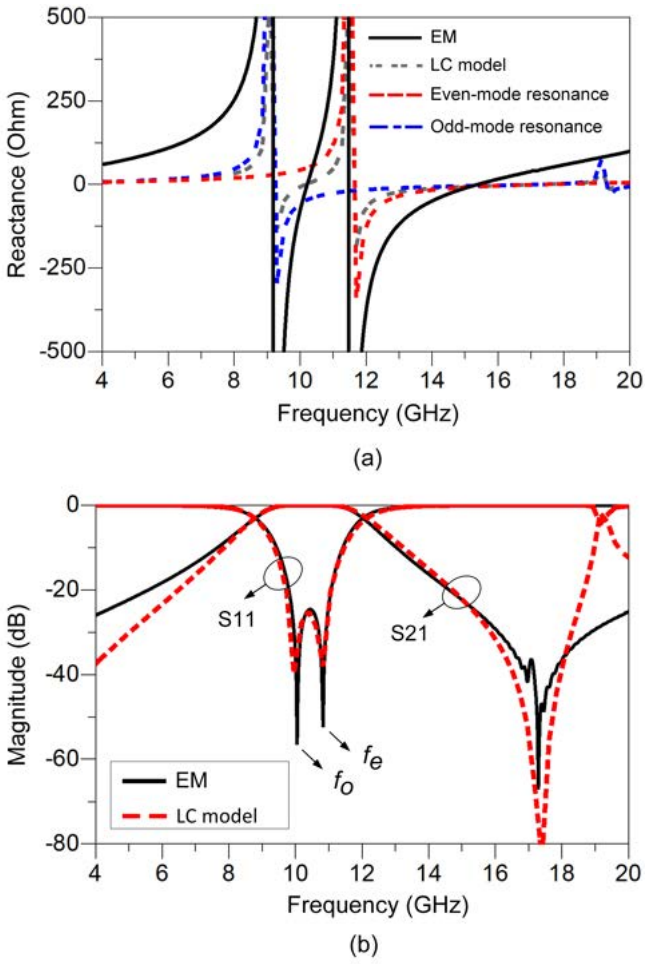

Figure 6.7: Equivalent-circuit models and EM simulation results of the proposed FSS filter for the case of $h = 8$ mm (a) Validation of the modal resonances. (b) S-parameters. The optimized lumped elements values for the example case of $h = 2$ mm are: $L_1 = 0.2506\ nH$, $L_2 = 0.21\ nH$, $L_t = 0.20\ nH$, $C_t = 0.26\ nH$ $C_1 = 0.04\ pF$,$C_2 = 0.401\ pF$

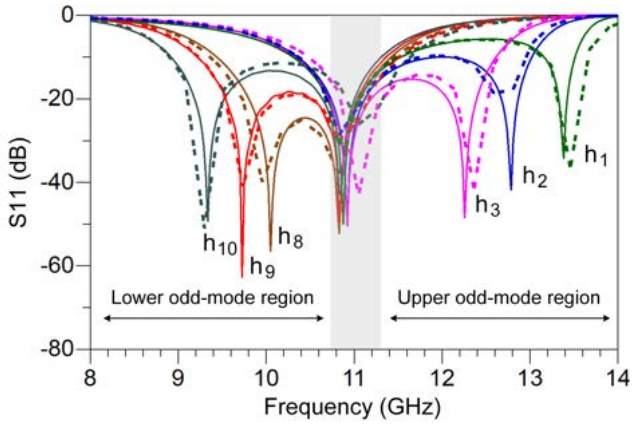

Figure 6.8: Tunability of the odd-mode resonance by varying h. Solid line represents the EM simulated results of the FSS filter. Dotted line shows the results of the lumped circuit models of the FSS filter for the case of tight and loose coupling conditions. Increasing air gap (h) from 1 mm to 10 mm, causes the odd-mode resonance to shift to lower frequencies, while the even-mode resonance remains almost unaffected, which suggests the passband tunability of the FSS filter by only varying h. The gray area around 11 GHz shows the negligible variation of the even-mode resonance. The values of the air gap and their associated inductances are as follows: $h_1 = 1\ mm,\ L_{t1} = 0.1301\ nH$, $h_2 = 2\ mm,\ L_{t2} = 0.15101\ nH$, $h_3 = 3\ mm,\ L_{t3} = 0.1606\ nH$, $h_8 = 8\ mm,\ L_{t8} = 0.20\ nH$, $h_9 = 9\ mm,\ L_{t9} = 0.24\ nH$, $h_{10} = 10\ mm,\ L_{t10} = 0.3701\ nH$.

frequency, the current distribution is dominantly induced on the first layer of ODRs, preventing significant current flows on the second layer, resulting in an almost no propagation after the first layer at 17.4 GHz, as shown in Fig. 6.11. This is because of the dominant effect of the ODRs, modeled as a shunt-connected series L-C resonator in the equivalent-circuit model.

In summary, the design procedure can be summarized in 3 straightforward steps:

1- Synthesizing the EMS using the resonance map in Fig. 6.2, based on the mechanical and electromagnetic requirements of the application. The recommended combination of w_1 and h are those which create a resonance close to the upper edge of the desired band. Such selection minimizes the unwanted effects of the spurious second harmonic.

2- Choosing the ODR length to introduce the even-mode resonance within the desired band, which can be done by a parametric analysis. We recommend to set w to a constant value chosen according to the fabrication constraint, and only sweep l, as w has a subordinate effect on the even-mode resonance.

3- Re-tuning the air-gap between the two metallic layers (h) to adjust the central frequency and the bandwidth, as the odd-mode transmission pole can be easily swept over a large frequency window only by varying h, as explained and verified electromagnetically in the previous section.

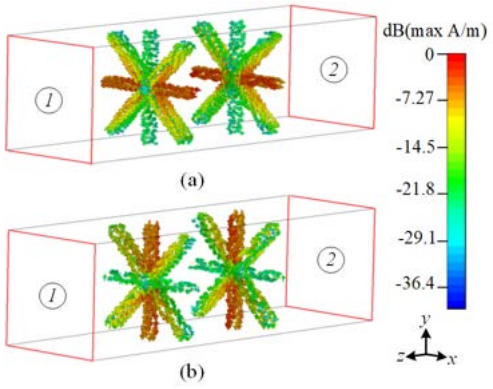

Figure 6.9: Surface current distribution at the lower transmission-pole frequency under periodic boundary conditions. (a) E_x polarization. (b) E_y polarization.

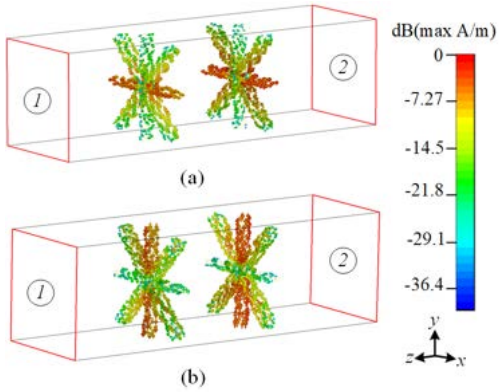

Figure 6.10: Surface distribution at the upper transmission-pole frequency under periodic boundary conditions. (a) E_x polarization. (b) E_y polarization.

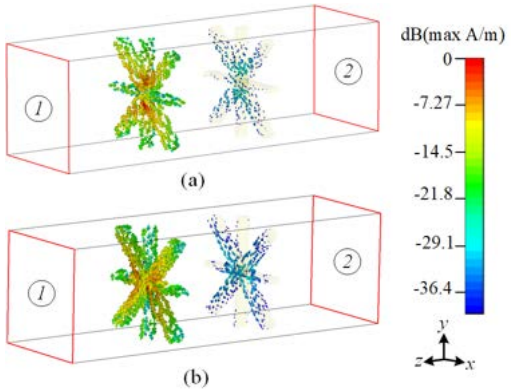

Figure 6.11: Surface current distribution at the transmission-zero frequency under periodic boundary conditions. (a) E_x polarization. (b) E_y polarization.

6.5 Higher Order FSS Filter and its Tunability

In order to achieve a bandpass response with higher selectivity, more resonances are required to generate additional transmission poles and transmission zeros. This can be done by increasing the number of metallic layers with the same spacing. Such arrangement would not disturb the passband and only improves the out-of-band response of the filter, by shrinking the transition band (a frequency band with insertion loss between 3 dB and 20 dB) and extending the stopband.

It can be observed through Fig. 6.12 that the upper transition band is reduced from 1.95

GHz to 1.35 GHz, 0.82 GHz and 0.54 GHz for the case of 2, 3, 4 and 5 layers of the FSS filter, respectively. The lower transition band exhibits a similar improvement by shrinking from 3.54 GHz to 1.3, 0.75 GHz and 0.50 GHz, because of increasing the number of metallic layers from 2 to 5, respectively. The upper stopband with an attenuation level of 20 dB extends upto 2.1f_c, 2.35f_c, 2.43f_c and 2.45f_c for the cases of 2, 3 , 4 and 5 layers, respectively. The lower stopband has a rejection level better than 20 dB at all frequencies for all cases.

It has been discussed earlier in modal analysis that the proposed FSS filter has a mechanically reconfigurable frequency response, in which the passband can be passively adjusted only by tunning the air-gap (h) between the metallic layers without any changes that require re-fabrication. As can be seen from Fig. 6.13, the central frequency is swept from 11.27 GHz to 10.10 GHZ, with varying h from 4 mm to 8.5 mm, while the fractional bandwidth is not affected and remains around 30% for all cases. The quality of in-band as well as out-of-band response remain almost unaffected, as the insertion loss levels in the passband and the stopband are better than 1 dB and 20 dB, respectively. Larger sweep in the central frequency is possible at expense of some ripples in the passband.

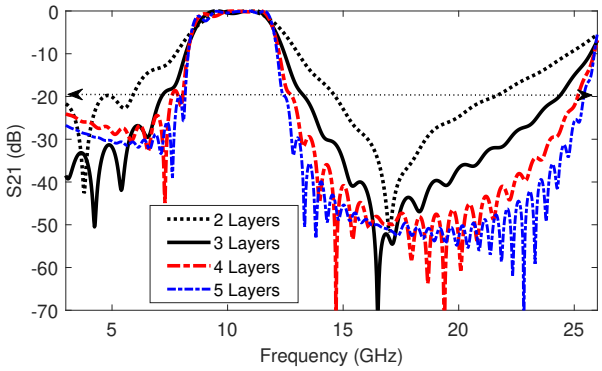

Figure 6.12: Out-of-band response of the filter for different numbers of metallic layers with a constant air-gap of 8 mm. The upper transition band reduces from 1.95 GHz to 1.35 GHz, 0.82 GHz and 0.54 GHz for the case of 2, 3, 4 and 5 layers of the FSS filter, respectively. Similarly, the lower transition band shrinks from 3.54 GHz to 1.3, 0.75 GHz and 0.50 GHz, for the case of 2, 3, 4 and 5 layers, respectively.

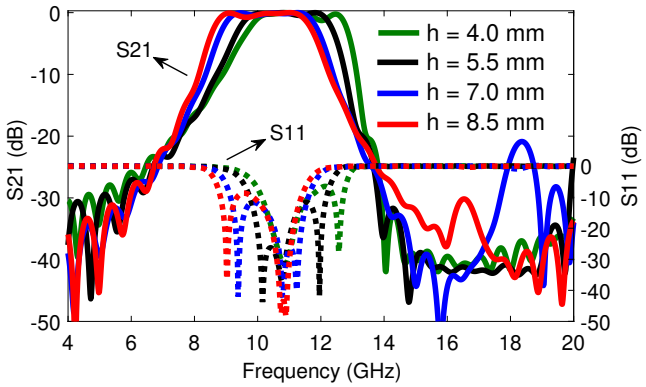

Figure 6.13: Passband adjustability of the FSS filter for various air-gaps. The center frequency of the filter can be tunned within a large frequency window from 11.27 GHz to 10.10 GHZ, without affecting the fractional bandwidth which remains around 30%

6.6 Prototyping and Measurement

The proposed FSS filter can be fabricated using the available technologies employed for metal prototyping. Amongst all available metal manufacturing methods, including plasma cutting, additive manufacturing, CNC machining, water-jet cutting and laser cutting, we recommend the last two methods. However, laser cutting is a faster method and incurs lower cost compared to water-jet cutting, and hence it is recommended especially for developing larger pieces of the FSS filter. A laser cutting machine (HL-6060C) with a maximum line cutting speed of 800 mm/s was used to remove numerous minute polygons from stainless steel sheets to form one layer of the FSS filter with a size of 302 mm×302 mm including 1089 square unit cells and 5 mm surrounding margin, as shown in Fig. 6.14. The proposed configuration makes large-scale low-cost prototyping possible for passively reconfigurable wideband radiation-hardened devices, which was otherwise not possible.

The proposed configuration has also the advantage of optical transparency, as shown in Fig. 6.14, which is an increasingly necessary for windows and domes of space observation and communication as well as observation windows of medical electromagnetic isolation rooms. One of the unique specifications of the proposed all-metal filter is its porous, yet mechanically robust,

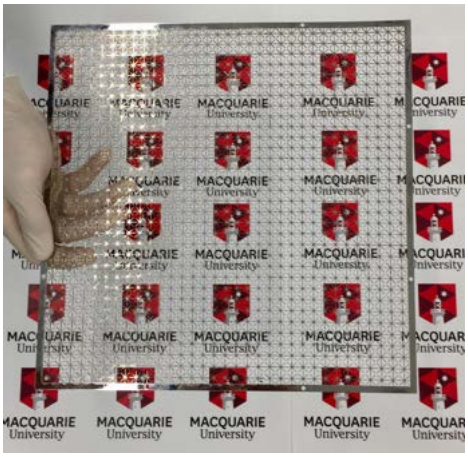

Figure 6.14: Optically transparent FSS filter developed using laser cutting technology.

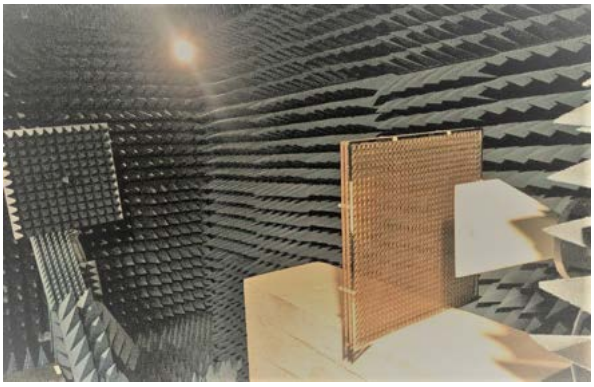

Figure 6.15: Measurement set-up in anechoic chamber, including the fabricated metasurface with three metallic layers.

configuration, which makes it a viable solution for the outdoor high altitude/ harsh weather applications, such as EM shielding for critical military/civilian devices, without the need of any further protection.

To experimentally verify the performance of the FSS filter, three identical layers of the perforated stainless steel were fabricated and separated by 8 nylon spacers on the perimeter of metal sheets, as shown in Fig. 6.15. The FSS filter is measured by a free-space measurement comprising standard open-ended waveguides and horn antennas, which were used as transmitter and receiver, respectively, and a vector network analyser connected to the receiver horn antenna. Fig. 6.15 shows the measurement setup in an anechoic chamber.

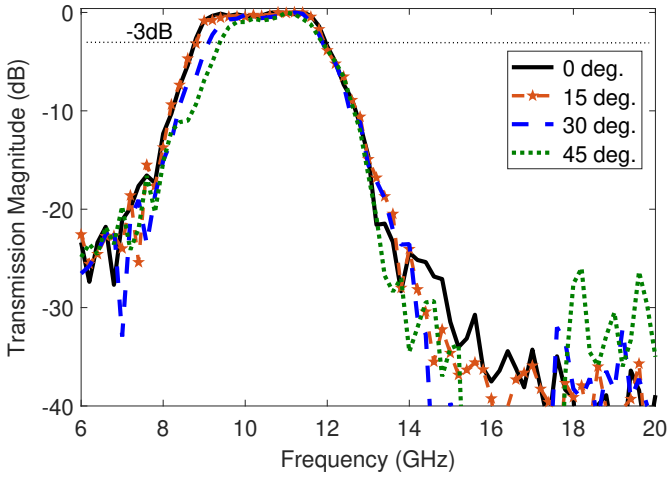

Figure 6.16: Measurement results at incidence angles of the FSS filter composed of 3 metallic layers.

The FSS filter was placed in the far-field region of the transmitter (around 2.5 meters away), so that it receives plane waves. The receiver horn antenna is placed nearly 0.2 m behind the FSS filter to collect the electromagnetic waves propagated through the FSS filter. The transmission magnitude of the filter was then calculated using the transmission magnitude of the measurement setup before and after the placement of the filter. In order to demonstrate out-of-band as well as in band frequency response of the prototype, four different waveguides (WR159, WR112, WR75 and WR51) and corresponding horn antennas are used to cover a large frequency range of 4 to 20 GHz. The measured transmission magnitude of the FSS filter with 3 layers is shown in Fig. 6.16, suggesting very good stability in the frequency response in both pass and out-of-band for different incidence angles. The measured 3 dB passband of the FSS filter extends from 8.76 GHz to 11.96 GHz, corresponding to a fractional bandwidth of 31% for the case of normal incidence. The passband, however, slightly reduces when the oblique angle increases, reaching to 30% (8.81 GHz-11.91 GHz), 26.7% (9.1 GHz-11.88 GHz) and 23.4% (9.39 GHz-11.86 GHz) for the case of 15°, 30° and 45°, respectively. It should be mentioned that all numerical simulations were carried out using the transient time domain of commercial software Computer Simulation Technology (CST) Microwave Studio. To predict the scattering parameters of the filter, unit-cell model was used, in which an infinite repetition of unit cells is assumed in transverse (x and

y) directions to realize periodic boundary conditions. Additionally, all lumped-element circuits were numerically analyzed using Advanced Design System (ADS).

6.7 Conclusion

A new class of low-cost FSS filter made of inexpensive thin layers of metal sheets suitable for all polarizations is presented in this paper. The presented filter is completely passive and has no dielectric substrates in its configuration. It is mechanically robust, light-weight, optically transparent, and has large upper and lower stopbands with small transition bands. The FSS filter has 31% 3-dB fractional bandwidth centered at 10.36 GHz, which can be tuned without the need of active modules or re-fabrication. The filtering mechanism of the proposed FSS filter has been explained and verified using modal analysis and its associated equivalent circuits. It can be manufactured in large quantities with an extremely low cost by stamping the metallic pattern in a thin metal sheet.

CHAPTER 7

Dielectric-Less Wideband Phase-Correcting Metasurface

7.1 Abstract

This paper presents a novel Substrate-less Near-field Correcting Structure (SNCS) used with a heavily shortened horn antenna to produce plane wave over a large frequency band. The proposed SNCS has mechanically and electromagnetically exceptional properties, never achieved by any near-field manipulators. The SNCS is polarization independent, incredibly low-cost, light-weight and has a large operational frequency bandwidth of 25%. Majority of near-field manipulators are made of either several printed microwave substrates, or low-loss all-dielectric materials, contributing to very high fabrication cost, posing an industrial impediment to their applications. The proposed SNCS is composed of only two freestanding layers of all-metal resonating elements collectively create wideband high transmission with controllable transmission phase without converting the polarization of the electromagnetic waves. The predicted and measured results suggest the horn with the SNCS generates plane wave for a wide frequency band, and has considerably high aperture efficiency of 66%, showing 270% improvement compared to

Under review as: Ali Lalbakhsh, Muhammad U. Afzal, Karu P. Esselle, Stepanie L. Smith, " Substrate-Less Polarization-Independent Structure for Wideband Near-Field Correction," *IEEE Transactions on Antennas and Propagation.*

the bare horn. The measured peak directivity of the antenna system is around 21 dB with a large 3-dB directivity bandwidth of 25%.

7.2 Introduction

There has been an increasing demand of low-cost, light-weight directive antennas for micro- and millimeter wave frequency bands. Traditionally, reflector dishes and arrays of low-gain antennas, such as microstrip antennas are employed in high-gain applications [196]. The former is undesirably large for some applications and the latter needs a complex feeding networks subject to loss. Lately, Resonant-Cavity Antennas (RCAs) have also been investigated for high-gain applications because of their simple feed mechanism and planar configurations [28,42,47,53,130]. However, the conventional RCAs have a non-uniform phase distribution created by the transverse propagation of the cavity feed, which requires near-field modifications to rectify [49, 139].

Traditional horn antennas are attractive candidates, as they do not need expensive RF laminates and do not suffer from dielectric losses. However, the size and the weight of this class of antenna become problematic, especially at lower frequencies, as the gain of the antenna is directly proportional to its physical size [197]. The aperture of horn antennas is increased by keeping a fixed flare angle and increasing the height of the conical section of the horn. For high-gain applications, a horn can be several wavelengths tall and may not be suitable for space-limited practices. The height can be reduced by increasing the flare angle but it deteriorates the phase uniformity on the aperture of the horn, adversely affecting the gain of the antenna.

Dielectric lens was the first response to address this issue, leading to various dielectric lens horn antennas [4, 198–200]. Later on, printed lens was introduced to reduce the size and the weight of the dielectric lens. Therefore, different types of meta-surfaces in the form of Frequency Selective Surfaces (FSSs) or transmit arrays have been used to improve the near-field distribution of horns as well as other aperture antennas, such as RCAs [20, 22, 25, 48, 201, 202]. For example, a double-sided printed FSS composed of non-resonating patch elements have been proposed for phase correction over a limited bandwidth of a pyramidal horn antenna [202]. Wideband

phase-correction of horn antennas, however, have been achieved through more complex configurations [201, 203, 204]. For instance, a metamaterial-based lens composed of several printed layers, including two impedance matching surfaces have recently been proposed in [203], resulting a significant wideband improvement in the aperture efficiency of a sub-loaded horn antenna. In a different approach, resonating patches have been used to develop a wideband transmit array [201].

Nevertheless, all aforementioned structures are composed of either all-dielectric or conductive elements mounted on the expensive microwave dielectric substrates, contributing to very high prototyping cost. Additionally, it may be preferred to avoid employing such substrates in applications with harsh environments, such as space explorations [193].

Very recently a few all-metal phase-shifting structures have been proposed, all of which are polarization dependent and/or operate at a single frequency [34, 194, 195, 205, 206]. For example structures proposed in [34] and [206] have very limited bandwidths and can only support either circularly, or linearly polarized waves. Differently, large operational bandwidths of around 24% and 15% have been achieved in [195] and [194], respectively, where the former is suitable for linear polarization only and the latter achieves the required phase-shift by transforming the polarization of the incoming wave into a cross polar outgoing wave.

Reviewing phase-correcting structures for aperture radiating sources suggests that while considerable near-filed enhancements have been achieved by various types of expensive dielectric-based phase-shifting structures, there is still no fully-metallic passive solution for a wideband near-field correction, which is polarization insensitive. The proposed SNCS is made of only two freestanding layers of resonating elements, whose wideband operational mechanism does not rely on polarization conversion or the polarization of the incoming EM waves. Additionally, the SNCS is low-cost, light-weight and unlike [34] does not require any internal waveguide, so it can be developed using a range of low-cost manufacturing technologies, such as water-jet cutting, laser cutting and 2D stamping for rapid large-scale prototyping.

The rest of the paper is organized as follows: In Section II, a shortened horn antenna with a large apex having a highly non-uniform electric near-field phase distribution is designed. In

Section III, the novel structure of the proposed SNCS along with its electromagnetic and mechanical specifications are presented. Section IV discusses the fabrication and the measurements of the antenna system, and Section V gives a summary of the paper.

7.3 Shortened conical horn antenna with larger apex angle

The physical parameters of a conventional conical horn fed by a waveguide is calculated using (1), (2) and some trigonometric simplifications as discussed in [207].

$$G = \varepsilon_{ap} \frac{4\pi A_p}{\lambda^2} \tag{7.1}$$

$$r = \frac{\sqrt{3l\lambda}}{2} \tag{7.2}$$

where G is the gain, ε_{ap} is the aperture efficiency, λ is the free-space wavelength at the design frequency, A_p is the physical aperture of the antenna. In (2), r and l are the radii and length of the conical horn, respectively.

In order to achieve a peak gain of 21 dB at 11 GHz, the height and radii of the conventional conical horn are calculated to be 192.7 mm and 68.9 mm, respectively. Then, the flare angle is increased from 17.26^o to 32^o and the height reduced to 70.7 mm, resulting an aperture with a radii of 53 mm. The volume of the new *ad hoc* horn is significantly smaller than the initially designed horn, suggesting 4.6 times volume reduction. However, this improvement achieved at a price of a large phase non-uniformity in the antenna aperture, resulting a peak gain of 16.05 dB. This can be seen from 2-D near-field phase distributions at 4 distinct frequencies within the desired large frequency band, as shown in Fig. 7.1. Such undesired spherical wavefronts can be rectified by the proposed SNCS explained in the following section.

,

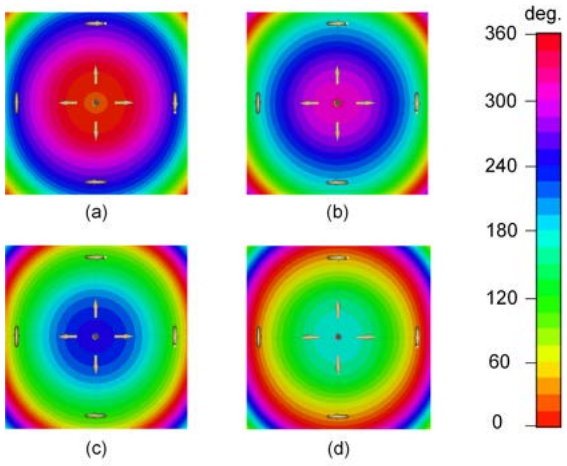

Figure 7.1: 2D phase distribution of the shortened horn antenna on a reference surface at a distance of 15 mm from the aperture. (a) 10.5 GHz, (b) 11.0 GHz, (c) 11.5 GHz,(d) 12.0 GHz.

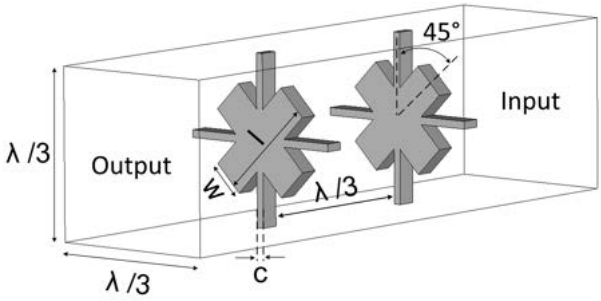

Figure 7.2: A perspective of the proposed fully metallic spatial phase shifter.

7.4 Design of Substrate-less Near-field Correcting Structure (SNCS)

7.4.1 Electromagnetic and Mechanical Specifications of the Unit Cell

Over the last few years, meta-surfaces have made breakthroughs in electromagnetic problems by introducing engineered microwave properties which are not achievable using conventional

antennas and microwave devices [30, 42, 157–160, 182, 189, 208]. There are a number of phase-correcting designs based on printed meta-surfaces, which are bound to use dielectric substrates to support and isolate the conductive patterns on the printed layers [18, 23, 25, 204, 209, 210]. However, the existing knowledge of such meta-surfaces cannot be directly applied on a fully-metallic structure. This problem is more restricting for the wideband applications, due to the intrinsic complexity associated with the broadband EM devices.

Hence, design of the SNCS is not only a pure EM design problem, but mechanical restrictions need to be initially removed by some none-electromagnetically intrusive. Once the unconditional mechanical integrity of the structure is ensured, metallic resonators with any configurations, with or without discontinuity can be incorporated in the structure, which was otherwise not possible.

Fig. 7.2 shows a unit-cell configuration of the proposed metallic spatial phase shifter with a unit-cell size of $\lambda_0/3$ following recommendations in [25, 50]. As shown in Fig. 7.2, each unit cell comprises of two identical metallic layers separated by an air-gap of $\lambda_0/3$. Each layer is composed of two pairs of orthogonal strips with an angle of 45^o from each other, as illustrated in Fig. 7.2. In this topology, the throughout inductive strips are named Static Cross (SC), which is primarily responsible for mechanical integrity of the structure, while the diagonal dipole is called Diagonal Resonator (DR) and designed to be varied in both length and width to generate the required phase shift without upsetting the structure's robustness ensured by the SCs. The thickness of metal layers is chosen to be 1 mm, so that the SNCS can be fabricated using low-cost available technologies, and would not require any extra bonding and protecting mechanism like foam or radome.

To achieve wideband performance of the SNCS, the SCs in the absence of DRs need to have a large passband, covering the desired operation frequency of the SNCS. This can be achieved if the resonance condition is met somewhere in the operating frequency band. In this design, the presence of two inductive strips in SCs and the capacitive effects created by the stacked air-transmission line create a resonance condition which can be tuned at 11 GHz using a parametric analysis, as illustrated in Fig. 7.3. According to this analysis, a transmission pole occurs at 10.8 GHz for the case of $c = 0.4$ mm, and shifts to higher frequencies when c increases. As a result, a

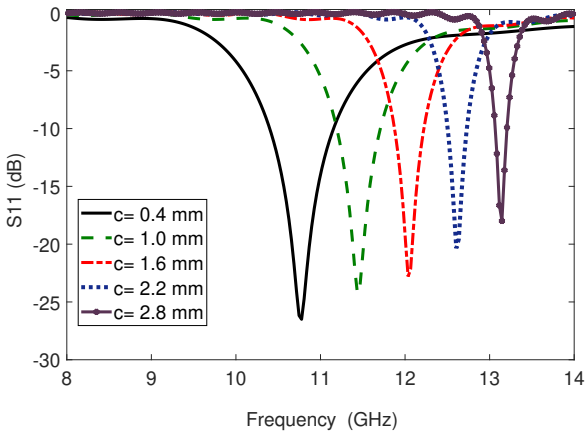

Figure 7.3: The magnitude of the reflection coefficients of the bandpass CSs for different widths.

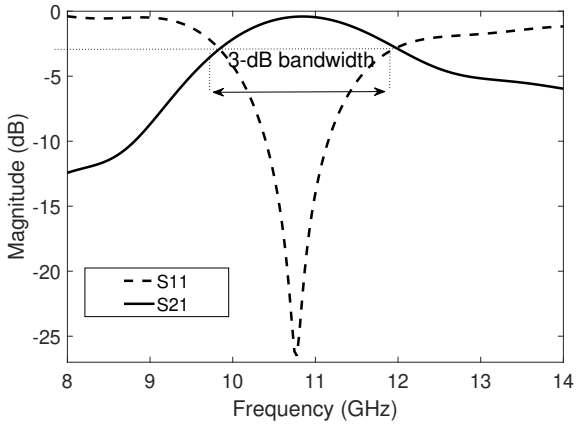

Figure 7.4: Transmission magnitude of the SC (c=0.4 mm).

large 3-dB transmission band with a fractional bandwidth of 21% centered at 11 GHz is realized.

Once the design of the SC is finalized and the mechanical integrity of the structure is ensured, the required phase shifts can be achieved for different dimensions of DRs. The transmission magnitude and phase of each cell were numerically predicted through a parametric study of the unit cell shown in Fig. 7.2, where l and w varied and SC remained unchanged. In this study, l was swept from 0.4 to 3.4 mm with a step size of 0.1 mm, and w varied from 1.0 to 11.4 mm with an interval of 0.4 mm. The minimum, maximum and the step size values in this analysis are determined considering the tolerance limits of the fabrication process and the sensitivity of the parameters. Optimal sizes of l and w can be determined using these surface plots to create

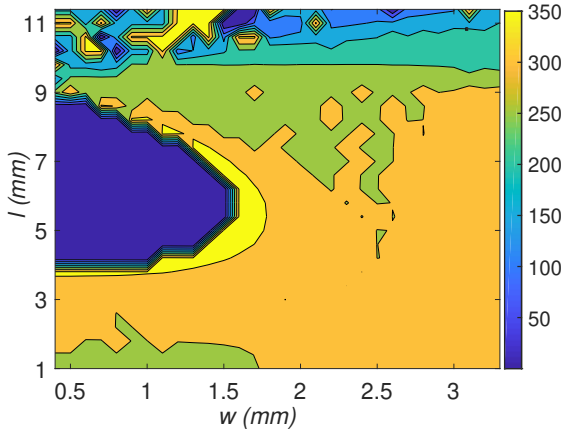

Figure 7.5: Transmission magnitude of various combinations of l and w for a constant c, (c = 0.4 mm) at 11 GHz.

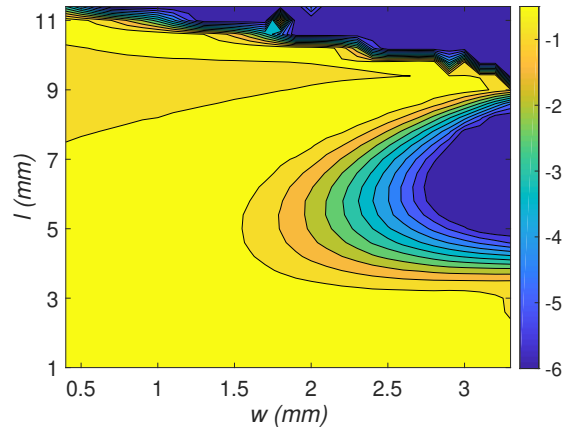

Figure 7.6: Transmission phase of various combinations of l and w for a constant c, (c = 0.4 mm) at 11 GHz.

the required phase shifts with minimum reflection.

7.4.2 Realization of the Wideband SNCS

In order to calculate the local phase shifts required to correct the large aperture phase non-uniformity of the *ad hoc* horn designed in Section II, near-field phase values at 11 GHz were probed on the horn aperture in cylindrical coordinates with $\phi = 0$ and a sampling step-size of $\lambda_0/3$ chosen based on the unit-cell size explained in Section III. A.

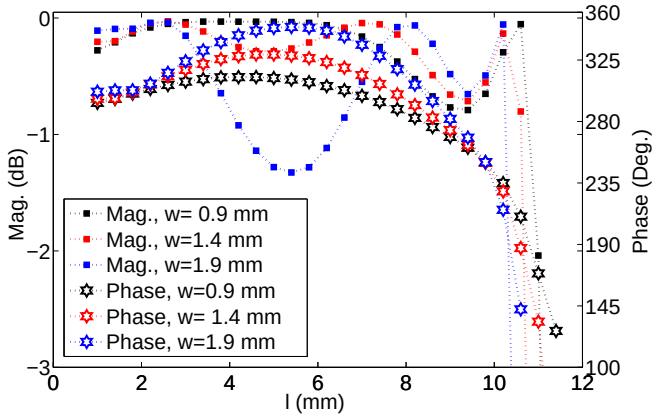

Figure 7.7: Transmission coefficients of the selected unit cells for varying size of DRs at 11 GHz.

Considering the computed phase non-uniformity (will be shown in dotted red line in Fig. 7.11), and the parametric study results shown in surface plots in Fig. 7.5 and Fig. 7.6, it appeared that the DRs with $w = 0.9$ mm and varying length (l) can produce most of the required phase-shift values, as depicted in Fig. 7.7; however, larger values of w can be used for smaller phase delays to complete the required phase range.

In the case of the *ad hoc* horn antenna, 6 transparent phase-correcting cells with the configuration explained in Section III. A are required to be distributed on the antenna's aperture in a circular arrangement proposed in [25, 50]. Such symmetrical manner does not disturb the polarization insensitivity incorporated in the unit-cell configuration and hence the synthesized SNCS remains polarization independent. Table I shows the size and transmission components of the correcting-phase cells used to synthesize the fully metallic SNCS.

7.5 Fabrication, Near- and Far-field Results

7.5.1 Fabrication

In order to fabricate the proposed fully metallic SNCS, firstly the most suitable prototyping procedure needs to be decided based on the constrains of the structure. There are some avail-

Table 7.1: Unit-cell parameters

Cell	w (mm)	l (mm)	$\lvert S_{21}\rvert$ (dB)	$\angle S_{21}$ (Deg.)
1	0.9	10.8	-0.5	190
2	0.9	10.7	-0.15	201
3	0.9	10.4	-0.1	225
4	0.9	9.5	-0.76	259
5	0.9	8.2	-0.50	285
6	1.9	4.2	-0.9	345

able fabrication technologies which can be used for metal prototyping, such as Metal Additive Manufacturing (MAM) [211], plasma cutting [212], Abrasive Waterjet Cutting (AWC) [155] and laser cutting [213], amongst which the first two methods cannot be used for such configurations. Indeed, there is a destructive influence on the confluence, due to the very high temperature used in plasma cutting. Hence this technique is not recommended for the proposed structure, as the perforation areas in the meta-surface greatly exceed the untouched areas, which are highly subjected to breakdown. The MAM, however, is capable to precisely 3D-print objects composed of delicate patterns only if the printing object is supported by a robust base which is not the case with our meta-surface, due to its small metal thickness (1 mm). Either laser cutting or AWC can be employed to perforate a metal sheet and remove polygonal patterns to realize the proposed meta-surface. Nevertheless, laser cutting can be subject to thermal deformation and burr formation when used in a small area. So, a 0.5 Mpsi waterjet cutting machine with garnet abrasive powder was used for this purpose. Fig. 7.8 shows one layer of the SNCS made of Aluminum.

The SNCS can also be developed by stamping patterns on a thin standard metallic sheet, which can be used for large-scale manufacturing.

Two layers of perforated Aluminum sheets were fabricated and separated by 4 nylon spacers with a hight of 10 mm to realize the wideband SNCS. The *ad hoc* horn antenna designed in Section II was 3D printed using Original Prusa i3 MK3 3D printer with its maximum infill percentage, and a bed temperature of 110 C. The *ad hoc* horn antenna was made of polylactic acid (PLA) filament with a minimum layer thickness and a resolution of 0.1 mm and 0.01 mm, respectively, which was then metalized by the copper film. It was finally integrated with the fabricated meta-surface to realize the wideband plane-wave horn antenna, as shown in Fig. 7.9. The horn antenna is fed by a rectangular slot antenna with dimensions of 15.2 mm$\times$ 8.2 mm.

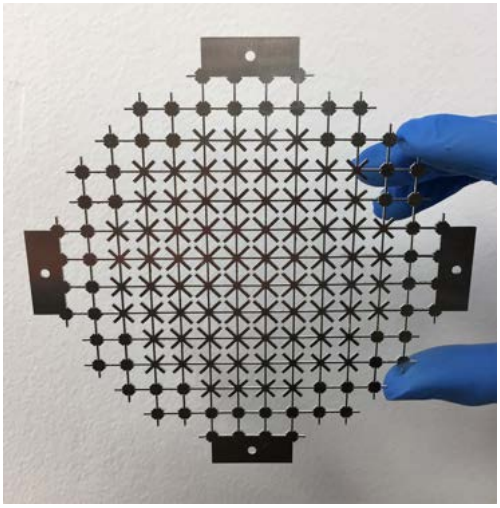

Figure 7.8: One layer of the SNCS fabricated using waterjet cutting with abrasive garnet powder.

7.5.2 Near- and Far-field Results

The input reflection coefficients of the bare shortened horn antenna as well as the antenna under SNCS loading were measured using an Agilent PNA-X N5242A vector network analyzer. As shown in Fig. 7.10, the measured 10-dB $|S11|$ bandwidth is 23% with a center frequency of 10.94 GHz. It should be noted that the SNCS disturb the impedance matching outside the operational

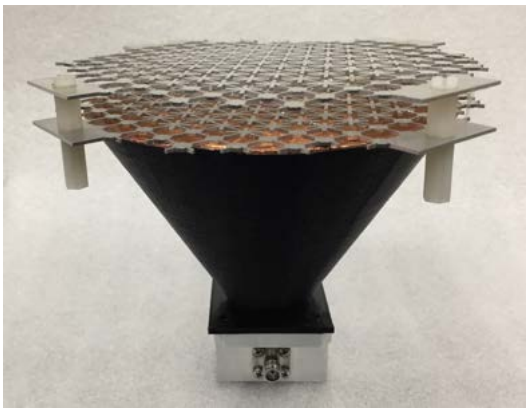

Figure 7.9: Fabricated SNCS placed on the shortened horn antenna. The two concentric layers of the SNCS is separated by 4 nylon spacers.

frequency band, and hence does not negatively impact the overall bandwidth of the antenna system.

The predicted near-field results of the plane-wave horn antenna verify a significant improvement in the electric phase distribution throughout a large frequency band, depicted by 1D and 2D plots in Fig. 7.11 and Fig. 7.12, respectively. This near-field correction achieved by the SNCS has considerably increased the aperture efficiency of the antenna system to 66%, which is 2.7 times grater than that of the bare horn antenna.

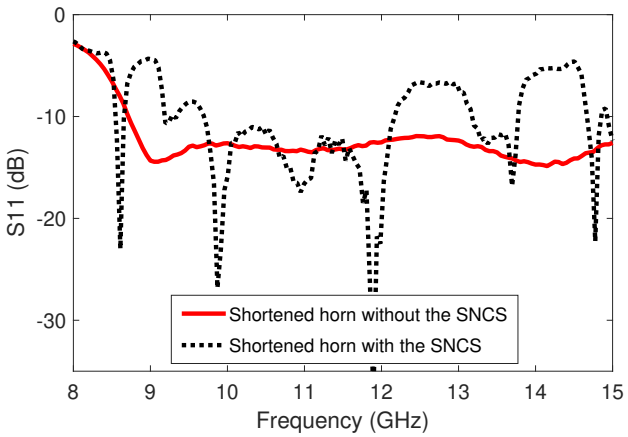

Figure 7.10: Input reflection coefficients of the shortened horn antenna with and without SNCS.

In addition to the near-field results, the wideband performance of the SNCS can be verified

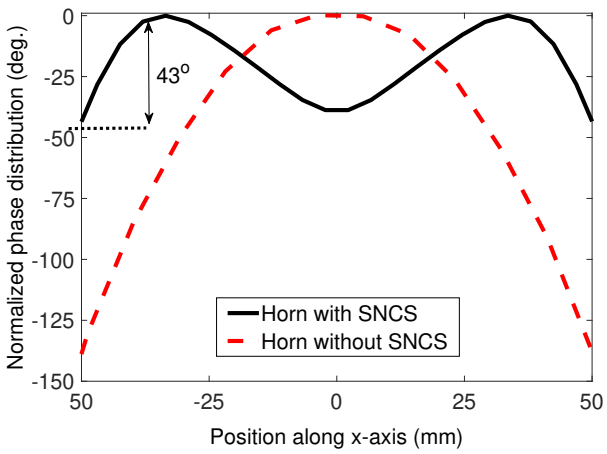

Figure 7.11: Aperture phase distribution of the shortened horn antenna before and after placing SNCS. The phase is measured at a distance of 7 mm from the antenna.

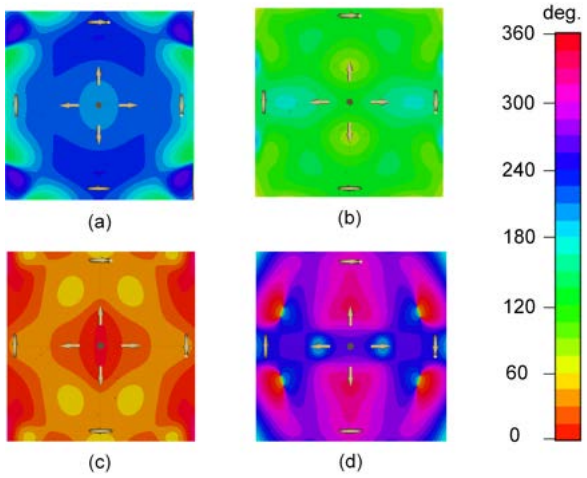

Figure 7.12: 2D phase distribution of the plane-wave horn antenna on a reference surface at a distance of 15 mm from the aperture.

through the enhanced far-field results. The plane-wave horn antenna has a measured peak directivity of 20.9 dB with a large 3-dB directivity bandwidth of 25%, extending from 9.70 GHz to 12.45 GHz. The measured peak gain and its corresponding 3-dB bandwidth of the antenna system are 20.46 dB and 23%, which is slightly smaller than the directivity bandwidth. The gain and directivity of the plane-wave horn antenna versus frequency are plotted in Fig. 7.13, showing very good agreement between the predicted results by CST MWS and the measured

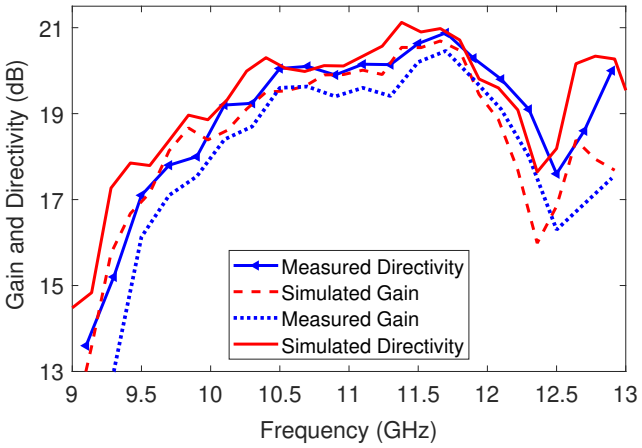

Figure 7.13: Gain and directivity of the shortened horn antenna with the fully metallic metasurface.

ones in NSI-700s-50 spherical near-field range. The radiation patterns of the antenna under the SNCS loading at 6 distinct frequencies (10.3, 10.7, 11.1, 11.5, 11.9 and 12.3 GHz) are plotted in Fig. 7.14, exhibiting very stable sidelobe levels (SLLs) all over the large operating frequency band. As can be seen from Fig. 7.14, SLLs in the H and E-planes are better than -20 dB and -12 dB, respectively, throughout the bandwidth. The weight of the fabricated SNCS composed of two perforated aluminum sheets is only 30 g.

7.6 Conclusion

A wideband Substrate-less Near-field Correcting Structure (SNCS) with a completely passive and symmetrical configuration is presented in this paper. The proposed SNCS is composed of two layers of aluminum sheets perforated to realize several arrays of metallic resonators, which are responsible to produce a wideband transmission window with a controllable transmission phase. Unlike all other all-metal phase manipulators, the wideband phase-shifting mechanism of the SNCS is neither based on polarization conversion, nor sensitive to incoming waves' polarization. The proposed SNCS was fabricated using waterjet cutting machine with abrasive garnet powder to facilitate the perforation of the metal sheets. To test the performance of the SNCS,

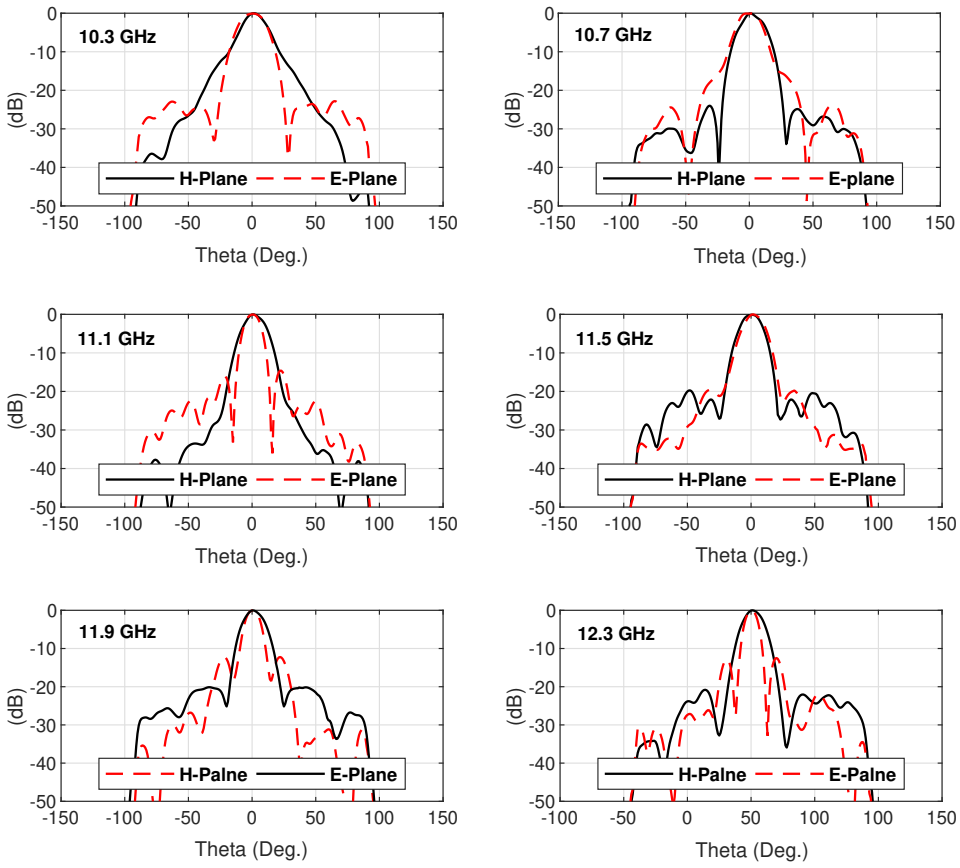

Figure 7.14: Measured radiation patterns of the horn antenna with SNCS at 6 equally spaced frequencies throughout the bandwidth.

a shortened horn antenna with a highly nonuniform near-field phase distribution was used as an electromagnetic source for the SNCS. According to the predicted and measured results, the SNCS has greatly improved the near-field phase distribution of the shortened horn antenna, resulting in a very high aperture efficiency of 66%, corresponding to a peak gain of 20.46 dB. The large operational bandwidth of the SNCS was also verified through the measured large 3-dB gain bandwidth of 23% achieved for the plane-wave horn antenna. The proposed design technology opens a new door in meta-surfaces design and their applications, as RF laminates which are the greatest contributor of high manufacturing cost has completely been made redundant without imposing any limitations in terms of electromagnetic behavior, mechanical robustness and ease

of fabrication, while an excellent wideband performance has been achieved.

CHAPTER 8

Conclusions and Future Work

8.1 Summary and Findings

In this thesis, multiple new practical procedures are proposed for altering electric near-fields of high-gain antennas for different applications, such as phase correction, magnitude correction, Partially Reflecting Surface (PRS), and beamsteering. It has been demonstrated that some critical EM limitations originated from the nature of materials can be removed through a systematic design approach, opening a new door in relation to both manufacturing and applications of metasurfaces. The thesis in particular presents design methodologies for all-dielectric metasurfaces, printed metasurfaces and finally dielectric-less metasurfaces.

To demonstrate the proposed design procedures, six major designs have been reported in this thesis corresponding to six major chapters (Chapter 2 to Chapter 7). The thesis begins with a new design methodology to control both magnitude and phase of the electric near-field of a Resonant Cavity Antenna (RCA) over a large bandwidth of 40%. In this approach, a customized Particle Swarm Optimization algorithm is implemented in MATLAB to communicate with CST Microwave Studio through a Visual Basic Application (VBA) channel to optimize a pre-configured design named Near-Field Correcting Structure (NFCS). The NFCS was fabricated and tested with the RCA, showing an excellent performance of phase and magnitude correction, resulting a significant increase in the peak directivity of the antenna, reaching 21 dB with very good sidelobe levels.

Another all-dielectric structure has been developed for steering the beam of high-gain antennas through a passive mechanism. The steerable high-gain antenna system is composed of a RCA, one stationary radially graded-dielectric metasurface and two rotating linearly graded-dielectric metasurfaces. In this approach, the stationary metasurface is responsible to rectify the non-uniform phase distribution of the RCA, while the two rotating metaurfaces collectively scan the beam to any direction within a cone having an apex angle of 82.2°. The aperture of the antenna system is $6\lambda_0$ and its height is only $2.2\lambda_0$, where λ_0 is defined at the operating frequency of 11 GHz. The peak directivity of the antenna system is 21 dB at 11 GHz.

Apart from all-dielectric configurations outlined above, a printed metasurface has been designed to be used as a PRS to develop a wideband RCA with excellent characteristics. The metasurface is composed of arrays of resonating elements printed on both sides of a single dielectric slab to create two phenomena, which have never been used simultaneously. The non-uniform PRS exhibits different reflection magnitudes on the aperture, creating a negative transverse reflection magnitude gradient and at the same time a progressive reflection phase gradient over frequency. The combination of these two features results in a compact wideband PRS without sacrificing ease of fabrication and gain. The PRS has been fabricated and tested, producing a peak gain of 15.75 dB at 11.4 GHz with a 3-dB gain bandwidth of 21.5%. The PRS is compact, light, with a thickness and area of $0.12\lambda_g$ and $3.8\lambda_0^2$, respectively.

All above-mentioned metasurfaces are realized using microwave dielectric substrates, which contributes to a high manufacturing cost. Additionally, they are all prone to dielectric breakdown at high power. To address these issues, three novel dielectric-less metasurfaces are proposed for a variety of applications. An All-Metal Phase Correcting Structure (AMPCS) has been designed to significantly improve the radiation patterns of a RCA through correcting the electric near-field of the antenna. The AMPCS is composed of three layers of perforated thin stainless steel with a distance of around $\lambda_0/3$ from each other. The AMPCS is suitable for both polarization, as it has four-fold symmetry. It was fabricated using laser technology and tested with the RCA, showing 8.4 dB improvement in the peak gain of the antenna, reaching to a peak gain of 19.42 dB. In spite of the excellent performance of the AMPCS, it has a narrow operational frequency

band. Therefore, in the next step a new design methodology is presented to achieve wideband performance of all-metal metasurfaces. In this procedure, a metallic inductive lattice is designed to provide a large bandpass response, and suppresses the second-harmonic band. Additional resonators are then integrated into the lattice to finely tailor the frequency response of the wideband metasurface filter.

Following this method, another all-metal metasurface composed of several phase shifting units is designed to rectify the highly non-uniform near-field of a shortened horn antenna, resulting in a small horn capable of generating plane wave. The measured results of the horn antenna with the metasurface show a high aperture efficiency of 66%. The antenna system has a peak directivity of around 21 dB with a large 3-dB directivity bandwidth of 25%. The measured sidelobe levels in the H and E-planes are better than -20 dB and -12 dB, respectively, throughout the operating frequency band.

8.2 Future Work

This thesis opens up number of possibilities for further exploration which may include the following.

All-Metal Beamsteering System: the presented design methodology for the all-metal metasurfaces can be adopted to develop all-metal beamsteering metsurfaces with a large operational bandwidth. For this purpose, an arrangement of metallic phase shifting units with high transmission magnitude can be used to realize a linearly progressive phase delay throughout the aperture of the base antenna. The consistency of such all-metal metasurface is ensured by the metallic inductive lattice.

Further Optimisations: evolutionary optimization techniques such as ant colony, neural network, genetic algorithm, and particle swarm optimization can be customized for global optimization of the all-metal metasurfaces presented in this thesis.

Multi-Band Spatial Metasurfaces Filter: design of multi-band spatial metasurfaces filters can be investigated using the presented design procedure of the wideband metasurface

filter. This can be possible by generating multiple resonances in the frequency response of the metasurface filter by tuning metallic Orthogonal Dipole Resonator.

Higher Gain Applications: the presented beamsteering metasurfaces can be used with some other high-gain antennas, such as radial line slot array antenna or arrays to achieve more directive steering radiations.

F and V-band applications: extension of the presented near-field correcting structure (NFCS) at millimeter wave frequencies can be investigated for applications in F-band (90 GHz-140 GHz) and V-band (50 GHz-75 GHz). Considering the large frequency band of NFCS, it can be used with some high-gain antennas to cover the whole band and act as switched-beam high-gain antenna systems for automotive radar applications, terrestrial communications. Such high-gain antenna can also be used as reflector feeds for radio astronomical radio-telescopes.

Flexible Metasurfaces: an investigation can be done into the application of flexible materials [52, 214, 215] in construction of non-rigid electromagnetic metasurfaces with potential applications in wireless body area networks [216].

Bibliography

[1] H. F. Ma, X. Chen, X. M. Yang, W. X. Jiang, and T. J. Cui, "Design of multibeam scanning antennas with high gains and low sidelobes using gradient-index metamaterials," *Journal of Applied Physics*, vol. 107, no. 1, p. 014902, 2010.

[2] X. Zhou, X. Zou, Y. Yang, H. Ma, and T. Cui, "Three-dimensional large-aperture lens antennas with gradient refractive index," *Science China Information Sciences*, vol. 56, no. 12, pp. 1–12, 2013.

[3] Z. Tao, W. X. Jiang, H. F. Ma, and T. J. Cui, "High-gain and high-efficiency grin metamaterial lens antenna with uniform amplitude and phase distributions on aperture," *IEEE Transactions on Antennas and Propagation*, vol. 66, no. 1, pp. 16–22, 2017.

[4] M. K. T. Al-Nuaimi, W. Hong, and Y. Zhang, "Design of high-directivity compact-size conical horn lens antenna," *IEEE Antennas Wireless Propag. Lett.*, vol. 13, pp. 467–470, 2014.

[5] P. Nayeri, M. Liang, R. A. Sabory-Garcı, M. Tuo, F. Yang, M. Gehm, H. Xin, A. Z. Elsherbeni *et al.*, "3d printed dielectric reflectarrays: low-cost high-gain antennas at submillimeter waves," *IEEE Transactions on Antennas and Propagation*, vol. 62, no. 4, pp. 2000–2008, 2014.

[6] R. M. Hashmi and K. P. Esselle, "A class of extremely wideband resonant cavity antennas with large directivity-bandwidth products," *IEEE Trans. Antennas Propag.*, vol. 64, no. 2, pp. 830–835, 2016.

[7] K. Konstantinidis, A. P. Feresidis, and P. S. Hall, "Multilayer partially reflective surfaces for broadband fabry-perot cavity antennas," *IEEE Transactions on Antennas and Propagation*, vol. 62, no. 7, pp. 3474–3481, 2014.

[8] ——, "Broadband sub-wavelength profile high-gain antennas based on multi-layer metasurfaces," *IEEE Transactions on Antennas and Propagation*, vol. 63, no. 1, pp. 423–427, 2015.

[9] A. Feresidis and J. Vardaxoglou, "A broadband high-gain resonant cavity antenna with single feed," in *Antennas and Propagation, 2006. EuCAP 2006. First European Conference on.* IEEE, 2006, pp. 1–5.

[10] H. Attia, M. L. Abdelghani, and T. A. Denidni, "Wideband and High-Gain Millimeter-Wave Antenna Based on FSS Fabry–Perot Cavity," *IEEE Trans. Antennas Propag.*, vol. 65, no. 10, pp. 5589–5594, 2017.

[11] Y. Ge, K. P. Esselle, and T. S. Bird, "The use of simple thin partially reflective surfaces with positive reflection phase gradients to design wideband, low-profile ebg resonator antennas," *IEEE Trans. Antennas Propag.*, vol. 60, no. 2, pp. 743–750, 2012.

[12] L. Moustafa and B. Jecko, "Ebg structure with wide defect band for broadband cavity antenna applications," *IEEE Antennas Wireless Propag. Lett.*, vol. 7, pp. 693–696, 2008.

[13] M. A. Al-Joumayly and N. Behdad, "A generalized method for synthesizing low-profile, band-pass frequency selective surfaces with non-resonant constituting elements," *IEEE Transactions on Antennas and Propagation*, vol. 58, no. 12, pp. 4033–4041, 2010.

[14] M. Al-Joumayly and N. Behdad, "Wideband planar microwave lenses using sub-wavelength spatial phase shifters," *IEEE Trans. Antennas Propag*, vol. 59, no. 12, pp. 4542–4552, 2011.

[15] ——, "A new technique for design of low-profile, second-order, bandpass frequency selective surfaces," *IEEE Trans. Antennas Propag.*, vol. 57, no. 2, pp. 1239–1245, 2009.

[16] K. Sarabandi and N. Behdad, "A frequency selective surface with miniaturized elements," *IEEE Trans. Antennas Propag.*, vol. 55, no. 5, pp. 1239–1245, 2007.

[17] K. K. Katare, A. Biswas, and J. Akhtar, "Wideband beam-steerable configuration of metasurface loaded slot antenna," *International Journal of RF and Microwave Computer-Aided Engineering*, p. e21408, 2018.

[18] K. K. Katare, A. Biswas, and M. J. Akhtar, "Microwave beam steering of planar antennas by hybrid phase gradient metasurface structure under spherical wave illumination," *Journal of Applied Physics*, vol. 122, no. 23, p. 234901, 2017.

[19] Y. Xu, Z. Guo, and G. Yang, "Honeycombed metasurface plate for generation of x-band orbital angular momentum beam," *Microwave and Optical Technology Letters*, vol. 61, no. 10, pp. 2392–2398, 2019.

[20] K. Dutta, D. Guha, and C. Kumar, "Synthesizing aperture fields over the superstrate of resonance cavity antenna for modifying its radiation properties," *IEEE Antennas and Wireless Propagation Letters*, vol. 15, pp. 1677–1680, 2016.

[21] M. U. Afzal and K. P. Esselle, "A low-profile printed planar phase correcting surface to improve directive radiation characteristics of electromagnetic band gap resonator antennas," *IEEE Trans. Antennas Propag.*, vol. 64, no. 1, pp. 276–280, 2016.

[22] L. Zhou, X. Chen, X. Duan, and J. Li, "Fabry-perot antenna using a three-layer phase shifting structure for gain enhancement," *IET Microwaves, Antennas & Propagation*, vol. 12, no. 3, pp. 400–405, 2017.

[23] M. A. Al-Joumayly and N. Behdad, "Wideband planar microwave lenses using subwavelength spatial phase shifters," *IEEE Transactions on Antennas and Propagation*, vol. 59, no. 12, pp. 4542–4552, 2011.

[24] S. M. A. M. H. Abadi, M. Li, and N. Behdad, "Harmonic-suppressed miniaturized-element frequency selective surfaces with higher order bandpass responses," *IEEE Transactions on Antennas and Propagation*, vol. 62, no. 5, pp. 2562–2571, 2014.

[25] A. Lalbakhsh, M. U. Afzal, and K. P. Esselle, "Multi-objective particle swarm optimization to design a time delay equalizer metasurface for an electromagnetic band gap resonator antenna," *IEEE Antennas Wireless Propag. Lett.*, vol. 16, pp. 912–915, 2017.

[26] R. Karimian, A. Kesavan, M. Nedil, and T. A. Denidni, "Low-mutual-coupling 60-ghz mimo antenna system with frequency selective surface wall," *IEEE Antennas and Wireless Propagation Letters*, vol. 16, pp. 373–376, 2017.

[27] M. M. Tahseen and A. A. Kishk, "Flexible and portable textile-reflectarray backed by frequency selective surface," *IEEE Antennas and Wireless Propagation Letters*, vol. 17, no. 1, pp. 46–49, 2018.

[28] A. Lalbakhsh, M. U. Afzal, K. P. Esselle, , S. L. Smith, and B. A. Zeb, "Single-dielectric wideband partially reflecting surface with variable reflection components for realization of a compact high-gain resonant cavity antenna," *IEEE Transactions on Antennas and Propagation*, vol. 76, no. 3, pp. 1916 – 1921, 2019.

[29] M. Li and N. Behdad, "A third-order bandpass frequency selective surface with a tunable transmission null," *IEEE Transactions on Antennas and Propagation*, vol. 60, no. 4, pp. 2109–2113, 2012.

[30] D. Li, Z. Shen, and E.-P. Li, "Spurious-free dual-band bandpass frequency-selective surfaces with large band ratio," *IEEE Transactions on Antennas and Propagation*, vol. 67, no. 2, pp. 1065–1072, 2019.

[31] A. A. Omar and Z. Shen, "Thin 3-d bandpass frequency-selective structure based on folded substrate for conformal radome applications," *IEEE Transactions on Antennas and Propagation*, vol. 67, no. 1, pp. 282–290, 2019.

[32] J. Benford, J. A. Swegle, and E. Schamiloglu, *High power microwaves*. CRC press, 2007.

[33] X.-Q. Li, Q.-X. Liu, X.-J. Wu, L. Zhao, J.-Q. Zhang, and Z.-Q. Zhang, "A gw level high-power radial line helical array antenna," *IEEE Transactions on Antennas and Propagation*, vol. 56, no. 9, pp. 2943–2948, 2008.

[34] X. Zhao, C. Yuan, L. Liu, S. Peng, Q. Zhang, and H. Zhou, "All-metal transmit-array for circular polarization design using rotated cross-slot elements for high-power microwave applications," *IEEE Transactions on Antennas and Propagation*, vol. 65, no. 6, pp. 3253–3256, 2017.

[35] X. Zhao, C. Yuan, L. Liu, S. Peng, Q. Zhang, L. Yu, and Y. Sun, "All-metal beam steering lens antenna for high power microwave applications," *IEEE Transactions on Antennas and Propagation*, vol. 65, no. 12, pp. 7340–7344, 2017.

[36] R. Y. Wu, Y. B. Li, W. Wu, C. B. Shi, and T. J. Cui, "High-gain dual-band transmitarray," *IEEE Transactions on Antennas and Propagation*, vol. 65, no. 7, pp. 3481–3488, 2017.

[37] B. Rahmati and H. Hassani, "High-efficient wideband slot transmitarray antenna," *IEEE Transactions on Antennas and Propagation*, vol. 63, no. 11, pp. 5149–5155, 2015.

[38] C. Cheype, C. Serier, M. Thèvenot, T. Monédière, A. Reineix, and B. Jecko, "An electromagnetic bandgap resonator antenna," *IEEE Trans. Antennas Propag.*, vol. 50, no. 9, pp. 1285–1290, 2002.

[39] L. Leger, R. Granger, M. Thevenot, T. Monediere, and B. Jecko, "Multifrequency dielectric ebg antenna," *Microwave and Optical Technology Letters*, vol. 40, no. 5, pp. 420–423, 2004.

[40] D. Jackson, A. Oliner, and A. Ip, "Leaky-wave propagation and radiation for a narrow-beam multiple-layer dielectric structure," *IEEE Trans. Antennas Propag.*, vol. 41, no. 3, pp. 344–348, 1993.

[41] Y. Ge, Z. Sun, Z. Chen, and Y.-Y. Chen, "A high-gain wideband low-profile Fabry-Perot resonator antenna with a conical short horn," *IEEE Antennas Wireless Propag. Lett.*, vol. 15, pp. 1889–1892, 2016.

[42] M. Akbari, S. Gupta, M. Farahani, A. Sebak, and T. Denidni, "Gain enhancement of circularly polarized dielectric resonator antenna based on fss superstrate for mmw applications," *IEEE Trans. Antennas Propag.*, vol. 64, no. 12, pp. 5542–5546, 2016.

[43] Y. Zheng, J. Gao, Y. Zhou, X. Cao, H. Yang, S. Li, and T. Li, "Wideband gain enhancement and rcs reduction of fabry–perot resonator antenna with chessboard arranged metamaterial superstrate," *IEEE Trans. Antennas Propag.*, vol. 66, no. 2, pp. 590–599, 2018.

[44] Z.-G. Liu and W.-B. Lu, "Low-profile design of broadband high gain circularly polarized fabry-perot resonator antenna and its array with linearly polarized feed," *IEEE Access*, vol. 5, pp. 7164–7172, 2017.

[45] W. Cao, W. Hong, Z. N. Chen, B. Zhang, and A. Liu, "Gain enhancement of beam scanning substrate integrated waveguide slot array antennas using a phase-correcting grating cover," *IEEE Trans. Antennas Propag.*, vol. 62, no. 9, pp. 4584–4591, 2014.

[46] G. V. Trentini, "Partially reflecting sheet arrays," *IRE Trans. Antennas and Propag.*, vol. 4, no. 4, pp. 666–671, 1956.

[47] K. Dutta, D. Guha, C. Kumar, and Y. M. Antar, "New approach in designing resonance cavity high-gain antenna using nontransparent conducting sheet as the superstrate," *IEEE Trans. Antennas Propag.*, vol. 63, no. 6, pp. 2807–2813, 2015.

[48] K. Dutta, D. Guha, and C. Kumar, "Theory of controlled aperture field for advanced superstrate design of a resonance cavity antenna with improved radiations properties," *IEEE Transactions on Antennas and Propagation*, vol. 65, no. 3, pp. 1399–1403, 2017.

[49] M. U. Afzal, K. P. Esselle, and B. A. Zeb, "Dielectric phase-correcting structures for electromagnetic band gap resonator antennas," *IEEE Trans. Antennas Propag.*, vol. 63, no. 8, pp. 3390–3399, 2015.

[50] M. U. Afzal, K. P. Esselle, and A. Lalbakhsh, "A methodology to design a low-profile composite-dielectric phase-correcting structure," *IEEE Antennas Wireless Propag. Lett.*, vol. 17, no. 7, pp. 1223–1227, 2018.

[51] M. U. Afzal, A. Lalbakhsh, and K. P. Esselle, "Electromagnetic-wave beam-scanning antenna using near-field rotatable graded-dielectric plates," *Journal of Applied Physics*, vol. 124, no. 23, p. 234901, 2018.

[52] B. Mohamadzade, R. B. Simorangkir, R. M. Hashmi, and A. Lalbakhsh, "A conformal ultra-wideband antenna with monopole-like radiation pattern," *IEEE Trans. Antennas Propag.*, vol. 68, 2020.

[53] M. Akbari, H. A. Ghalyon, M. Farahani, A.-R. Sebak, and T. A. Denidni, "Spatially decoupling of CP antennas based on FSS for 30-GHz MIMO systems," *IEEE Access*, vol. 5, pp. 6527–6537, 2017.

[54] J. Kennedy and R. C. Eberhart, "Particle swarm optimisation," in *Proc. Int. Conf. Neural Networks*, vol. IV, 1995, pp. 1942–1948.

[55] J. Robinson and Y. Rahmat-Samii, "Particle swarm optimization in electromagnetics," *IEEE Trans. Antennas Propag.*, vol. 52, no. 2, pp. 397–407, 2004.

[56] A. Lalbakhsh, M. Afzal, K. Esselle, and S. Smith, "A fast design procedure for quadrature reflection phase," in *2017 Progress in Electromagnetics Research Symposium-Fall (PIERS-FALL)*. IEEE, 2017, pp. 2364–2366.

[57] C. Jarufe, R. Rodriguez, V. Tapia, P. Astudillo, D. Monasterio, R. Molina, F. Mena, N. Reyes, and L. Bronfman, "Optimized corrugated tapered slot antenna for mm-wave

applications," *IEEE Transactions on Antennas and Propagation*, vol. 66, no. 3, pp. 1227–1235, 2018.

[58] A. Lalbakhsh *et al.*, "Particle swarm optimization for performance enhancement of electromagnetic band gap resonator antennas," 2015.

[59] Z. D. Zaharis, I. P. Gravas, P. I. Lazaridis, I. A. Glover, C. S. Antonopoulos, and T. D. Xenos, "Optimal lte-protected lpda design for dvb-t reception using particle swarm optimization with velocity mutation," *IEEE Transactions on Antennas and Propagation*, 2018.

[60] A. Lalbakhsh, M. U. Afzal, B. A. Zeb, and K. P. Esselle, "Design of a dielectric phase-correcting structure for an ebg resonator antenna using particle swarm optimization," in *Proc. Int. Symp. Antennas Propag., Hobart, Australia*, 2015.

[61] A. Dadgarpour, G. Dadashzadeh, M. Naser-Moghadasi, F. Jolani, and B. S. Virdee, "PSO/FDTD optimization technique for designing UWB in-phase power divider for linear array antenna application," *IEEE Antennas and Wireless Propagation Letters*, vol. 9, pp. 424–427, 2010.

[62] A. Lalbakhsh, M. U. Afzal, K. P. Esselle, and B. A. Zeb, "Multi-objective particle swarm optimization for the realization of a low profile bandpass frequency selective surface," in *Proc. Int. Symp. Antennas Propag. (ISAP)*, 2015, pp. 1–4.

[63] N. Jin and Y. Rahmat-Samii, "Advances in particle swarm optimization for antenna designs: Real-number, binary, single-objective and multiobjective implementations," *IEEE Trans. Antennas Propag.*, vol. 55, no. 3, pp. 556–567, 2007.

[64] A. Lalbakhsh, M. U. Afzal, K. P. Esselle, and S. Smith, "Design of an artificial magnetic conductor surface using an evolutionary algorithm," in *Proc. Int. Conf. Electromagnetics in Advanced Applications (ICEAA)*, 2017, pp. 885–887.

[65] M. B. Jamshidi, N. Alibeigi, N. Rabbani, B. Oryani, and A. Lalbakhsh, "Artificial neural networks: a powerful tool for cognitive science," in *2018 IEEE 9th Annual Information*

Technology, Electronics and Mobile Communication Conference (IEMCON). IEEE, 2018, pp. 674–679.

[66] M. B. Jamshidi, A. Lalbakhsh, B. Mohamadzade, H. Siahkamari, and S. M. H. Mousavi, "A novel neural-based approach for design of microstrip filters," *AEU-International Journal of Electronics and Communications*, vol. 110, p. 152847, 2019.

[67] P. Lalbakhsh, B. Zaeri, and A. Lalbakhsh, "An improved model of ant colony optimization using a novel pheromone update strategy," *IEICE Trans. Inf. & Syst.*, vol. E96-D, no. 11, pp. 2309–2318, 2013.

[68] M. B. Jamshidi, M. Gorjiankhanzad, A. Lalbakhsh, and S. Roshani, "A novel multiobjective approach for detecting money laundering with a neuro-fuzzy technique," in *2019 IEEE 16th International Conference on Networking, Sensing and Control (ICNSC)*. IEEE, 2019, pp. 454–458.

[69] M. B. Jamshidi, N. Alibeigi, A. Lalbakhsh, and S. Roshani, "An anfis approach to modeling a small satellite power source of nasa," in *2019 IEEE 16th International Conference on Networking, Sensing and Control (ICNSC)*. IEEE, 2019, pp. 459–464.

[70] M. Jamshidi, A. Lalbakhsh, S. Lotfi, H. Siahkamari, B. Mohamadzade, and J. Jalilian, "A neuro-based approach to designing a wilkinson power divider," *International Journal of RF and Microwave Computer-Aided Engineering*, p. e22091, 2019.

[71] P. Lalbakhsh, B. Zaeri, A. Lalbakhsh, and M. N. Fesharaki, "Antnet with reward-penalty reinforcement learning," in *2010 2nd International Conference on Computational Intelligence, Communication Systems and Networks*. IEEE, 2010, pp. 17–21.

[72] M. B. Jamshidi, A. Lalbakhsh, N. Alibeigi, M. R. Soheyli, B. Oryani, and N. Rabbani, "Socialization of industrial robots: an innovative solution to improve productivity," in *2018 IEEE 9th Annual Information Technology, Electronics and Mobile Communication Conference (IEMCON)*. IEEE, 2018, pp. 832–837.

[73] S. Koziel and A. Bekasiewicz, "Comprehensive comparison of compact uwb antenna performance by means of multiobjective optimization," *IEEE Trans. Antennas Propag.*, vol. 65, no. 7, pp. 3427–3436, 2017.

[74] S. Koziel, C. I. Bekasiewicz, A., and T. Dhaene, "Efficient multi-objective simulation-driven antenna design using co-kriging," *IEEE Trans. Antennas Propag.*, vol. 62, no. 11, pp. 5900–5905, 2014.

[75] A. Lalbakhsh and K. P. Esselle, "Directivity improvement of a fabry-perot cavity antenna by enhancing near field characteristic," in *2016 17th International Symposium on Antenna Technology and Applied Electromagnetics (ANTEM)*. IEEE, 2016, pp. 1–2.

[76] A. Lalbakhsh, M. U. Afzal, and K. P. Esselle, "Simulation-driven particle swarm optimization of spatial phase shifters," in *Proc. Int. Conf. Electromagnetics in Advanced Applications (ICEAA),*, 2016, pp. 428–430.

[77] A. B. Constantine *et al.*, "Antenna theory: analysis and design," *MICROSTRIP ANTENNAS, third edition, John wiley & sons*, 2005.

[78] K. W. Linnes, W. D. Merrick, and R. Stevens, "Ground antenna for space communication system," *IRE Trans. on Space Electronics Telemetry*, vol. SET-6, no. 1, pp. 45–54, March 1960.

[79] B. Mohamadzade, R. B. Simorangkir, R. M. Hashmi, R. Gharaei, and A. Lalbakhsh, "Monopole-like and semi-directional reconfigurable pattern antenna for wireless body area network applications," *Microwave and Optical Technology Letters*, vol. 61, no. 12, pp. 2760–2765, 2019.

[80] P. R. Gooran, G. Karimi, and A. Lalbakhsh, "A novel miniaturized log-periodic dipole array antenna using dynamic scaling factor for rfid application," *International Journal of Microwave and Wireless Technologies*, vol. 10, no. 3, p. 345, 2018.

[81] P. Rostami Gooran, A. Lalbakhsh, H. Moradi, and M. Jamshidi, "Compact and wideband printed log-periodic dipole array antenna using multi-sigma and multi-tau techniques," *Journal of Electromagnetic Waves and Applications*, vol. 33, no. 6, pp. 697–706, 2019.

[82] N. A. Stutzke, M. C. Leifer, B. J. Tame, D. A. Paschen, and K. Kerby, "Low-profile lens method and apparatus for mechanical steering of aperture antennas," Nov. 29 2011, uS Patent 8,068,053. [Online]. Available: https://www.google.com/patents/US8068053

[83] K. Y. Kapusuz, Y. Şen, M. Bulut, . Karadede, and U. Oğuz, "Low-profile scalable phased array antenna at ku-band for mobile satellite communications," in *2016 IEEE International Symposium on Phased Array Systems and Technology (PAST)*, Oct 2016, pp. 1–4.

[84] B. Forman, "Directivity characteristics of scannable planar arrays," *IEEE Trans. Antennas Propagat.*, vol. 20, no. 3, pp. 245–252, May 1972.

[85] R. J. Mailloux, "Phased array theory and technology," *Proceedings of the IEEE*, vol. 70, no. 3, pp. 246–291, March 1982.

[86] M. U. Afzal and K. P. Esselle, "Steering the beam of medium-to-high gain antennas using near-field phase transformation," *IEEE Trans. Antennas Propagat.*, vol. 65, no. 4, pp. 1680–1690, April 2017.

[87] D. T. Moore, "Gradient-index optics: a review," *Appl. Opt.*, vol. 19, no. 7, pp. 1035–1038, Apr 1980. [Online]. Available: http://ao.osa.org/abstract.cfm?URI=ao-19-7-1035

[88] Y. He and G. V. Eleftheriades, "Matched, low-loss, and wideband graded-index flat lenses for millimeter-wave applications," *IEEE Transactions on Antennas and Propagation*, vol. 66, no. 3, pp. 1114–1123, March 2018.

[89] Y. Zhang, R. Mittra, and W. Hong, "A zoned two-layer flat lens design," in *Antenna Technology (iWAT), 2011 International Workshop on*, 2011, pp. 412–415.

[90] Y. Zhang, W. Hong, and Y. Zhang, "A beam steerable plane dielectric lens antenna," in *Antennas Propagation (ISAP), 2013 Proceedings of the International Symposium on*, vol. 01, Oct 2013, pp. 476–479.

[91] Y. Zhang, R. Mittra, and W. Hong, "Systematic design of planar lenses using artificial dielectrics," in *IEEE AP-S Int. Symp.*, 2010, pp. 1–4.

[92] Y. Ji and M. Fujita, "Design and analysis of a folded Fresnel zone plate antenna," *International Journal of Infrared and Millimeter Waves*, vol. 15, no. 8, pp. 1385–1406, 1994. [Online]. Available: http://dx.doi.org/10.1007/BF02096066

[93] H. Hristov and M. Herben, "Millimeter-wave Fresnel-zone plate lens and antenna," *IEEE Trans. Microw. Theory Techn.*, vol. 43, no. 12, pp. 2779–2785, Dec 1995.

[94] J. M. Rodríguez, H. D. Hristov, and W. Grote, "Fresnel zone plate and ordinary lens antennas: Comparative study at microwave and terahertz frequencies," in *2011 41st European Microwave Conference*, Oct 2011, pp. 894–897.

[95] H. D. Hristov, J. M. Rodríguez, and W. Grote, "The grooved-dielectric fresnel zone plate: An effective terahertz lens and antenna," *Microw. Opt. Technol. Lett.*, vol. 54, pp. 1343–1348, 2012.

[96] M. U. Afzal and K. P. Esselle, "A planar low-profile transverse permittivity gradient phase correcting structure for electromagnetic bandgap resonator antennas," in *2016 IEEE International Symposium on Antennas and Propagation (APSURSI)*, June 2016, pp. 1919–1920.

[97] Y. Yaguang, "Analytic solution of free space optical beam steering using Risley prisms," *Lightwave Technology, Journal of*, vol. 26, no. 21, pp. 3576–3583, 2008.

[98] Q. Peng, X. Wang, H. Ren, G. Chen, and J. Cao, L. Wang, "Analytical direct solutions of the Risley prism systems for tracking and pointing," *Applied Optics*, vol. 53, no. 13, pp. C83–C90, 2014.

[99] Y. Lu, Y. Zhou, M. Hei, and D. Fan, "Theoretical and experimental determination of steering mechanism for Risley prism systems," *Appl. Opt.*, vol. 52, no. 7, pp. 1389–1398, Mar 2013. [Online]. Available: http://ao.osa.org/abstract.cfm?URI=ao-52-7-1389

[100] C. D. McEwen and M. R. Khan, "Beam steering method with improved sidelobe response using dielectric wedges for satellite tv reception," pp. 681–685, 1984.

[101] N. Gagnon and A. Petosa, "Using rotatable planar phase shifting surfaces to steer a high-gain beam," *IEEE Trans. Antennas Propagat.*, vol. 61, no. 6, pp. 3086–3092, 2013.

[102] W. Milroy, S. Coppedge, and A. Lemons, "Variable inclination continuous transverse stub array," Jul. 19 2005, uS Patent 6,919,854. [Online]. Available: https://www.google.com.au/patents/US6919854

[103] W. H. Henderson and W. W. Milroy, "Wireless communication applications of the continuous transverse stub (CTS) array at microwave and millimeter wave frequencies," in *IEEE/ACES International Conference on Wireless Communications and Applied Computational Electromagnetics, 2005.*, April 2005, pp. 253–256.

[104] ThinKom, "Falcon-ka2517," Available:http://www.thinkom.com/antenna-products/thinair/falcon-ka2517/.

[105] M. U. Afzal, K. P. Esselle, and B. A. Zeb, "Dielectric phase-correcting structures for electromagnetic band gap resonator antennas," *IEEE Trans. Antennas propagat.*, vol. 63, no. 8, pp. 3390–3399, 2015.

[106] A. Lalbakhsh, M. U. Afzal, and K. P. Esselle, "Multiobjective particle swarm optimization to design a time-delay equalizer metasurface for an electromagnetic band-gap resonator antenna," *IEEE Antennas Wireless Propag. Lett.*, vol. 16, pp. 912–915, 2017.

[107] M. U. Afzal and K. P. Esselle, "A low-profile printed planar phase correcting surface to improve directive radiation characteristics of electromagnetic band gap resonator antennas," *IEEE Trans. Antennas Propag.*, vol. 64, no. 1, pp. 276–280, Jan 2016.

[108] ——, "Quasi-analytical synthesis of continuous phase correcting structures to increase the directivity of circularly polarized fabry-perot resonator antennas," *Journal of Applied Physics*, vol. 117, no. 21, pp. 214 092–214 099, 2015. [Online]. Available: http://scitation.aip.org/content/aip/journal/jap/117/21/10.1063/1.4921971

[109] S. J. Orfanidis, "Reflection and transmission," in *Electromagnetic Waves and Antennas*. Rutgers University, 2008.

[110] G. V. Trentini, "Partially reflecting sheet arrays," *IEEE Trans. Antennas Propagat.*, vol. 4, no. 4, pp. 666–671, 1956.

[111] N. Guerin, S. Enoch, G. Tayeb, P. Sabouroux, P. Vincent, and H. Legay, "A metallic Fabry-Perot directive antenna," *IEEE Trans. Antennas Propagat.*, vol. 54, no. 1, pp. 220–224, 2006.

[112] A. P. Feresidis and J. C. Vardaxoglou, "High gain planar antenna using optimised partially reflective surfaces," *IEE Proc.-Microw. Antennas Propag.*, vol. 148, no. 6, pp. 345–350, 2001.

[113] Z.-G. Liu, Z.-C. Ge, and X.-Y. Chen, "Research progress on Fabry-Perot resonator antenna," *Journal of Zhejiang University SCIENCE A*, vol. 10, no. 4, pp. 583–588, 2009. [Online]. Available: http://dx.doi.org/10.1631/jzus.A0820546

[114] D. R. Jackson and N. G. Alexopoulos, "Gain enhancement methods for printed circuit antennas," *IEEE Trans. Antennas Propagat.*, vol. 33, no. 9, pp. 976–987, 1985.

[115] J. L. Yao, M. J. Guo, Y. B. Qi, H. X. Zhu, R. Y. Yi, and L. Gao, "Processing of al 2 o 3 /srtio 3 /pdms composites with low dielectric loss," *IOP Conference Series: Materials Science and Engineering*, vol. 359, no. 1, p. 012017, 2018. [Online]. Available: http://stacks.iop.org/1757-899X/359/i=1/a=012017

[116] Y. J. C. Vardaxoglou, "Additive manufacturing of meta-atoms for microwave structures," in *2017 International Conference on Electromagnetics in Advanced Applications (ICEAA)*, Sept 2017, pp. 1836–1838.

[117] A. Lalbakhsh, M. U. Afzal, K. P. Esselle, and S. L. Smith, "A high-gain wideband ebg resonator antenna for 60 GHz unlicenced frequency band," 12th European Conference on Antennas and Propagation (EuCAP 2018).

[118] A. Lalbakhsh and K. P. Esselle, "Design of an improved resonant cavity antenna," in *2017 International Conference on Electromagnetics in Advanced Applications (ICEAA)*. IEEE, 2017, pp. 1658–1660.

[119] A. Lalbakhsh, M. U. Afzal, K. P. Esselle, and S. L. Smith, "An array of electromagnetic bandgap resonator antennas for v-band backhaul applications," in *The IIER International Conference, Tokyo, Japan, 7th-8th August, 2019, 69-71*, 2019.

[120] M. U. Afzal, A. Lalbakhsh, and K. P. Esselle, "A low-profile beam-tilted antenna array for receiving direct-broadcast satellite services," in *2018 IEEE Asia-Pacific Conference on Antennas and Propagation (APCAP)*. IEEE, 2018, pp. 147–148.

[121] M. U. Afzal, A. Lalbakhsh, N. Y. Koli, and K. P. Esselle, "Antenna beam steering by near-field phase transformation: Comparison between phase transforming printed metasurfaces and graded-dielectric plates," in *2019 International Conference on Electromagnetics in Advanced Applications (ICEAA)*. IEEE, 2019, pp. 0593–0595.

[122] M. Thevenot, C. Cheype, A. Reineix, and B. Jecko, "Directive photonic-bandgap antennas," vol. 47, no. 11, pp. 2115–2122, 1999.

[123] B. A. Zeb, R. M. Hashmi, and K. P. Esselle, "Wideband gain enhancement of slot antenna using one unprinted dielectric superstrate," *Electronics Letters*, vol. 51, no. 15, pp. 1146–1148, 2015.

[124] L. Leger, R. Granger, M. Thevenot, T. Monediere, and B. Jecko, "Multifrequency dielectric ebg antenna," *Microwave and Optical Technology Letters*, vol. 40, no. 5, pp. 420–423, 2004.

[125] A. Hosseini, F. De Flaviis, and F. Capolino, "A 60 GHz simple-to-fabricate single-layer planar Fabry–Pérot cavity antenna," *IET Microwaves, Antennas & Propagation*, vol. 9, no. 4, pp. 313–318, 2014.

[126] M. Akbari, S. Gupta, M. Farahani, A. Sebak, and T. Denidni, "Gain enhancement of circularly polarized dielectric resonator antenna based on FSS superstrate for MMW applications," *IEEE Trans. Antennas Propag.*, vol. 64, no. 12, pp. 5542–5546, 2016.

[127] M. Akbari, H. A. Ghalyon, M. Farahani, A. R. Sebak, and T. A. Denidni, "Spatially decoupling of CP antennas based on FSS for 30-GHz MIMO systems," *IEEE Access*, vol. 5, pp. 6527–6537, 2017.

[128] A. Weily and et al., "A planar resonator antenna based on a woodpile ebg material," *IEEE Trans. Antennas Propag.*, vol. 53, no. 1, pp. 216–223, 2005.

[129] A. Dadgarpour, B. Zarghooni, B. S. Virdee and T. A. Denidni, "One-and two-dimensional beam-switching antenna for millimeter-wave MIMO applications," *IEEE Trans. Antennas Propag.*, vol. 64, no. 2, pp. 564–573, 2016.

[130] A. Dadgarpour, B. Zarghooni, B. S. Virdee, and T. A. Denidni, "Enhancement of tilted beam in elevation plane for planar end-fire antennas using artificial dielectric medium," *IEEE Trans. Antennas Propag.*, vol. 63, no. 10, pp. 4540–4545, 2015.

[131] A. P. Feresidis and J. C. Vardaxoglou, "High gain planar antenna using optimised partially reflective surfaces," *IEE Proc.-Microw. Antennas Propag.*, vol. 148, no. 6, pp. 345–350, 2001.

[132] Z. B. A. Hashmi, R. M. and K. P. Esselle, "Wideband high-gain ebg resonator antennas with small footprints and all-dielectric superstructures," *IEEE Trans. Antennas Propag.*, vol. 62, no. 6, pp. 2970–2977, 2014.

[133] A. Baba, R. Hashmi, and K. Esselle, "Wideband gain enhancement of slot antenna using superstructure with optimised axial permittivity variation," *Electronics Letters*, vol. 52, no. 4, pp. 266–268, 2016.

[134] K. Konstantinidis, A. P. Feresidis, and P. S. Hall, "Multilayer partially reflective surfaces for broadband fabry-perot cavity antennas," *IEEE Transactions on Antennas and Propagation*, vol. 62, no. 7, pp. 3474–3481, 2014.

[135] D. H. Lee, Y. J. Lee, J. Yeo, R. Mittra, and W. S. Park, "Design of novel thin frequency selective surface superstrates for dual-band directivity enhancement," *IET Microwaves, Antennas & Propagation*, vol. 1, no. 1, pp. 248–254, 2007.

[136] B. Mohamadzade, A. Lalbakhsh, R. B. Simorangkir, A. Rezaee, and R. M. Hashmi, "Mutual coupling reduction in microstrip array antenna by employing cut side patches and ebg structures," *Progress In Electromagnetics Research*, vol. 89, pp. 179–187, 2020.

[137] B. Mohamadzade and M. Afsahi, "Mutual coupling reduction and gain enhancement in patch array antenna using a planar compact electromagnetic bandgap structure," *IET Microwaves, Antennas & Propagation*, vol. 11, no. 12, pp. 1719–1725, 2017.

[138] D. I. de Villiers and S. M. Koziel, "Fast multi-objective optimisation of pencil beam reflector antenna radiation pattern responses using kriging," *IET Microwaves, Antennas & Propagation*, vol. 12, no. 1, pp. 120–126, 2017.

[139] A. Lalbakhsh, M. U. Afzal, K. P. Esselle, and S. L. Smith, "Wideband near-field correction of a fabry-perot resonator antenna," *IEEE Transactions on Antennas and Propagation*, vol. 67, no. 3, pp. 1975–1980, 2019.

[140] T. Hayat, M. U. Afzal, A. Lalbakhsh, and K. P. Esselle, "Additively manufactured perforated superstrate to improve directive radiation characteristics of electromagnetic source," *IEEE Access*, vol. 7, pp. 153 445–153 452, 2019.

[141] P. Feng, X. Chen, and K. Huang, "High performance resonant cavity antenna with non-uniform metamaterial inspired superstrate," *International Journal of RF and Microwave Computer-Aided Engineering*, vol. 27, no. 7, p. e21114, 2017.

[142] L. Zhou, X. Chen, and X. Duan, "High gain fabry-perot cavity antenna with phase shifting surface," in *Wireless Information Technology and Systems (ICWITS) and Applied Computational Electromagnetics (ACES), 2016 IEEE/ACES International Conference on.* IEEE, 2016, pp. 1–2.

[143] B. Ratni, W. A. Merzouk, A. de Lustrac, S. Villers, G.-P. Piau, and S. N. Burokur, "Design of phase-modulated metasurfaces for beam steering in fabry–perot cavity antennas," *IEEE Antennas and Wireless Propagation Letters*, vol. 16, pp. 1401–1404, 2017.

[144] M. Afzal, A. Lalbakhsh, and K. Esselle, "Integration of sparse array feed and phase correction to design high gain resonant cavity antennas," in *2017 Progress in Electromagnetics Research Symposium-Fall (PIERS-FALL).* IEEE, 2017, pp. 2884–2887.

[145] T. Hayat, M. U. Afzal, F. Ahmed, A. Lalbakhsh, and K. P. Esselle, "Comparative analysis of highly transmitting phase correcting structures for electromagnetic bandgap resonator antenna," in *2020 International Workshop on Antenna Technology, Romania*, 2020.

[146] J. H. Kim, C.-H. Ahn, and J.-K. Bang, "Antenna gain enhancement using a holey superstrate," *IEEE Transactions on Antennas and Propagation*, vol. 64, no. 3, pp. 1164–1167, 2016.

[147] T. Hayat, M. U. Afzal, A. Lalbakhsh, and K. P. Esselle, "3-d-printed phase-rectifying transparent superstrate for resonant-cavity antenna," *IEEE Antennas and Wireless Propagation Letters*, vol. 18, no. 7, pp. 1400–1404, 2019.

[148] A. Lalbakhsh, "A wideband procedure for near-field enhancement of resonant cavity antennas," in *16th Australian Symposium on Antennas*, 2019.

[149] T. Hayat, M. U. Afzal, A. Lalbakhsh, F. Ahmed, and K. P. Esselle, "3d printable lightweight porous superstrate for improved radiation performance of antenna," in *4th Australian Microwave Symposium*, 2020.

[150] N. Gagnon, A. Petosa, and D. A. McNamara, "Printed hybrid lens antenna," *IEEE Transactions on Antennas and Propagation*, vol. 60, no. 5, pp. 2514–2518, 2012.

[151] N. Gagnon, A. Petosa, and D. McNamara, "Thin microwave quasi-transparent phase-shifting surface (pss)," *IEEE Transactions on Antennas and Propagation*, vol. 58, no. 4, pp. 1193–1201, 2010.

[152] J. Valentino and J. Goldenberg, *Introduction to computer numerical control (CNC)*. Prentice Hall Englewood Cliffs, 2003.

[153] S.-I. Kim and M.-H. Kim, "Evaluation of cutting characterization in plasma cutting of thick steel ship plates," *International Journal of Precision Engineering and Manufacturing*, vol. 14, no. 9, pp. 1571–1575, 2013.

[154] W. E. Frazier, "Metal additive manufacturing: a review," *Journal of Materials Engineering and Performance*, vol. 23, no. 6, pp. 1917–1928, 2014.

[155] S. Srinivas and N. R. Babu, "Penetration ability of abrasive waterjets in cutting of aluminum-silicon carbide particulate metal matrix composites," *Machining Science and Technology*, vol. 16, no. 3, pp. 337–354, 2012.

[156] S. Katayama, *Handbook of laser welding technologies*. Elsevier, 2013.

[157] A. Ghayekhloo, M. Akbari, M. Afsahi, A. A. Orouji, A. R. Sebak, and T. A. Denidni, "Multifunctional transparent electromagnetic surface based on solar cell for backscattering reduction," *IEEE Transactions on Antennas and Propagation*, vol. 67, no. 6, pp. 4302–4306, 2019.

[158] L. La Spada and L. Vegni, "Metamaterial-based wideband electromagnetic wave absorber," *Optics express*, vol. 24, no. 6, pp. 5763–5772, 2016.

[159] M. Akbari, F. Samadi, A.-R. Sebak, and T. A. Denidni, "Superbroadband coding metasurface for rcs reduction based on polarization conversion," *IEEE Antennas and Propagation Magazine*, 2019.

[160] S. Zarbakhsh, M. Akbari, F. Samadi, and A.-R. Sebak, "Broadband and high-gain circularly-polarized antenna with low rcs," *IEEE Transactions on Antennas and Propagation*, vol. 67, no. 1, pp. 16–23, 2018.

[161] P. Das, K. Mandal, and A. Lalbakhsh, "Single-layer polarization-insensitive frequency selective surface for beam reconfigurability of monopole antennas," *Journal of Electromagnetic Waves and Applications*, pp. 1–17, 2019.

[162] G. Karimi, M. Amirian, A. Lalbakhsh, and M. Ranjbar, "A new microstrip coupling system for realization of a differential dual-band bandpass filter," *AEU-International Journal of Electronics and Communications*, vol. 99, pp. 186–192, 2019.

[163] G. Karimi, A. Lalbakhsh, K. Dehghani, and H. Siahkamari, "Analysis of novel approach to design of ultra-wide stopband microstrip low-pass filter using modified u-shaped resonator," *ETRI Journal*, vol. 37, no. 5, pp. 945–950, 2015.

[164] M. Amirian, G. Karimi, A. Lalbakhsh, and M.-s. Bayati, "Compact differential bandpass filter with a narrow notched band using apcl structure suitable for uwb application," *Microelectronics Journal*, vol. 46, no. 9, pp. 869–874, 2015.

[165] G. Karimi, H. Siahkamari, F. K. Hamedani, and A. Lalbakhsh, "Design of modified z-shaped and t-shaped microstrip filter based on transfer function analysis," *Wireless Personal Communications*, vol. 82, no. 4, pp. 2005–2016, 2015.

[166] A. Ahmadi, S. Makki, A. Lalbakhsh, and S. Majidifar, "A novel dual-mode wideband band pass filter," *Applied Computational Electromagnetics Society Journal (ACES Journal)*, vol. 29, no. 9, pp. 735–742, 2014.

[167] G. Karimi, M. Yazdani, H. Siahkamari, and A. Lalbakhsh, "Design of microstrip lpf with sharp cut-off frequency and wide stopband," *Frequenz*, vol. 68, no. 7-8, pp. 313–319, 2014.

[168] A. A. Lotfi-Neyestanak and A. Lalbakhsh, "Improved microstrip hairpin-line bandpass filters for spurious response suppression," *Electron. Lett*, vol. 48, no. 14, pp. 858–859, 2012.

[169] K. Dehghani, G. Karimi, A. Lalbakhsh, and S. Maki, "Design of lowpass filter using novel stepped impedance resonator," *Electronics letters*, vol. 50, no. 1, pp. 37–39, 2014.

[170] M. Veysi, A. Ahmadi, G. Karimi, and A. Lalbakhsh, "Rfid tag design using spiral resonators and defected ground structure," *Radioengineering*, vol. 26, no. 4, pp. 1019–1024, 2017.

[171] H. Sariri, Z. Rahmani, A. Lalbakhsh, and S. Majidifar, "Compact lpf using t-shaped resonator," *Frequenz*, vol. 67, no. 1-2, pp. 17–20, 2013.

[172] A. Lalbakhsh, A. A. L. Neyestanak, and M. Naser-Moghaddasi, "Microstrip hairpin bandpass filter using modified minkowski fractal-shape for suppression of second harmonic," *IEICE transactions on electronics*, vol. 95, no. 3, pp. 378–381, 2012.

[173] G. Karimi, A. Lalbakhsh, and H. Siahkamari, "Design of sharp roll-off lowpass filter with ultra wide stopband," *IEEE Microw. Compon. Lett.*, vol. 23, no. 6, pp. 303–305, 2013.

[174] J. P. Jacobs and S. Koziel, "Reduced-cost microwave filter modeling using a two-stage g aussian process regression approach," *International Journal of RF and Microwave Computer-Aided Engineering*, vol. 25, no. 5, pp. 453–462, 2015.

[175] A. Lalbakhsh, G. Karimi, and F. Sabaghi, "Triple mode spiral wideband bandpass filter using symmetric dual-line coupling," *Electronics Letters*, vol. 53, no. 12, pp. 795–797, 2017.

[176] L. Zhang, G. Yang, Q. Wu, and J. Hua, "A novel active frequency selective surface with wideband tuning range for emc purpose," *IEEE Transactions on Magnetics*, vol. 48, no. 11, pp. 4534–4537, 2012.

[177] Q. Luo, S. Gao, M. Sobhy, and X. Yang, "Wideband transmitarray with reduced profile," *IEEE Antennas and Wireless Propagation Letters*, vol. 17, no. 3, pp. 450–453, 2018.

[178] S. Ghosh and K. V. Srivastava, "Broadband polarization-insensitive tunable frequency selective surface for wideband shielding," *IEEE Transactions on Electromagnetic Compatibility*, vol. 60, no. 1, pp. 166–172, 2018.

[179] A. Lalbakhsh, K. Esselle, and S. Smith, "Design of a single-slab low-profile frequency selective surface," in *2017 Progress in Electromagnetics Research Symposium-Fall (PIERS-FALL)*. IEEE, 2017, pp. 2360–2363.

[180] D. F. Mamedes, A. G. Neto, J. C. e Silva, and J. Bornemann, "Design of reconfigurable frequency-selective surfaces including the pin diode threshold region," *IET Microwaves, Antennas & Propagation*, 2018.

[181] W. Mohyuddin, D. S. Woo, H. C. Choi, and K. W. Kim, "A practical double-sided frequency selective surface for millimeter-wave applications," *Review of Scientific Instruments*, vol. 89, no. 2, p. 024703, 2018.

[182] W. Mohyuddin, D. Kim, H. Choi, and K. Kim, "Comparative study of square and circular loop frequency selective surfaces for millimeter-wave imaging diagnostics systems," *Sensors*, vol. 18, no. 9, p. 3079, 2018.

[183] S. Ghosh and S. Lim, "Fluidically reconfigurable multifunctional frequency-selective surface with miniaturization characteristic," *IEEE Transactions on Microwave Theory and Techniques*, vol. 66, no. 8, pp. 3857–3865, 2018.

[184] B. Li and Z. Shen, "Bandpass frequency selective structure with wideband spurious rejection," *IEEE Antennas and Wireless Propagation Letters*, vol. 13, pp. 145–148, 2014.

[185] R. Sivasamy and M. Kanagasabai, "Novel reconfigurable 3-d frequency selective surface," *IEEE Transactions on Components, Packaging and Manufacturing Technology*, vol. 7, no. 10, pp. 1678–1682, 2017.

[186] L. La Spada, S. Haq, and Y. Hao, "Modeling and design for electromagnetic surface wave devices," *Radio Science*, vol. 52, no. 9, pp. 1049–1057, 2017.

[187] M. I. Khan and F. A. Tahir, "Simultaneous quarter-wave plate and half-mirror operation through a highly flexible single layer anisotropic metasurface," *Scientific reports*, vol. 7, no. 1, p. 16059, 2017.

[188] L. La Spada, C. Spooner, S. Haq, and Y. Hao, "Curvilinear metasurfaces for surface wave manipulation," *Scientific reports*, vol. 9, no. 1, p. 3107, 2019.

[189] L. La Spada, "Metasurfaces for advanced sensing and diagnostics," *Sensors*, vol. 19, no. 2, p. 355, 2019.

[190] Y. Huang, J. Luo, M. Pu, Y. Guo, Z. Zhao, X. Ma, X. Li, and X. Luo, "Catenary electromagnetics for ultra-broadband lightweight absorbers and large-scale flat antennas," *Advanced Science*, vol. 6, no. 7, p. 1801691, 2019.

[191] M. Pu, Z. Zhao, Y. Wang, X. Li, X. Ma, C. Hu, C. Wang, C. Huang, and X. Luo, "Spatially and spectrally engineered spin-orbit interaction for achromatic virtual shaping," *Scientific reports*, vol. 5, p. 9822, 2015.

[192] Y. Guo, Y. Wang, M. Pu, Z. Zhao, X. Wu, X. Ma, C. Wang, L. Yan, and X. Luo, "Dispersion management of anisotropic metamirror for super-octave bandwidth polarization conversion," *Scientific Reports*, vol. 5, p. 8434, 2015.

[193] R. E. Hodges, N. Chahat, D. J. Hoppe, and J. D. Vacchione, "A deployable high-gain antenna bound for mars: Developing a new folded-panel reflectarray for the first cubesat mission to mars." *IEEE Antennas and Propagation Magazine*, vol. 59, no. 2, pp. 39–49, 2017.

[194] F. Yang, R. Deng, S. Xu, and M. Li, "Design and experiment of a near-zero-thickness high-gain transmit-reflect-array antenna using anisotropic metasurface," *IEEE Transactions on Antennas and Propagation*, vol. 66, no. 6, pp. 2853–2861, 2018.

[195] S. H. R. Tuloti, P. Rezaei, and F. T. Hamedani, "High-efficient wideband transmitarray antenna," *IEEE Antennas and Wireless Propagation Letters*, vol. 17, no. 5, pp. 817–820, 2018.

[196] A. Dadgarpour, A. A. Kishk, and T. A. Denidni, "Gain enhancement of planar antenna enabled by array of split-ring resonators," *IEEE Trans. Antennas Propag*, vol. 64, no. 8, pp. 3682–3687, 2016.

[197] W. L. Stutzman and G. A. Thiele, *Antenna theory and design*. John Wiley & Sons, 2013.

[198] R. J. Bauerle, R. Schrimpf, E. Gyorko, and J. Henderson, "The use of a dielectric lens to improve the efficiency of a dual-polarized quad-ridge horn from 5 to 15 ghz," *IEEE Transactions on Antennas and Propagation*, vol. 57, no. 6, pp. 1822–1825, 2009.

[199] C. Y. Tan and K. T. Selvan, "A performance comparison of a ku-band conical horn with an inserted cone-sphere with horns with an integrated dielectric lens and metamaterial loading [antenna designer's notebook]," *IEEE Antennas and Propagation Magazine*, vol. 53, no. 5, pp. 115–122, 2011.

[200] M. K. T. Al-Nuaimi and W. Hong, "Discrete dielectric reflectarray and lens for e-band with different feed," *IEEE Antennas and Wireless Propagation Letters*, vol. 13, pp. 947–950, 2014.

[201] C. Jouanlanne, A. Clemente, M. Huchard, J. Keignart, C. Barbier, T. Le Nadan, and L. Petit, "Wideband linearly polarized transmitarray antenna for 60 ghz backhauling," *IEEE Trans. Antennas Propag*, vol. 65, no. 3, pp. 1440–1445, 2017.

[202] X. Chen, Y. Ge, and T. S. Bird, "Reduction of sidelobe radiations of the standard pyramidal horn using a thin metamaterial lens," *Electronics Letters*, vol. 52, no. 24, pp. 1973–1974, 2016.

[203] Q.-W. Lin and H. Wong, "A low-profile and wideband lens antenna based on high-refractive-index metasurface," *IEEE Transactions on Antennas and Propagation*, vol. 66, no. 11, pp. 5764–5772, 2018.

[204] K. Liu, Y. Ge, and C. Lin, "A compact wideband high-gain metasurface-lens-corrected conical horn antenna," *IEEE Antennas and Wireless Propagation Letters*, vol. 18, no. 3, pp. 457–461, 2019.

[205] A. Lalbakhsh, M. U. Afzal, K. P. Esselle, and S. L. Smith, "Low-cost non-uniform metallic lattice for rectifying aperture near-field of electromagnetic bandgap resonator antennas," *IEEE Transactions on Antennas and Propagation*, vol. 68, 2020.

[206] K. T. Pham, A. Clemente, E. Fourn, F. Diaby, L. Dussopt, and R. Sauleau, "Low-cost metal-only transmitarray antennas at ka-band," *IEEE Antennas and Wireless Propagation Letters*, vol. 18, no. 6, pp. 1243–1247, 2019.

[207] C. A. Balanis, *Antenna theory: analysis and design*. John wiley & sons, 2016.

[208] M. Amin, O. Siddiqui, F. A. Tahir *et al.*, "Quasi-crystal metasurface for simultaneous half-and quarter-wave plate operation," *Scientific reports*, vol. 8, no. 1, p. 15743, 2018.

[209] K. K. Katare, S. Chandravanshi, A. Biswas, and M. J. Akhtar, "Realization of split beam antenna using transmission-type coding metasurface and planar lens," *IEEE Transactions on Antennas and Propagation*, vol. 67, no. 4, pp. 2074–2084, 2019.

[210] N. Gagnon and A. Petosa, "Using rotatable planar phase shifting surfaces to steer a high-gain beam," *IEEE Trans. Antennas Propag.*, vol. 61, no. 6, pp. 3086–3092, 2013.

[211] W. E. Frazier, "Metal additive manufacturing: a review," *Journal of Materials Engineering and Performance*, vol. 23, no. 6, pp. 1917–1928, 2014.

[212] V. A. Nemchinsky and W. Severance, "What we know and what we do not know about plasma arc cutting," *Journal of Physics D: Applied Physics*, vol. 39, no. 22, p. R423, 2006.

[213] R. Siebert, J. Schneider, and E. Beyer, "Laser cutting and mechanical cutting of electrical steels and its effect on the magnetic properties," *IEEE Transactions on Magnetics*, vol. 50, no. 4, pp. 1–4, 2014.

[214] B. Mohamadzade, R. B. Simorangkir, R. M. Hashmi, Y. Chao-Oger, M. Zhadobov, and R. Sauleau, "A conformal band-notched ultrawideband antenna with monopole-like radiation characteristics," *IEEE Antennas and Wireless Propagation Letters*, 2019.

[215] B. Mohamadzade, R. M. Hashmi, R. B. Simorangkir, R. Gharaei, S. Ur Rehman, and Q. H. Abbasi, "Recent advances in fabrication methods for flexible antennas in wearable devices: State of the art," *Sensors*, vol. 19, no. 10, p. 2312, 2019.

[216] B. Mohamadzade, R. B. Simorangkir, R. M. Hashmi, and S. Shrestha, "Low-profile pattern reconfigurable antenna for wireless body area networks," in *2019 International Conference on Electromagnetics in Advanced Applications (ICEAA)*. IEEE, 2019, pp. 546–547.